

---


Electronic Theses and Dissertations

---

2019

## Molecular Basis of Membrane Pore Formation by Amyloid Beta Peptide

Nabin Kandel  
*University of Central Florida*

 Part of the [Molecular and Cellular Neuroscience Commons](#)  
Find similar works at: <https://stars.library.ucf.edu/etd>  
University of Central Florida Libraries <http://library.ucf.edu>

This Doctoral Dissertation (Open Access) is brought to you for free and open access by STARS. It has been accepted for inclusion in Electronic Theses and Dissertations by an authorized administrator of STARS. For more information, please contact [STARS@ucf.edu](mailto:STARS@ucf.edu).

---

### STARS Citation

Kandel, Nabin, "Molecular Basis of Membrane Pore Formation by Amyloid Beta Peptide" (2019). *Electronic Theses and Dissertations*. 6851.  
<https://stars.library.ucf.edu/etd/6851>

MOLECULAR BASIS OF MEMBRANE PORE FORMATION BY AMYLOID BETA  
PEPTIDE

by

NABIN KANDEL  
MS University of Texas at Brownsville, 2014

A dissertation submitted in partial fulfilment of the requirements  
for the degree of Doctor of Philosophy  
in the Department of Physics  
in the College of Sciences  
at the University of Central Florida  
Orlando, Florida

Summer Term  
2019

Major Professor: Suren A Tatulian

© 2019 Nabin Kandel

## ABSTRACT

Alzheimer's Disease (AD) is a neurodegenerative disorder that affects around 50 million people worldwide and causes cognitive decline, brain atrophy and death. Despite extensive basic and clinical studies and drug development efforts, currently no effective treatments are available for AD. The amyloid  $\beta$  ( $A\beta$ ) peptide is neurotoxic and is tightly associated with AD pathology, but the molecular mechanism of its action remains unclear. There are various forms of  $A\beta$  in the brain, ranging from the full length  $A\beta_{1-42}$  to shorter peptides, such as a strongly toxic  $A\beta_{25-35}$  fragment. The Amyloid Cascade Hypothesis (ACH) postulated that extracellular  $A\beta$  deposits cause the disease. More recently, the soluble  $A\beta$  oligomers came into the focus of research as they proved to be the major neurotoxic entities. One of the mechanisms by which  $A\beta$  peptides, including  $A\beta_{25-35}$ , kill neurons is membrane perforation and disruption of cellular homeostasis. Although direct membrane interaction and pore formation by  $A\beta$  has been documented, the detailed structural aspects of membrane pores remain elusive. Here, we quantitatively describe the structure of  $A\beta_{25-35}$  in aqueous buffer and in lipid environment, its binding to membranes, pore formation, and the details of membrane pores. We have shown that membrane binding of  $A\beta_{25-35}$  is electrostatically driven.  $A\beta_{25-35}$  forms  $\beta$ -barrel like structures ranging from hexamers to octamers and then assemble into supra-molecular structures forming calcium-conducting pores in the membrane with radius of 6 Å to 7 Å. The structural features of  $A\beta_{25-35}$  pores depend on the content of cholesterol in the membranes. Moreover, the aggregation and structural changes of a series of  $A\beta$  fragments have been analyzed to identify the segment(s) of highest propensity for fibrillogenesis that might serve as initiators of  $A\beta$  aggregation and conversion into toxic species. Finally, the structures of the full-length  $A\beta_{1-42}$  and a hypertoxic version pEA $\beta_{3-42}$ , in lipid environment have been analyzed by solid state nuclear magnetic resonance. Collectively, these studies will elucidate the structural details of membrane pores formed by  $A\beta$  peptides as targets for new anti-AD therapies.

Dedicated to my family for their uncredited support....

## **ACKNOWLEDGMENTS**

First of all, I would like to express my sincere thanks to my advisor, Dr. Suren A Tatulian, for accepting me as a research student, supporting me as a research assistant, and uniquely guiding me all the way to this point. It would not have been possible without his expertise and mentor. I am also indebted to Dr. Bo Chen for his constant support with solid state nuclear magnetic resonance (ssNMR) techniques especially when I had no prior knowledge of it. I would also like to acknowledge Dr. Alfons Schulte and Dr. Kenneth Teter for accepting my request to serve as an internal and external members of my dissertation committee. I am also very obliged to the Department of Physics, UCF for providing me graduate teaching assistantship during my studies. I would also like to remember all the professors who taught me different course during my stay here in UCF. I am also grateful to Dr. Greg Goldblatt for helping me with FTIR experiments and training me with other instruments in the lab. I am also thankful to Greta Apostoli for her help with some vesicles leakage experiments. Finally, I am thankful to my family, especially to my wife and all my well wishers for their moral support.

## TABLE OF CONTENTS

LIST OF FIGURES . . . . .	ix
LIST OF TABLES . . . . .	.xviii
CHAPTER 1: INTRODUCTION . . . . .	1
CHAPTER 2: LITERATURE REVIEW . . . . .	4
2.1 Alzheimer’s Disease: Progress and Challenges . . . . .	4
2.2 Membrane Interactions of Different A $\beta$ Variants . . . . .	6
2.3 Membrane Pores and Associated Neurotoxicity . . . . .	9
2.3.1 Calcium Dysregulation . . . . .	9
2.3.2 Cholesterol Metabolism . . . . .	10
CHAPTER 3: MATERIALS AND METHODS . . . . .	12
3.1 Materials . . . . .	12
3.2 Methods . . . . .	12
3.2.1 Fluorescence Spectroscopy . . . . .	12
3.2.2 Circular Dichroism . . . . .	17

3.2.3	Fourier Transform Infrared Spectroscopy . . . . .	20
3.2.4	Attenuated Total Reflection Fourier Transform Infrared Spectroscopy . . . . .	22
3.2.5	Introduction to Forster Resonance Energy Transfer . . . . .	23
3.2.6	Principles of Solid State Nuclear Magnetic Resonance . . . . .	27
3.3	Theoretical Prospective of Membrane Binding and Pore Formation . . . . .	35
3.4	FTIR Data Analysis . . . . .	36
3.4.1	Secondary Structures Determination . . . . .	36
3.4.2	Orientation of Peptides . . . . .	38
CHAPTER 4: RESULTS . . . . .		39
4.1	Salt Dependent Membrane Binding and Pore Formation by $A\beta_{25-35}$ . . . . .	39
4.1.1	$A\beta_{25-35}$ Peptide in Aqueous Buffer . . . . .	39
4.1.2	Binding of $A\beta_{25-35}$ Peptide to Lipid Membrane . . . . .	40
4.1.3	Membrane Permeabilization Effect of Peptide . . . . .	43
4.1.4	Structure of Peptide in Lipid Vesicles . . . . .	48
4.2	Role of Cholesterol on Membrane Binding and Pore Formation by $A\beta_{25-35}$ . . . . .	50
4.2.1	Structure of Peptide by Circular Dichroism . . . . .	53
4.2.2	Effect of Cholesterol on Membrane Fluidity . . . . .	55



4.2.3	Determination of Peptide Structure Using ATR–FTIR Spectroscopy . . . . .	57
4.2.4	Peptide Orientation and Lipid Order from ATR–FTIR Spectroscopy . . . . .	58
4.2.5	Structure of the Pore . . . . .	60
4.3	Detection of Early Stage Aggregation of $A\beta_{1-42}$ Using FRET . . . . .	65
4.3.1	FRET For Soluble Oligomer Detection . . . . .	66
4.3.2	Secondary Structure Change During Oligomerization Using CD . . . . .	71
4.4	FTIR and ssNMR Analysis of Neurotoxic Peptides $A\beta_{1-42}$ and $pEA\beta_{3-42}$ in Mem- brane . . . . .	72
4.4.1	FTIR Shows Different Aggregation Pathways of $A\beta_{1-42}$ and $pEA\beta_{3-42}$ . . . . .	72
4.4.2	Solid State NMR Data Shows Coexisting Ordered ( $\beta$ -Sheet) and Disor- dered (Turns and Loops) Regions in Both Peptides $A\beta_{1-42}$ and $pEA\beta_{3-42}$ in Lipid Membrane. . . . .	75
CHAPTER 5: CONCLUSION . . . . .		84
APPENDIX A: LIST OF ABBREVIATIONS . . . . .		86
APPENDIX B: SUPPLEMENTARY DATA OF MEMBRANE PORE FORMATION . . . . .		89
APPENDIX C: SUPPLEMENTARY DATA OF FTIR AND ssNMR . . . . .		96
LIST OF REFERENCES . . . . .		104

## LIST OF FIGURES

Figure 2.1: Calcium dysregulation in Alzheimer’s disease [85]. . . . .	9
Figure 3.1: Schematic diagram of fluorescence and phosphorescence phenomena. . . .	13
Figure 3.2: Chemical formula of Quin–2 tetrapotassium salt. . . . .	14
Figure 3.3: Membrane lipid components used in the study: POPC (neutral or zwitterionic lipid), POPG (negative lipid) and cholesterol (non–ionic sterol). . . . .	15
Figure 3.4: Preparation of Quin–2 loaded unilamellar vesicles through extrusion. . . .	16
Figure 3.5: Chemical structure of Laurdan. . . . .	16
Figure 3.6: Schematic diagram showing how to remove Quin–2 present outside the vesicles by using desalting column. . . . .	17
Figure 3.7: Schematic diagram of CD spectroscopy. . . . .	18
Figure 3.8: CD spectra of $\beta$ –sheet (blue), $\alpha$ –helix (black) and random coil or un-ordered (red). . . . .	19
Figure 3.9: Schematic configuration of FTIR spectroscopy [102]. . . . .	20
Figure 3.10: Schematic diagram of ATR–FTIR spectroscopy [102]. . . . .	22
Figure 3.11: Figure showing overlapping of emission spectra of donors and acceptor for FRET. Abbreviations: DE (Donor Emission), AA (Acceptor Absorption), AE (Acceptor Emission). . . . .	24

Figure 3.12: Splitting of spectral lines in presence of external magnetic field. . . . .	28
Figure 3.13: Free induction decay and corresponding signal in frequency domain. . . . .	28
Figure 3.14: Schematic diagram of DARR mixing. This resonance can connect either intra-residues or inter-residues depending on mixing time. . . . .	33
Figure 4.1: FTIR ( <i>a</i> ) and CD ( <i>b</i> ) structures of $A\beta_{25-35}$ in aqueous buffer. FTIR mea- surements were done in buffer of 50 mM Na,K-phosphate, 50 mM NaCl, pD 7.2 and CD measurements were carried out in Tris buffer (145 mM NaCl, 50 mM Tris, pH 7.2). . . . .	39
Figure 4.2: $\zeta$ -potential of lipid vesicles as a function of added peptide at different salt (NaCl) concentrations: 10 mM ( <i>a</i> ), 30 mM ( <i>b</i> ), and 75 mM ( <i>c</i> ) in Tris-HCl buffer (20 mM, pH 7.2). Solid, dashed and dotted lines represent theoretical plots for aggregation numbers of $z = 1$ , $z = 4$ , and $z = 8$ respectively. The corresponding variation of binding constants (apparent) are shown in panels ( <i>d - f</i> ). The working lipid concentration is 0.2 mM with membrane molar composition of 60 % PC, 30 % PG and 10 % cholesterol. . . . .	41
Figure 4.3: Quin-2 fluorescence as a function of time due to influx of $Ca^{2+}$ at different salt concentrations: 30 mM ( <i>a</i> ), 75 mM ( <i>b</i> ), 150 mM ( <i>c</i> ) and 180 mM ( <i>d</i> ). Squares, circles and triangles represent $P : L = 1 : 10$ , $1 : 5$ and $1 : 3$ and rhombs represent effect of ionophore as positive control. The working lipid concentration is 0.2 mM with membrane molar composition of 60 % PC, 30 % PG and 10 % cholesterol. All data are normalized to unity based on the maximum effect of ionophore. . . . .	44

Figure 4.4: Relative Quin-2 fluorescence intensity as a function of salt in buffer (a), single exponential rate constant as a function of salt in buffer (b), and second order rate constant of pore formation as a function of salt in buffer (c). Solid ( $z = 1$ ), dashed ( $z = 4$ ) and dotted ( $z = 8$ ) lines represent theoretical isotherms respectively. The working lipid concentration is 0.2 mM with membrane molar composition of 60 % PC, 30 % PG and 10 % cholesterol. Peptide concentration is 66.7 $\mu$ M. . . . .	45
Figure 4.5: Model of lipid vesicles with Quin-2 entrapped inside and illustration of membrane permeation, pore formation, calcium influx and Quin-2 fluorescence enhancement. . . . .	45
Figure 4.6: Size distribution of lipid vesicles as a function of peptide concentration shown using dynamic light scattering. The working lipid vesicle concentration is 0.2 mM with membrane molar composition of 60 % PC, 30 % PG and 10 % cholesterol. . . . .	46
Figure 4.7: $\zeta$ -potential of lipid vesicles as a function of added peptide concentrations with NaCl salt of 75 mM in the buffer. Solid, dashed and dotted lines represent theoretical plots for aggregation numbers of $z = 1$ , $z = 4$ , and $z = 8$ respectively (a). Quin-2 fluorescence as a function of time (b). Squares, circles and triangles represent $P : L = 1 : 10$ , $1 : 5$ and $1 : 3$ and rhombs represent effect of ionophore as positive control. The working lipid concentration is 0.2 mM with membrane molar composition of 90 % PC and 10 % cholesterol that will behave as a neutral membrane. . . . .	48

Figure 4.8: CD spectra of  $A\beta_{25-35}$  with (black solid) and without (gray solid) lipid vesicles at different ionic strength: (a) 30 mM, (b) 50 mM, (c) 75 mM, (d) 180 mM, (e) 225 mM, and (f) 300 mM of NaCl. The second derivatives are shown with respective dotted lines with (black) and without (gray) lipid vesicles. The working lipid concentration is 0.2 mM with membrane molar composition of 60 % PC, 30 % PG and 10 % cholesterol. . . . . 49

Figure 4.9: Quin-2 fluorescence as a function of time (due to influx of  $Ca^{2+}$ ) at different cholesterol concentrations: 0 % (a), 5 % (b), 10 % (c), 20 % (d), and 40 % (e). The lipid composition is  $(0.7 - x_{chol})$ , 0.3, and  $x_{chol}$  mol % of POPC, POPG and cholesterol with  $x_{chol}$  varying from 0.00, 0.05, 0.10, 0.20, and 0.40 respectively. Squares, circles and triangles represent  $P : L = 1 : 10$ ,  $1 : 5$  and  $1 : 3$  and rhombs represent effect of ionophore as positive control. The working lipid concentration is 0.2 mM with buffer ionic strength of 75 mM. Graph (f) represents increase in Quin-2 fluorescence 2 min after the addition of peptide. . . . . 50

Figure 4.10: Relative Quin-2 fluorescence (a), single exponential rate constant (b), second-order rate constant of pore formation (c), affinity constant of peptide oligomers within the membrane (d), and the number of oligomers in the pore structure (e) as a function of cholesterol. The lipid composition is  $(0.7 - x_{chol})$ , 0.3, and  $x_{chol}$  mol % of POPC, POPG and cholesterol with  $x_{chol}$  varying from 0.00, 0.05, 0.10, 0.20, and 0.40 respectively. The working lipid concentration is 0.2 mM and ionic strength of buffer is 75 mM NaCl. . . . . 51

Figure 4.11: Light scattering of lipid vesicles before (gray) and after (black) addition of ionophore or peptide in  $\mu\text{M}$  as shown in the legend at various cholesterol concentrations: 0% (a), 5% (b), 10% (c), 20% (d), and 40% (e). The lipid composition is  $(0.7 - x_{chol})$ , 0.3, and  $x_{chol}$  mol% of POPC, POPG and cholesterol with  $x_{chol}$  varying from 0.00, 0.05, 0.10, 0.20, and 0.40 respectively. The working lipid concentration is 0.2 mM and ionic strength of buffer is 75 mM NaCl. . . . . 52

Figure 4.12: CD spectra of  $A\beta_{25-35}$  peptide at different cholesterol concentrations: 0% (a), 5% (b), 10% (c), 20% (d), and 40% (e) in lipid vesicles with ionic strength of buffer 75 mM NaCl. The lipid composition is  $(0.7 - x_{chol})$ , 0.3, and  $x_{chol}$  mol% of POPC, POPG and cholesterol with  $x_{chol}$  varying from 0.00, 0.05, 0.10, 0.20, and 0.40 respectively. The working lipid concentration is 0.2 mM. Legend:  $P : L = 1 : 10$  (gray),  $1 : 5$  (black dotted), and  $1 : 3$  (black solid). . . . . 54

Figure 4.13: Original CD spectrum of  $A\beta_{25-35}$  peptide (a) with no lipid vesicles and (b) membrane-bound peptide at various cholesterol percentages as shown in the graph. The ionic strength of buffer is 75 mM NaCl and the working lipid concentration is 0.2 mM. . . . . 55

Figure 4.14: Membrane fluidity as measured by Laurdan fluorescence (a) and generalized polarization (GP) of Laurdan (b) at different cholesterol concentrations shown. The lipid composition is  $(0.7 - x_{chol})$ , 0.3, and  $x_{chol}$  mol% of POPC, POPG and cholesterol with  $x_{chol}$  varying from 0.00, 0.05, 0.10, 0.20, and 0.40 respectively. . . . . 56

Figure 4.15: Figure shows fractions of secondary structures of  $A\beta_{25-35}$  in lipid multilayers in dry state (a),  $D_2O$  vapor (b) and  $D_2O$  buffer (c). The lipid composition is  $(0.7 - x_{chol})$ , 0.3, and  $x_{chol}$  mol % of POPC, POPG and cholesterol with  $x_{chol}$  varying from 0.00, 0.05, 0.10, 0.20, and 0.40 respectively. The symbols used are  $\alpha$  for  $\alpha$ -helix,  $\beta$  for  $\beta$ -sheet,  $t$  for turn and  $\rho$  for irregular structures. . . . . 58

Figure 4.16: Sketch of a  $\beta$ -stranded barrel. The strands are oriented at an angle  $\beta$  with respect to the central axis of barrel and barrel axis is at angle  $\gamma$  with membrane normal. . . . . 61

Figure 4.17: (a) Cartoon structure of  $A\beta_{25-35}$  with hydrogen bonding between  $S^{26}$  and  $K^{28}$  as shown by the dotted line. Color code is as follow: carbon in gray, nitrogen in blue, oxygen in red, and sulfur in yellow. Hydrogen atoms are not shown for clarity. (b) Model of 6-stranded  $\beta$ -barrel of the peptide in unwrapped form (inside barrel view). (c) Cartoon for a 6-stranded  $\beta$ -barrel (d) Cartoon for a 8-stranded  $\beta$ -barrel of  $A\beta_{25-35}$  (ribbon format), using residues (90 - 100) of  $\alpha B$  crystallin (reference: PDB code 3sgn). This forms "cylindrin" structure consisting of 6-stranded  $\beta$ -barrel [143]. (e) Proposed pore stabilizing H-bonding between  $S^{26}$  and  $K^{28}$  of one strand with  $K^{28}$  and  $S^{26}$  of adjacent strand in  $\beta$ -barrel. . . . . 62

Figure 4.18: Side view (a) and top view (along the pore axis) (b) of  $\alpha B$  crystallin residues (90 - 100) (reference: PDB code 3sgn). . . . . 63

Figure 4.19: Top view (along the pore axis) of the final membrane pore (radius of central cavity about 6.5 Å) formed by $A\beta_{25-35}$ as hexamer of 6-stranded barrel constructed from $\alpha B$ crystallin (90 – 100) (reference: PDB code 3sgn), replacing the side chains by $A\beta_{25-35}$ side chains. Each barrel is turned about its cylindrical axes by 60° relative to its neighbors. . . . .	64
Figure 4.20: Different segments of peptide $A\beta_{1-42}$ fragments that have been studied. Phenylalanine (F) and tyrosine (T) residues are highlighted yellow and red, respectively. . . . .	67
Figure 4.21: Several possible arrangements of different segments of peptide $A\beta_{1-42}$ . . . . .	68
Figure 4.22: Structures of peptides $A\beta_{1-10}$ , $A\beta_{11-20}$ and their equimolar mixture in HFIP and dry states (left panels). Right panels show similar structures of peptides $A\beta_{6-15}$ , $A\beta_{16-25}$ and their equimolar mixture in HFIP and dry states respectively using CD. . . . .	69
Figure 4.23: FRET difference spectra and time dependence of difference F and Y fluorescence intensities for $A\beta_{1-10}/A\beta_{11-20}$ (A,B) and $A\beta_{6-15}/A\beta_{16-25}$ (C,D). In panels A and C, the insets show the hours of incubation in buffer (25 mM NaCl, 20 μM ThT, 25 mM Na,K-phosphate, pH 7.2) at 25 °C. . . . .	70
Figure 4.24: CD spectra of $A\beta_{1-10}$ (A), $A\beta_{11-20}$ (B), equimolar mixture of $A\beta_{1-10}$ and $A\beta_{11-20}$ (C), $A\beta_{6-15}$ (D), $A\beta_{16-25}$ (E), and the equimolar mixture of $A\beta_{6-15}$ and $A\beta_{16-25}$ (F) at various time periods of incubation in aqueous buffer containing 25 mM NaCl, 20 μM ThT, 25 mM Na,K-phosphate, pH 7.2 at temperature 25 °C. . . . .	71



Figure 4.25: FTIR spectra of $A\beta_{1-42}$ in lipid membrane and corresponding time dependence of the values of $I_{\beta}/I_{\alpha}$ in 10 mM Na,K-phosphate with pD 7.2, in peptide to lipid ratio of $P : L = 1 : 50$ . Lipid composition is 60 % POPC, 30 % POPG and 10 % cholesterol. . . . .	73
Figure 4.26: FTIR spectra of $pEA\beta_{3-42}$ in lipid membrane and corresponding time dependence of the values of $I_{\beta}/I_{\alpha}$ in 10 mM Na,K-phosphate with pD 7.2, in peptide to lipid ratio of $P : L = 1 : 50$ . Lipid composition is 60 % POPC, 30 % POPG and 10 % cholesterol. . . . .	74
Figure 4.27: 1D CP $^{13}\text{C}$ -NMR spectra of (a) pure lipid sample with 60 % POPC, 30 % POPG and 10 % cholesterol (b) pure peptide $A\beta_{1-42}$ with $^{13}\text{C}$ , $^{15}\text{N}$ -segmentally labeled at $^{16}\text{K}^{17}\text{L}^{18}\text{V}$ . . . . .	75
Figure 4.28: 1D CP $^{13}\text{C}$ -NMR spectra of peptide (c) $A\beta_{1-42}$ and (d) $pEA\beta_{3-42}$ reconstituted in lipid membrane. Peptides are $^{13}\text{C}$ , $^{15}\text{N}$ -segmentally labeled at $^{16}\text{K}^{17}\text{L}^{18}\text{V}$ . . . . .	76
Figure 4.29: 1D $^{13}\text{C}$ -NMR spectra of the peptide $A\beta_{1-42}$ with $^{13}\text{C}$ , $^{15}\text{N}$ -segmentally labeled at $^{36}\text{V}^{37}\text{G}^{38}\text{G}^{39}\text{V}$ (e) CP and (f) direct $\pi/2$ pulse ( <i>Onepul</i> ) in lipid membrane. . . . .	77
Figure 4.30: 1D $^{13}\text{C}$ -NMR spectra of the peptide $pEA\beta_{3-42}$ with $^{13}\text{C}$ , $^{15}\text{N}$ -segmentally labeled at $^{36}\text{V}^{37}\text{G}^{38}\text{G}^{39}\text{V}$ (g) CP and (h) direct $\pi/2$ pulse ( <i>Onepul</i> ) in lipid membrane. . . . .	78
Figure 4.31: 2D $^{13}\text{C}$ - $^{13}\text{C}$ DARR spectrum of the peptide $pEA\beta_{3-42}$ $^{13}\text{C}$ , $^{15}\text{N}$ -segmentally labeled at $^{36}\text{V}^{37}\text{G}^{38}\text{G}^{39}\text{V}$ recorded at 600 MHz resonance with 100 ms mixing time in lipid membrane. . . . .	79

Figure 4.32: Chemical shift of $C_o$ , $C_\alpha$ , and $C_\beta$ of different residues with respect to random coil $C_r$ in 2D $^{13}\text{C}$ – $^{13}\text{C}$ DARR spectrum of the peptide pEA $\beta_{3-42}$ $^{13}\text{C}$ , $^{15}\text{N}$ –segmentally labeled at $^{36}\text{V}^{37}\text{G}^{38}\text{G}^{39}\text{V}$ recorded at 600 MHz resonance with mixing time 100 ms in lipid membrane. . . . .	79
Figure 4.33: 2D $^{13}\text{C}$ – $^{13}\text{C}$ DARR spectrum of $^{13}\text{C}$ , $^{15}\text{N}$ –uniformly labeled peptide A $\beta_{1-42}$ reconstituted in lipid membrane recorded at 600 MHz resonance with 100 ms mixing time. . . . .	80
Figure 4.34: 2D $^{13}\text{C}$ – $^{13}\text{C}$ DARR spectrum of $^{13}\text{C}$ , $^{15}\text{N}$ –uniformly labeled peptide A $\beta_{1-42}$ reconstituted in lipid membrane recorded at 800 MHz resonance with 25 ms mixing time. . . . .	81
Figure 4.35: 2D $^{13}\text{C}$ – $^{13}\text{C}$ DARR spectrum of $^{13}\text{C}$ , $^{15}\text{N}$ –uniformly labeled A $\beta_{1-42}$ reconstituted in lipid membrane recorded at 800 MHz resonance with 50 ms mixing time. . . . .	82
Figure 4.36: 2D NCA spectra of $^{13}\text{C}$ , $^{15}\text{N}$ –uniformly labeled A $\beta_{1-42}$ recorded at 600 MHz resonance in lipid membrane. . . . .	82
Figure 4.37: 2D NCO spectra of $^{13}\text{C}$ , $^{15}\text{N}$ –uniformly labeled A $\beta_{1-42}$ recorded at 600 MHz resonance in lipid membrane. . . . .	83

## LIST OF TABLES

Table 3.1:	CD Signals of Some Common Secondary Structures . . . . .	19
Table 3.2:	FTIR Wavenumbers of Some Secondary Structures in H <sub>2</sub> O and D <sub>2</sub> O . . . . .	21
Table 3.3:	Excitation Wavelength, Emission Wavelength and Quantum Yield of Three Aromatic Residues in Water (pH 7.0), Taken from [106] and Corresponding Values Under Our Experimental Conditions . . . . .	25
Table 3.4:	Parameters of Some Important Spin 1/2 Nuclei . . . . .	30
Table 4.1:	Binding Parameters Describing the Binding of A $\beta_{25-35}$ to Lipid Vesicles for Aggregation Number $z = 1$ . . . . .	42
Table 4.2:	Binding Parameters Describing the Binding of A $\beta_{25-35}$ to Lipid Vesicles for Aggregation Number $z = 4$ . . . . .	42
Table 4.3:	Binding Parameters Describing the Binding of A $\beta_{25-35}$ to Lipid Vesicles for Aggregation Number $z = 8$ . . . . .	43
Table 4.4:	Orientation of $\beta$ -Strand in Lipid Membrane in Terms of $\beta$ -Angle Under Various Buffer Conditions . . . . .	59
Table B.1:	Concentrations of Membrane Bound Peptide [ $P_b$ ] ( $\mu$ M) at Various Aggregation Numbers: $z = 1$ , $z = 4$ and $z = 8$ . . . . .	90
Table B.2:	Second Order Rate Constant of Pore Formation $k_a$ ( $M^{-1} s^{-1}$ ) at Various Aggregation Numbers: $z = 1$ , $z = 4$ and $z = 8$ . . . . .	91

Table B.3:	Peptide–Peptide Affinity Constant $K_P$ ( $M^{-1}$ ) at Various Aggregation Numbers: $z = 1$ , $z = 4$ and $z = 8$ . . . . .	92
Table B.4:	Oligomeric State (Number of Peptide Oligomers) of the Pore $n$ . . . . .	93
Table B.5:	Concentrations of Membrane Bound Peptide $[P_b]$ ( $\mu M$ ) at Various Aggregation Numbers: $z = 1$ , $z = 4$ and $z = 8$ for Zwitterionic Lipid Vesicles Composed of 90 % POPG and 10 % Cholesterol in Buffer Containing 75 mM NaCl, 30 mM Myo–Inositol, 6 mM $CaCl_2$ , and 20 mM Tris–HCl (pH 7.2) . . . . .	94
Table B.6:	Second Order Rate Constant of Pore Formation $k_a$ ( $M^{-1} s^{-1}$ ) at Various Aggregation Numbers: $z = 1$ , $z = 4$ and $z = 8$ for Zwitterionic Lipid Vesicles Composed of 90 % POPG and 10 % Cholesterol in Buffer Containing 75 mM NaCl, 30 mM Myo–Inositol, 6 mM $CaCl_2$ , and 20 mM Tris–HCl (pH 7.2) . . . . .	94
Table B.7:	Peptide–Peptide Affinity Constant $K_p$ ( $M^{-1}$ ) at Various Aggregation Numbers: $z = 1$ , $z = 4$ and $z = 8$ for Zwitterionic Lipid Vesicles Composed of 90 % POPG and 10 % Cholesterol in Buffer (75 mM NaCl, 30 mM Myo–Inositol, 6 mM $CaCl_2$ , and 20 mM Tris–HCl, pH 7.2) . . . . .	95
Table B.8:	Oligomeric State of the Pore $n$ at Various Aggregation Numbers: $z = 1$ , $z = 4$ and $z = 8$ for Zwitterionic Lipid Vesicles Composed of 90 % POPG and 10 % Cholesterol in Buffer Containing 75 mM NaCl, 30 mM Myo–Inositol, 6 mM $CaCl_2$ , and 20 mM Tris–HCl at pH 7.2 . . . . .	95

Table C.1:	$I_{\beta}/I_{\alpha}$ Values for $A\beta_{1-42}$ Reconstituted in Lipid Membrane in Buffer Consisting of 10 mM Na,K-Phosphate with pD 7.2, in Peptide to Lipid Ratio of $P : L = 1 : 50$ . Lipid Composition is 60 % POPC, 30 % POPG and 10 % Cholesterol . . . . .	97
Table C.2:	$I_{\beta}/I_{\alpha}$ Values for $pEA\beta_{3-42}$ Reconstituted in Lipid Membrane in Buffer Consisting of 10 mM Na,K-Phosphate with pD 7.2, in Peptide to Lipid Ratio of $P : L = 1 : 50$ . Lipid Composition is 60 % POPC, 30 % POPG and 10 % Cholesterol . . . . .	98
Table C.3:	$^{13}\text{C}$ Chemical Shift and FWHM of Pure Lipid and $A\beta_{1-42}$ with $^{13}\text{C}$ Uniformly Labeled Residues in the Region $^{16}\text{K}^{17}\text{L}^{18}\text{V}$ . Lipid Composition is 60 % POPC, 30 % POPG, and 10 % Cholesterol . . . . .	99
Table C.4:	$^{13}\text{C}$ Chemical Shift and FWHM of $A\beta_{1-42}$ and $pEA\beta_{3-42}$ with $^{13}\text{C}$ Uniformly Labeled Residues in the Region $^{36}\text{V}^{37}\text{G}^{38}\text{G}^{39}\text{V}$ in Lipid Membrane. Lipid Composition is 60 % POPC, 30 % POPG, and 10 % Cholesterol . . . .	100
Table C.5:	$^{13}\text{C}$ Chemical Shift and FWHM of Identified Residues of $^{13}\text{C}$ , $^{15}\text{N}$ Uniformly Labeled $A\beta_{1-42}$ in Lipid Membrane. Lipid Composition is 60 % POPC, 30 % POPG, and 10 % Cholesterol at Peptide to Lipid Ratio $P : L = 1 : 25$ . . . . .	101
Table C.6:	Random Coil $^{13}\text{C}$ Chemical Shifts for the 20 Common Amino Acids . . . .	103

## CHAPTER 1: INTRODUCTION

Alzheimer's Disease (AD) is a neurodegenerative disorder characterized by gradual decline in cognitive abilities including memory loss. Despite of extensive research and investment, the central role of amyloid beta ( $A\beta$ ) in Alzheimer's Disease and the molecular mechanism of its toxicity are still controversial. Many clinical trials of AD drug candidates targeting classical neuropathological features of AD have not been successful so far. Most of the experimental works have not been conclusive and *in silico* works have resulted in very divergent models of the  $A\beta$  peptide and its role in AD pathology. These classical lesions also appeared in brains without AD. Moreover, it was also found that about one third of cognitively normal older persons built amyloid plaques in cerebral region. This fact seriously questioned the paradigm of amyloid cascade hypothesis. This has caused a shift in the hypothesis from all  $A\beta$  burden to small soluble toxic oligomers. These intermediates bind to the membrane, assemble into a fixed structure and result in membrane damage, pore/channel formation and calcium dysregulation in neuronal cells. This research is focused to provide molecular details into the formation of pore/channel by  $A\beta$  peptide in phospholipid membranes.

This dissertation work focuses on molecular basis of membranotropic effect of  $A\beta$  peptides using various techniques: fluorescence spectroscopy (FS), Fourier transform infrared spectroscopy (FTIR), circular dichroism (CD), Forster resonance energy transfer (FRET) and solid state nuclear magnetic resonance (ssNMR). The first part is based on characterization of membrane pores formed by an undecapeptide  $A\beta_{25-35}$  with sequence (GSNKGAIIGLM) with a detailed analysis of these structures. The second part presents the analysis of the structure of  $A\beta_{25-35}$  in lipid membrane and the role of cholesterol in pore formation activities of the peptide in the lipid membrane. It also covers some FRET experiments for the detection of aggregation in early stages *i.e.* formation of peptide oligomers that precede fibril formation. The third and final part of this dissertation

summarizes on the conformational changes occurring in peptides  $A\beta_{1-42}$  and  $pEA\beta_{3-42}$  in the presence of lipid membrane.

In the first part, a detailed analysis of  $A\beta_{25-35}$  binding to lipid membranes and resulting pore formation under different salt concentration has been discussed. CD and FTIR were used to analyze the structural changes of peptide in aqueous buffer. Membrane binding mechanism was analyzed using microelectrophoresis data in terms of  $\zeta$ -potential and binding constants. Binding site densities were also calculated using these data. Detailed mode of binding affinity, kinetics of different species of peptides formed during incubation in buffer and in membrane have been presented. Similarly, the membrane permeabilization assay was performed using Quin-2 fluorescence under various conditions of salts and membrane charge. The structure of these pore forming species was monitored using CD under various experimental conditions to find structure and molecular state of these membrane disturbing assemblies.

Second part describes the biophysical techniques used to characterize structure of the pore. The peptide structure in lipid membrane and the effect of varying concentration of cholesterol on the structure and function of the pore was identified. The quantitative analysis of peptide assemblies, structure and oligomeric state of the pore have been presented. The molecular events occurring in the membrane with different cholesterol were analyzed. The order and homogeneity of lipid membrane with peptide incorporated, the orientation of peptide, the mode of calcium transport with different possible structures of pore-assembly have been demonstrated.

The third section covers on FRET experiments designed to capture the oligomeric species of  $A\beta_{1-42}$  before formation of fibrils. Based on the position of phenylalanine (Phe) and tyrosine (Tyr) and also depending on charge and hydrophobicity of residues, different truncation variants of  $A\beta_{1-42}$  were used. The aggregation studies are usually carried out using exogenous fluorophores which are insensitive to early stages of aggregations and might themselves affect fiber formation.

In order to identify segment that initiates aggregation and connect the total pathway of aggregation starting from very early stages to final matured form, we combine FRET between Phe and Tyr, ThT–fluorescence, FTIR and CD measurements.

The final section of this work summarizes the structure–function relationship of  $A\beta_{1-42}$  and  $pEA\beta_{3-42}$  in lipid membrane and associated toxicities. As the amyloid plaque consists of all species of  $A\beta$  peptide including the most dominant  $A\beta_{1-40}$  and more toxic  $A\beta_{1-42}$  and  $pEA\beta_{3-42}$ , the purpose here is to extrapolate the results of the membranotropic effect of shorter variant  $A\beta_{25-35}$  to these full length counterparts. The work is aimed at characterizing the detail tertiary structure of the membrane bound structure and associated pore/channel formation by peptides  $A\beta_{1-42}$  and  $pEA\beta_{3-42}$  in lipid membrane using FTIR and ssNMR. If we can understand the entire mechanism of these different truncation variants along with full length peptides, this would contribute to therapeutic measures for the control of this devastating disease.



## CHAPTER 2: LITERATURE REVIEW

### 2.1 Alzheimer's Disease: Progress and Challenges

Alzheimer's disease (AD) is the main cause of dementia which is characterized by two main lesions; positive lesions of extracellular regions of senile plaques consisting of cross  $\beta$ -sheet conformation of  $A\beta$  peptide [1, 2, 3], cerebral amyloid angiopathy, intracellular deposits of neurofibrillary tangles consisting of phosphorylated tau protein and glial responses accompanied by neuronal and synaptic losses [4, 5, 6, 7, 8, 9, 10]. AD affects millions of people worldwide and is currently incurable. After the discovery of these plaques in the brains of Alzheimer's patients, it was believed that  $A\beta$  burden was the main cause of this disease [4, 11, 12]. This postulate was also referred to as amyloid cascade hypothesis (ACH). This theory assumed that the neurons are badly damaged by the plaques several years before onset of dementia. Amyloid imaging tracers were also developed to track the progression of AD and the role of anti-amyloid therapy in these events [13]. Structure based inhibitors of pathological amyloid fibrils have also been studied to disrupt the fibril formation [14]. It was also shown that increasing the levels of longer amyloid beta over shorter fragments put the individual at higher risk of developing AD without altering the progression time of the disease [15]. However, even after several years of intense research based on this hypothesis, there were no clear indications to support this argument. Instead, people found some buffering role of those plaques [16].

It is reported that abnormal  $A\beta$  processing and resulting deposits of  $A\beta$  is essential but not sufficient for developing Alzheimer's disease [17]. Protein assembly begins in specific regions of the brain and then spreads out to other regions. Another conflicting observation was that about one third of the people who have very normal cognitive abilities developed plaques in cerebral regions [18]. Many clinical trials targeting these classical neuro-pathological features of AD have not

been successful so far [10, 12]. These classical lesions also appeared in brains without AD and sometimes ten to fifteen years before the symptoms of AD. This fact seriously questioned the AD paradigm and put the key role of  $A\beta$  on these molecular events in doubt. It is still not clear whether the amyloid fibrils are the cause of AD pathology or if alternatively, they have a protective function, while the pathological cause is the amyloid membrane disruption activity. Hence the whole mechanism of toxicity still remains controversial. If we can establish a clear experimental evidence elucidating the structure–function relationship of amyloid beta, then the design of molecules able to interact with the amyloid peptides as inhibitors of fibril formation or as inhibitors of amyloid membrane pore formation will constitute a basic approach in the development of anti–Alzheimer therapies [19, 20].

It has now been suggested that well before formation of plaques, smaller forms of oligomers appeared to be toxic to neurons disturbing their communication [9, 21, 22, 23, 24]. However, despite the numerous works supporting the central role of  $A\beta$  oligomers in AD, the exact molecular events of oligomer formation and underlying toxicity are still unclear [25]. Although the formation of ion–channels or amyloid pores have been put forward as AD pathology, the molecular mechanism of pore/channel formation is still lacking. Some studies have suggested the structure of pore as a  $\beta$ –barrel [26, 27] while others have suggested the formation of oligomeric ion channels by self assembly with tilted  $\alpha$ –helical topology [28]. This inconsistency shows that the structure of pore is not known yet. It demands more clarification to resolve this inconsistency by determining the pore structure experimentally with the peptide in a lipid environment rather than *in silico* or in aqueous buffer.

## 2.2 Membrane Interactions of Different A $\beta$ Variants

A $\beta$  peptide is produced from the amyloid  $\beta$  precursor protein (APP) found in neuronal membrane by proteolytic activity of  $\beta$  and  $\gamma$  secretases [29, 30]. Poor sequential specificity of  $\gamma$  secretase results in different A $\beta$  species such as A $\beta_{1-42}$ , A $\beta_{1-40}$ , A $\beta_{25-35}$ , A $\beta_{17-42}$  and so on with A $\beta_{1-40}$  and A $\beta_{1-42}$  being the dominant species. The peptide A $\beta_{1-42}$  has been reported to be less abundant but more toxic than A $\beta_{1-40}$  or any other fragments [22]. The APP post processing pathway is still unclear. A $\beta$  can form a varieties of  $\beta$ -sheet rich aggregates. It has been reported that A $\beta$  oligomers undergo a conformational transition to highly toxic beta sheet structures from initial  $\alpha$ -helical or some random coil structure [31]. Neurotoxicity is believed to be related to different membrane interactions and destabilization processes of those oligomers through membrane permeation and pore formation. Membrane pore formation studies have been done mostly *in silico* and the results are very divergent based on choice of initial peptide structure. The structure reported range from different  $\beta$ -barrel [26, 27] to various  $\alpha$ -helical pores [32, 33, 34, 35, 36, 37]. Tsai et al. [32, 33] and Dies et al. [38] used detergent-solubilized partially  $\alpha$ -helical structure [39, 40]. Fantini and co-workers [34, 35, 36, 37] used  $\alpha$ -helical 25 to 35 stretch of A $\beta_{1-40}$  in micelles [41] while Chang et al. [26] used preformed octameric  $\beta$ -barrel structure.

Other A $\beta$  derivatives including full length peptide have also been reported to form similar pore structure *i.e.*  $\beta$ -barrel models consisting of 12 to 18 subunits for A $\beta_{1-42}$ , A $\beta_{9-42}$ , and A $\beta_{17-42}$  [42, 43]. Tetramers and/or pentamers of 16-stranded  $\beta$ -barrels have been reported for A $\beta_{9-42}$  and A $\beta_{17-42}$  with 64 to 80 peptide monomers in the pore [44]. Similarly, hexamers of 6-stranded  $\beta$ -barrels were also reported for A $\beta_{1-42}$  consisting of 36 monomers [45]. Moreover, A $\beta$  arctic mutant forming pore-like structures with 40 to 60 molecules [46] have also been reported.

The full length A $\beta$  with sequence DAEFRHDSGYEVHHQKLVFFAEDVGSNKGAIIGLMVGGVVIA is an amphiphilic peptide. A $\beta_{1-42}$  has been shown to form globular structures without

fibers in physiological buffer solution for up to 8 h and forms multimeric channel-like structures in a planar lipid bilayer [47]. Petkova et al. have shown a full-length A $\beta$  fibrils consisting of anti-parallel  $\beta$  sheets and  $\beta$  hairpin (around residues 24 to 29) with a bend in residues 23 to 26 [48]. Gremer et al. have revealed a 4 Å resolution cryo-EM structure of A $\beta_{1-42}$  fibrils having LS-shaped topology [49]. On the other hand, A $\beta_{1-40}$  is a truncation mutant obtained by deleting two of the neutral, non-polar aliphatic residues, Isoleucine and Alanine from the C-terminus. This peptide has been shown to have disorder regions,  $\beta$ -sheets and a bend in backbone facilitating side-chains interactions [41]. The hydrophobic interactions are the major causes of amyloid fibrillization. A $\beta_{1-40}$  has been reported to spontaneously associate with anionic liposomes in helical structures and then it converts into  $\beta$ -sheets. This model assumes that  $\beta$ -sheet structure will form disordered regions, and then it will later unwind the membrane-stabilized helical structure [50].

A $\beta_{25-35}$ , sequence Ac-GSNKGAIIGLM-NH<sub>2</sub>, a proteolytic fragment of amyloid beta (A $\beta_{1-42}$ ) has been reported to be the most active among several A $\beta$  variants. It has a very high number of hydrophobic residues and is the shortest fragment. Hence, it has been at the center of focus because of its strong cytotoxicity despite being less abundant [51, 52, 53, 54, 55, 56, 57, 58, 59]. It is also believed that they can form  $\beta$ -sheet aggregates and show similar mechanism of toxicity as full length peptides through DNA damage and apoptosis [60, 61]. It has been shown that cytotoxic effect of A $\beta_{25-35}$  is linked to mitochondrial membrane damage, oxidative stress, cytochrome c release and apoptotic cell death [59, 62, 63, 64]. While A $\beta_{25-35}$  promotes the expression of protein linked to mitochondrial permeability transition pore [65, 66], it also binds to the membrane and forms ion-conducting pores [34, 36, 67, 68, 69, 70]. This peptide also forms voltage dependent channels in the membrane with both cationic and anionic permeability in the order Ca<sup>2+</sup> > K<sup>+</sup> ≥ Na<sup>+</sup> > Cl<sup>-</sup> [67, 69]. In addition to this, A $\beta_{25-35}$  tested on cultured neurons caused maximum increase in intracellular Ca<sup>2+</sup> close to the full length A $\beta_{1-42}$  [70].

This peptide is also reported to assume mixed  $\alpha$ -helix/ $\beta$ -sheet structures in aqueous buffer and  $\beta$ -turns and  $\beta$ -sheet structures at moderate and higher concentration respectively in anionic lipid vesicles [71, 72, 73] with peripheral membrane binding in contrast to membrane insertion activities [74, 75, 76, 77]. Solid state NMR shows that organic phase mixing gives deeper insertion of peptide compared to preformed vesicles [78]. Similarly, neutron diffraction data suggests larger fraction of membrane inserted  $A\beta_{25-35}$  than peripheral for neutral membranes compared to negative membranes [79]. It undergoes transition from random-coil to  $\beta$ -sheet structures much faster depending on the environmental cues [80]. Despite of all these experimental evidences for membrane binding and insertion of  $A\beta_{25-35}$ , the molecular basis of membrane pore formation and underlying structural changes are still elusive.

The peptide  $pEA\beta_{3-42}$  is derived by deleting two N-terminal residues: aspartic acid (D) and alanine (A) and catalyzing the cyclic reaction by using glutaminyl enzyme to convert glutamic acid (E) to pyroglutamic acid (pE). The neuritic plaques consists of up to or even higher than 50 % of  $pEA\beta_{3-42}$  [81]. It is more hydrophobic than  $A\beta_{1-42}$  due to loss of negative charges and the presence of lactum ring in the pE residue. Because of this,  $pEA\beta_{3-42}$  has faster kinetics of self assembly and aggregates much faster and acts as a seed for  $A\beta$  aggregation [82]. This will result in increased interactions with lipid membrane. Large membrane inserted oligomers are reported to induce increased pore activity while adsorbed oligomers produce little or no significant structural damage [83]. Hence membrane inserted species are supposed to be the primary species responsible for membrane permeabilization.

## 2.3 Membrane Pores and Associated Neurotoxicity

### 2.3.1 Calcium Dysregulation

The dysregulation of calcium plays a key role in AD pathology. The level of intra-cellular calcium is believed to control many aspects of neuronal physiology. The calcium signaling by neurons controls many cellular processes including synaptic networks [84, 85]. The calcium hypothesis as shown in Fig. 2.1, is one of the most convincing arguments of AD pathology. The plasma membrane is always under a  $\text{Ca}^{2+}$  concentration gradient. The concentration of calcium in the cytosol at minimal neuronal activity is about  $0.2\ \mu\text{M}$  while the outside calcium is roughly  $1\ \text{mM}$  (almost 5000 times that of cytosol).

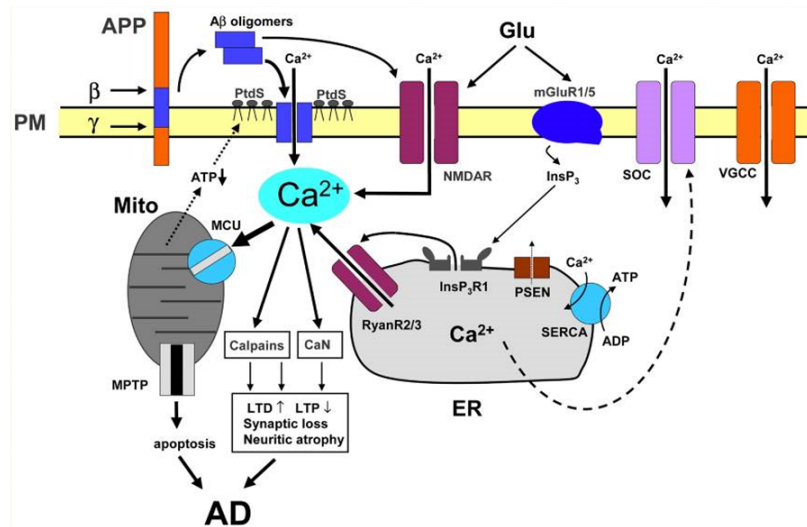


Figure 2.1: Calcium dysregulation in Alzheimer's disease [85].

There are growing evidences that  $A\beta$  oligomers bind to the membrane, forms pores/channels and dysregulates  $Ca^{2+}$  level. This dysregulation is considered to cause neurodegeneration by triggering signaling cascade in Alzheimer's disease. It increases neuronal excitation which triggers aberration of neuronal network, neuronal dysfunction and cell death. In addition, activation of calcineurons (CaN) and calpains causes long term potentiation (LTP), long term depression (LTD), modification of neuronal cytoskeleton, synaptic loss, neuritic atrophy, apoptosis and finally Alzheimer's disease [85].

### 2.3.2 Cholesterol Metabolism

The concentration of cholesterol in neuronal membranes has a profound role in membrane pore formation activities of  $A\beta$  peptides especially because its dual role which can interact both with peptide and lipid membrane depending on concentration. Cholesterol is the most predominant sterol in the neuronal membranes, concentrated in sphingolipid islands called "lipid rafts". Rafts can form only in the outer leaflet of the membrane as the raft composition in the inner leaflet is not possible. They can be very diverse in terms of their function, size, lifetime and composition. They are several angstrom thicker than rest of the bilayer. It is related to lipid fluidity, receptor function, endocytosis, enzyme activity, etc. Glial-derived APOE, a pathological chaperone, is the main cholesterol transporter in the brain [86]. Membrane cholesterol, which regulates  $A\beta$  production and oligomerization, plays a key role in this process [87]. Cholesterol binding to  $A\beta$  may play a role in  $A\beta$  aggregation and cytotoxicity of the peptide, especially with elevated level of cholesterol and its oxidized form [88, 89]. Cholesterol binding region of APP has been shown to encompass  $A\beta_{25-35}$  by nuclear magnetic resonances [90]. Di Scala et al. [28] reported the fragment of residues 22 to 35 of  $A\beta$  is a potential cholesterol binding motif with Val-24 and Lys-28 being very critical for binding that could facilitate the insertion of  $\beta$ -amyloid peptides or amyloid pore/channel formation in cholesterol-rich membrane domains. Cholesterol has been observed to induce a

tilted  $\alpha$ -helical topology of  $A\beta_{22-35}$  with hydrogen bonding between Asn-27 and Lys-28, a key step in the oligomerization of eight  $A\beta_{22-35}$ /cholesterol sub-units to form a perfect annular channel. Xiang et al. reported that increased cholesterol level promotes the binding of  $A\beta$  to the lipid bilayer [87]. Several species of  $A\beta$  have been reported to interact with cholesterol at much higher degree than POPC [34, 35, 36, 91, 92]. This may be the reason of enhanced neurotoxicity of  $A\beta$  in presence of cholesterol [56, 93, 94]. It has also been reported that competitive interaction of cholesterol with  $A\beta_{1-42}$  prevents its aggregation and  $\beta$ -sheet formation and hence inhibiting the membrane disruption activities [95, 96]. Cholesterol was also shown to suppress the toxicity of  $A\beta_{25-35}$  by hindering the formation of pathogenic aggregates [97]. Dual role of cholesterol *i.e.* direct interaction with  $A\beta_{25-35}$  at low concentrations and membrane stiffening effect at high cholesterol has also been reported [98]. However, the mode of interactions between cholesterol and  $A\beta$  are still elusive.



## CHAPTER 3: MATERIALS AND METHODS

### 3.1 Materials

The following chemicals are used in this work. Lipids and cholesterol are ordered from Avanti Polar Lipids (Alabaster, AL). Salts, chemicals, buffers and  $\text{Ca}^{2+}$  ionophore 4-Br-A23187 are from Fisher Scientific (Hanover Park, IL) and Sigma-Aldrich (St. Louis, MO). We ordered all peptides including those truncation variants for FRET studies (synthetic unlabeled) from Peptide 2.0 Inc (Chantilly, VA, USA) and  $^{13}\text{C}$  and  $^{15}\text{N}$ -labeled ones from Innovagen (Lund, Sweden) and rPeptide (Bogart, GA, USA). For the synthesis of  $^{13}\text{C}$ ,  $^{15}\text{N}$ -uniformly labeled full length  $\text{A}\beta_{1-42}$ , labeled amino-acids were purchased from Cambridge Isotope Laboratories, Inc. (Tewksbury, MA) and sent to Peptide 2.0 Inc (Chantilly, VA, USA). Quin-2 was bought from EMD Chemicals (San Diego, CA).

### 3.2 Methods

#### 3.2.1 Fluorescence Spectroscopy

Fluorescence spectroscopy is a widely used technique to study protein folding and aggregation, peptide-membrane interactions, membrane dynamics and many more. Jablonski diagram Fig. 3.1 can be used to explain fluorescence spectroscopy. Electrons can be excited by irradiating molecules with light. They stay in the excited state some time and then return back to the ground state. This process results in light emission, called luminescence. The singlet electrons (excited to singlet state,  $S_1$ ,  $S_2$  with opposite spin) can return quickly to the ground state by emitting photon called fluorescence which usually lasts 10 ns. However, if excited electron happens to be in triplet state

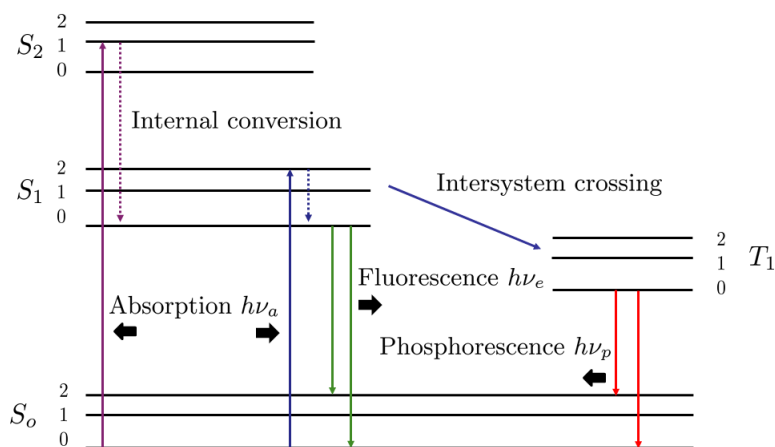


Figure 3.1: Schematic diagram of fluorescence and phosphorescence phenomena.

where electrons have same spin as ground state, they can not come to the ground state easily and they have to spend some time through some non-radiative processes. They spend longer time in those states and finally come to ground state by emitting photons, a process called phosphorescence. Aromatic compounds are well-known for fluorescence. Transition of an electron from the ground state to the excited state creates a large, transient dipole moment, which interacts with the surrounding polar solvent (water) and reorients solvent molecules, an effect known as solvent relaxation. Thus, before returning back to the ground state, the excited electron loses some energy and therefore the emission occurs at a larger wavelength, corresponding to smaller energy compared to excitation. This shift is known as Stokes shift. Emission spectra and Stokes shift can be used to derive the molecular information, solvent polarity, effect of temperature, and phase transition in membranes.

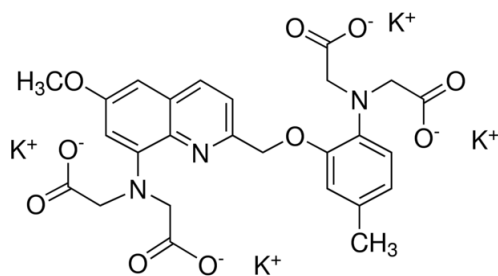


Figure 3.2: Chemical formula of Quin-2 tetrapotassium salt.

Most of the fluorescence assays in this study were done using Quin-2 with structure as shown in Fig. 3.2. Detailed experimental procedures are described in the protocol by Tatulian et al. [99]. Briefly, Quin-2 loaded vesicles were prepared using the method of extrusion. The Quin-2 was excited at wavelength of 339 nm and emission was observed around 492 nm. Fig. 3.4 explains the basic steps for the preparation of desired Quin-2 loaded lipid vesicles. In order to mimic the most common features of lipid membrane, our experiment focused in three main lipids POPC, POPG and cholesterol as shown schematically in Fig. 3.3. First, we mixed different components of lipids as desired in chloroform in a glass vial. Then, we dried the mixture by using gentle nitrogen stream, leave in a desiccator for half an hour before vortexing in a desired buffer. The buffer used is called inside buffer and contains 6 mM Quin-2, 20 mM Tris-HCl with pH 7.2 and different concentrations of KCl as required by the experiment. The vortexing of lipid in buffer produced multilamellar vesicles (MLVs). These MLVs were then extruded through 100 nm polycarbonate membrane to get large unilamellar vesicles (LUVs) loaded with Quin-2. Desalting column as shown in Fig. 3.6 was used for the removal of excess Quin-2 outside the vesicles. Osmotic pressure was balanced across the vesicles membrane by using desired ingredients in the buffer. The working lipid concentration was set at 5 mM. This was done by the use of calibration curve

obtained from light scattering technique [100, 101].

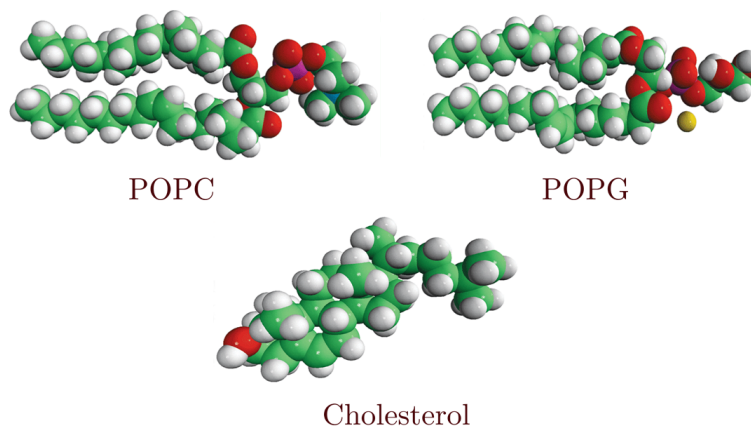


Figure 3.3: Membrane lipid components used in the study: POPC (neutral or zwitterionic lipid), POPG (negative lipid) and cholesterol (non-ionic sterol).

Jasco J-810 spectropolarimeter was used to detect permeation effect of peptide in the membrane. To describe it briefly, using Quin-2 loaded vesicles in quartz cuvette, emission spectra (450 to 600 nm) were observed for about 20 min using the excitation wavelength of 339 nm. The change of fluorescence over time was monitored to discover the mechanism of  $\text{Ca}^{2+}$  transport into the vesicles. Control experiments were also carried out using blank buffer (negative) and ionophore (positive). Temperature was set at  $25^\circ\text{C}$  throughout the experiments. To find the structure of peptide in the membrane, CD measurements were also recorded in the same sample. Using microelectrophoresis, the mode of peptide binding to the lipid membrane was investigated under various conditions using the detail procedure given by Kandel et al. [101].

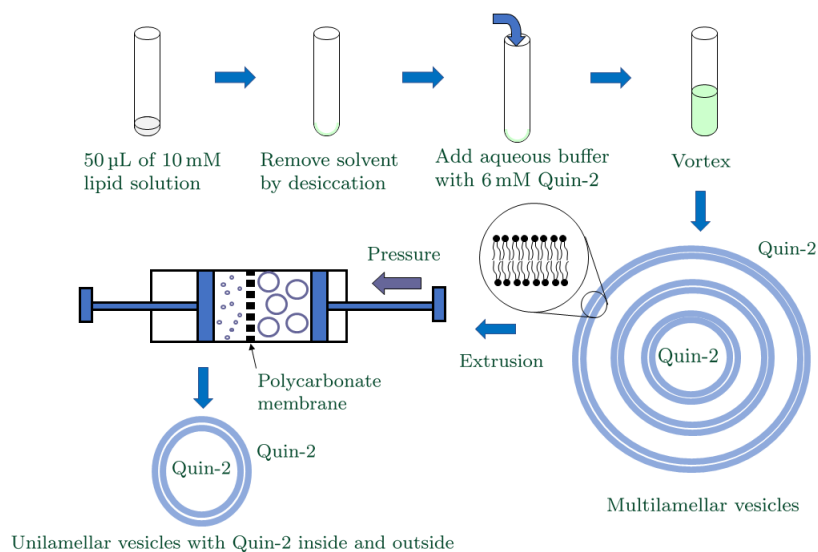


Figure 3.4: Preparation of Quin-2 loaded unilamellar vesicles through extrusion.

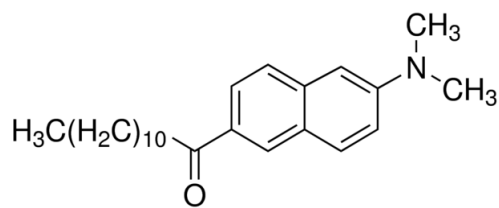


Figure 3.5: Chemical structure of Laurdan.

We measured the generalized polarization (GP) of Laurdan (formula as shown in Fig. 3.5), incorporated in lipid vesicles at 1 mol% to analyze the membrane fluidity. The excitation wavelength was at 360 nm and emission spectra were monitored between 380 and 580 nm. The emission spectra were found shifting depending on membrane fluidity which was then translated into generalized polarization defined as

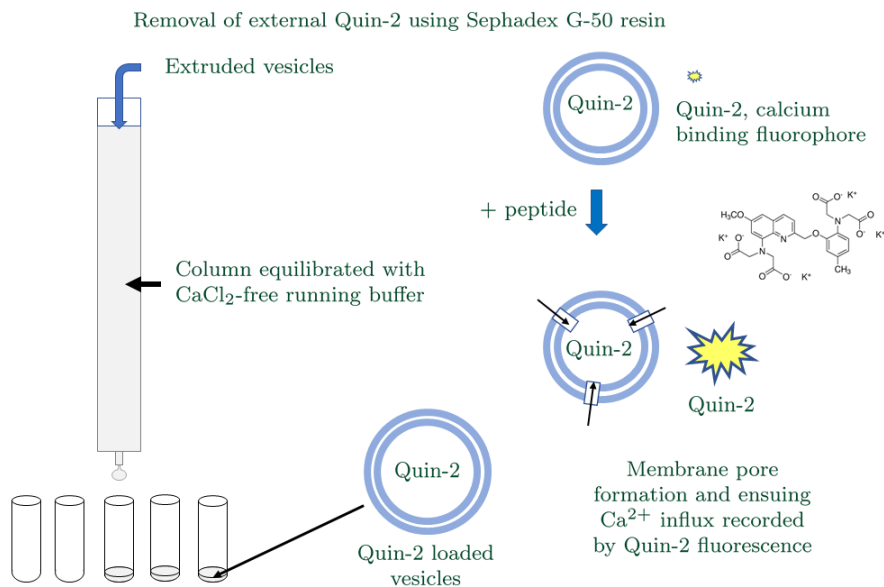


Figure 3.6: Schematic diagram showing how to remove Quin-2 present outside the vesicles by using desalting column.

$$GP = \frac{(F_{435} - F_{500})}{(F_{435} + F_{500})} \quad (3.1)$$

### 3.2.2 Circular Dichroism

Circular Dichroism (CD) is another great ultraviolet absorption technique to identify the secondary structure of protein. It works under the principle of differential absorption of circularly polarized light in two different directions as shown in Fig. 3.7. It uses an UV light source which is converted into circularly polarized light (CPL) once it passes through photo-elastic modulator (PEM). When an optically active molecule *i.e.* chiral center interacts with this CPL, there will be different amount

of absorption of right and left-polarized light and hence results ellipticity graph that will identify the secondary structures of that molecule. This technique has advantages like it can be used for so many different conditions, native or non-native proteins and disadvantages are it doesn't give very good resolution because of signal overlapping and strong light scattering in far UV region.

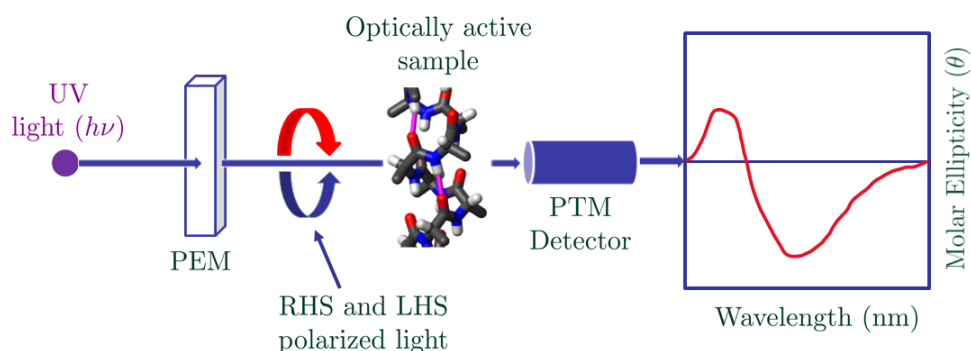


Figure 3.7: Schematic diagram of CD spectroscopy.

CD data were normalized using cell path length  $l$ , number of residues  $n_r$ , molecular weight  $M$  and concentration  $c$  of the sample using the Eq. 3.2.

$$\theta_{mr} = \theta_d \left( \frac{M}{cln_r} \right), \quad (3.2)$$

where  $\theta_{mr}$  is molar ellipticity per residue and  $\theta_d$  is degree ellipticity.

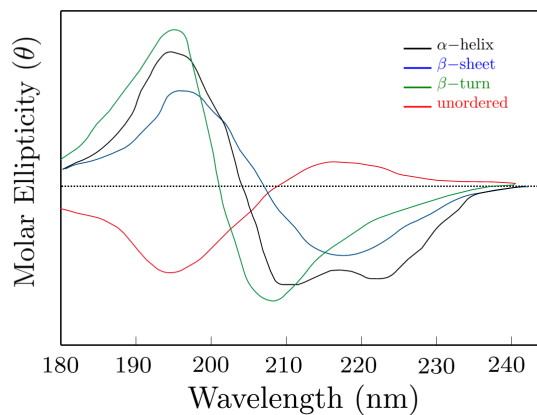


Figure 3.8: CD spectra of  $\beta$ -sheet (blue),  $\alpha$ -helix (black) and random coil or unordered (red).

In this work, CD spectra were recorded in a cuvette ( $4\text{ mm} \times 4\text{ mm}$ ) on the J-810 spectropolarimeter. Depending on the sample conditions, smaller path-length cuvettes 1 mm and 0.5 mm have also been used for precision and accuracy. Some typical CD features are shown in Fig. 3.8.

Table 3.1: CD Signals of Some Common Secondary Structures

Secondary Structure	Positive Peaks	Negative Peaks
$\alpha$ -Helix	194 nm	222 nm, 208 nm
$\beta$ -Sheet	195 nm	216 nm
$\beta$ -Turns	195 nm	208 nm
Disordered Structure	215 nm	195 nm



### 3.2.3 Fourier Transform Infrared Spectroscopy

This is a very sensitive tool to monitor protein conformations. It covers wide range of frequencies but mostly used in amide–I region because of exceptional sensitivity to the secondary structures. The frequency at which a molecule absorbs light depends on the formula and functional group which are different in different molecules. We can also study proton–deuterium exchange using FTIR. There is no light scattering problem in this technique as it is in infrared region [102]. The simple FTIR setup is show in Fig. 3.9. It has mainly three parts, light source (IR), Michelson interferometer with beam splitter and a detector [102]. The splitter splits 50 % of incident light, half goes to rotating mirror and half to other static mirror. They again recombine in the beam

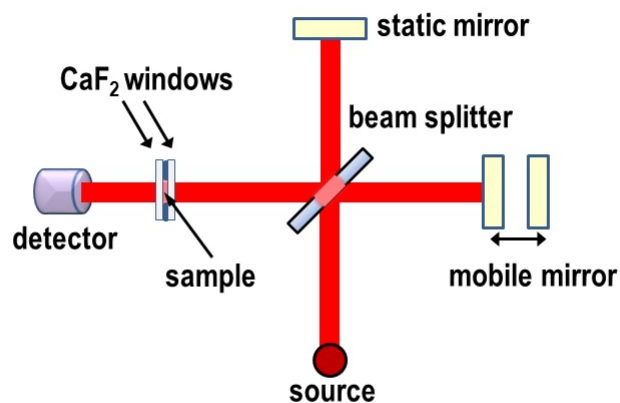


Figure 3.9: Schematic configuration of FTIR spectroscopy [102].

splitter to produce interference. For constructive interference,  $\Delta l = m\lambda$  and for destructive interference,  $\Delta l = (m + \frac{1}{2})\lambda$ , where  $m$  is any integer. Fourier transform is performed on the interferogram to produce transmission spectrum. It will be convenient to convert the transmission into absorption spectrum using Eq. 3.3. Some of the FTIR peaks are shown in Table 3.2 taken from [102].

$$A = -lg\left(\frac{T_s}{T_r}\right), \quad (3.3)$$

where  $T_s$  and  $T_r$  are sample and reference transmissions respectively.

Table 3.2: FTIR Wavenumbers of Some Secondary Structures in H<sub>2</sub>O and D<sub>2</sub>O

Secondary Structure	W <sub>H<sub>2</sub>O</sub> (cm <sup>-1</sup> )	W <sub>D<sub>2</sub>O</sub> (cm <sup>-1</sup> )
$\alpha$ -Helix	1658 – 1647	1655 – 1638
Parallel $\beta$ -Sheet	1638 – 1632	1636 – 1630
Antiparallel $\beta$ -Sheet	1638 – 1632 (strong) and 1695 – 1675 (weak)	1636 – 1630 (strong) and 1680 – 1670 (weak)
Intermolecular (aggregated) $\beta$ -Sheet	1627 – 1615	1625 – 1613
$\beta$ -Turns	1685 – 1655	1675 – 1640
$\gamma$ -Turns	1690 – 1650	1690 – 1650

To perform FTIR measurements, 75  $\mu$ L of sample in 10 mM Na,K-phosphate buffer, pD 7.2 was used in between two CaF<sub>2</sub> window. A Teflon spacer of thickness 50  $\mu$ m was also used between them. Vector-22 spectrometer (Bruker Optics, Billerica, MA, USA) was used for the measurement. This spectrometer has a Hg-Cd-Te detector which has to be cooled by using liquid nitrogen. The data were acquired at 2 cm<sup>-1</sup> resolution at 25 °C and 1000 scans were co-added

for better resolution. Blank buffers were used as references. The data analysis was performed by converting the transmission spectra into absorption spectra for convenience [103]. We also subtracted vapor whenever necessary. The data plotting and analysis was done using IGOR PRO (<https://www.wavemetrics.com/>) and the GRAMS software (<http://www.gramssuite.com>).

### 3.2.4 Attenuated Total Reflection Fourier Transform Infrared Spectroscopy

ATR–FTIR is a surface sensitive substitute for direct FTIR when the sample is not transparent. This technique is basically used to study parameter defining lipid order, lipid and peptide orientations, and so on. This technique is especially useful as sample can be analyzed directly without any further preparations. Fig. 3.10 shows the basic ATR–FTIR components. The working principle of this technique is based on production of evanescent wave as a result of total internal reflection. Germanium is used as an internal reflection element (IRE) to serve this purpose [102].

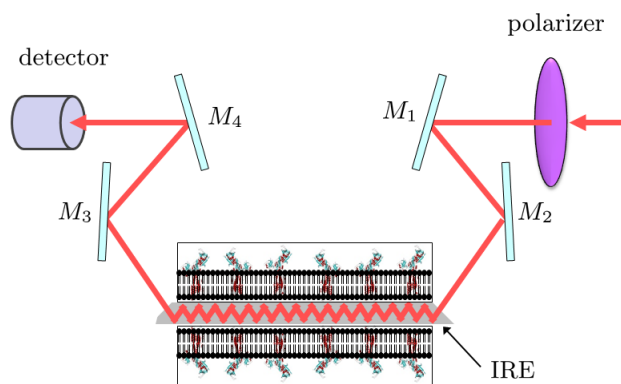


Figure 3.10: Schematic diagram of ATR–FTIR spectroscopy [102].

To perform ATR–FTIR measurements, the peptide  $A\beta_{25-35}$  was incorporated into lipid membrane multilayers. For this, HFIP solutions of peptide and chloroform solutions of lipids were mixed in the ratio  $P : L = 1 : 15$ , the lipid components being the same as used in vesicles leakage experiments *i.e.*  $POPC : POPG : Chol = 0.3 : (0.7 - x_{chol}) : x_{chol}$ . The sample was then spread on a germanium plate ( $5\text{ cm} \times 2\text{ cm} \times 1\text{ cm}$ ) with a cut at the  $2\text{ cm}$  side at an angle of  $45^\circ$  aperture. The sample was air–dried and then desiccated for 1 h. ATR system (Buck Scientific, East Norwalk, CT, USA) was assembled into Victor–22 FTIR spectrometer for measurement. The sample was purged using dry air for 15 min before acquiring transmission spectra. The data were recorded at  $2\text{ cm}^{-1}$  resolution at two different polarizations: parallel ( $\parallel$ ) and perpendicular ( $\perp$ ). The sample was then saturated with  $D_2O$  vapors using a chamber at  $\sim 90^\circ\text{C}$  and the same measurement was done. Finally, another similar measurement was carried out using buffer of 50 mM NaCl, 50 mM Na,K–phosphate in  $D_2O$ , pD 7.2. The references used were the transmission spectra of germanium plate and that of pure multilayer spectra without peptide.

### 3.2.5 Introduction to Forster Resonance Energy Transfer

Forster resonance energy transfer (FRET) or simply (RET) occurs between a fluorophore and some other molecule when they happen to be within a certain distance where the emission spectrum of the donor overlaps with the absorption spectrum of the acceptor [104]. In this situation, the excited energy from the donor will transfer into the acceptor accompanied by enhancement in the emission spectrum of the acceptor. These are the events occurring in the excited states of molecules. The FRET transfer efficiency is determined in terms of distance  $R_o$  between them and the degree of spectrum overlap [106]. The rate of energy transfer depends on the distance between donor and

acceptor and is given by

$$k_t(r) = \frac{1}{\tau_D} \left( \frac{R_o}{r} \right)^6 \quad (3.4)$$

where  $r$  is the distance between donor (D) and acceptor (A).

Similarly the energy transfer between the donor and acceptor pair is given by

$$E = \frac{R_o^6}{R_o^6 + r^6} \quad (3.5)$$

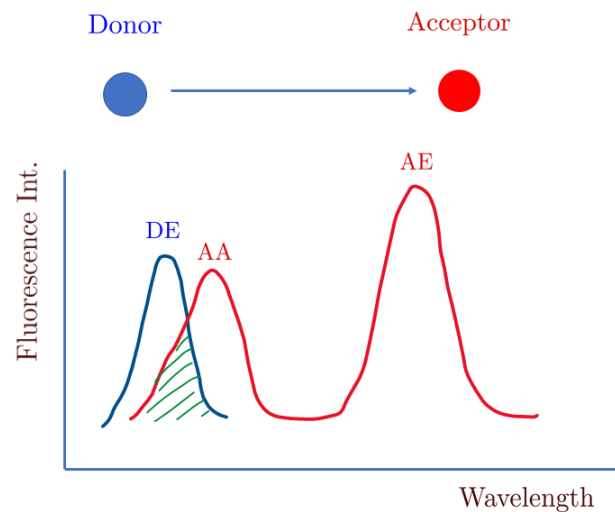


Figure 3.11: Figure showing overlapping of emission spectra of donors and acceptor for FRET. Abbreviations: DE (Donor Emission), AA (Acceptor Absorption), AE (Acceptor Emission).

The Forster distances, fortunately are comparable to the size of macromolecules. They are in the range of 30 Å to 60 Å. This has inspired people to use these energy transfer phenomena as a tool to measure distance between two different sites in a given molecule [105].

Table 3.3: Excitation Wavelength, Emission Wavelength and Quantum Yield of Three Aromatic Residues in Water (pH 7.0), Taken from [106] and Corresponding Values Under Our Experimental Conditions

Amino acid	$\lambda_{ex}$ (nm)	$\lambda_{em}$ (nm)	$\lambda_{ex}^{exp}$ (nm)	$\lambda_{em}^{exp}$ (nm)	$\lambda_{ex}^{opt}$ (nm)	Quantum Yield
Phenylalanine	260	282	265	290	220	0.02
Tyrosine	275	304	278	308	—	0.14
Tryptophan	295	353	0.13	295	—	0.13

In this work, will monitor the energy transfer between phenylalanine (Phe or F) as donor and tyrosine (Tyr or Y) as acceptor. The three fluorescent residues namely phenylalanine (Phe), tyrosine (Tyr) and tryptophan (Trp or W) have their quantum yield in increasing order with Y and W having similar yield. The fluorescence emission from higher yield residues would overshadow the weakest emission spectrum coming from phenylalanine. Fortunately, we do not have tryptophan in  $A\beta_{1-42}$  and hence in any other  $A\beta$  variants peptide. We do have tyrosine (Y) in the sequence which would still act like tryptophan (W) in terms of quantum yield compared to phenylalanine (F). Hence, we have to make sure we are not directly exciting tyrosine while exciting phenylalanine. Normally, this is always the case as they have very similar excitation wavelength around 260 nm and 275 nm as shown in Table 3.3. This selective excitation can be achieved by manually optimizing the excitation wavelength and at the same time looking into the corresponding emission spectrum of tyrosine. These excitation wavelengths can vary slightly depending on temperature, sample condition and solvent polarity. The optimized values for excitation and emission wavelengths of F and

Y, and the optimal excitation wavelength of F without exciting Y *i.e.*  $\lambda_{ex}^{opt}$  under our experimental conditions are as shown in Table 3.3.

For this reason, we have to optimize the excitation wavelength for phenylalanine and tyrosine in the entire region of excitation and emission and come up with a particular excitation wavelength  $\lambda_{ex}$  that will only excite phenylalanine but not tyrosine in the mixture of these fluorescent amino acids. We optimized that  $\lambda_{ex}$  and obtained 220 nm as the optimal value. There will always be some residual excitation which can be subtracted in terms of difference spectrum (DS) defined as

$$DS = 2F_{xy}^{220} - (F_x^{220} + F_y^{220}) \quad (3.6)$$

where  $F_{xy}$  denotes emission spectrum of mixture of two peptides say  $x$  and  $y$  and  $F_x$  or  $F_y$  denotes individual peptide emission when excited at 220 nm. The factor 2 is for dilution correction when two equimolar mixtures are mixed together.

The sample preparation for these FRET experiments was done as described below. Stock solutions of desired peptides at 100  $\mu$ M concentration were prepared in HFIP and stored in refrigerator until use. The desired peptides, either individual or equimolar mixture were transferred into a glass vial, dried with stream of nitrogen and desiccated for 1 h to remove any residual solvent present. The sample was then suspended in desired buffer (25 mM NaCl, 25 mM Na,K–phosphate in H<sub>2</sub>O, pH 7.2) so as to make the working concentration of 100  $\mu$ M. During this suspension process, ThT was also incorporated at 20  $\mu$ M concentration. The dilution correction was made in the case of equimolar mixture. The measurement was done in Jasco J–810 spectropolarimeter using a 4 mm path length quartz cuvette as usual.

### 3.2.6 Principles of Solid State Nuclear Magnetic Resonance

This is one of the most advanced techniques that applies to systems with non zero nuclear spin. Unfortunately, most of the naturally occurring isotopes have no magnetic moment except proton  $^1\text{H}$ . Nuclei of odd numbered—atoms possess both spin and magnetic moments. Most of biological protein samples are diamagnetic materials. In such materials, the magnetic moments are randomly oriented in absence of magnetic field giving no net magnetization. However, when magnetic field is applied to this system, the nuclei interact with the field and align themselves either along the field or opposite to the field. Boltzmann factor  $e^{-\mu H/kT}$  determines the number of population of these states. For a given temperature  $T$  and magnetic field  $H$ , there will be a resultant magnetization in the direction of field as a result of the transitions induced. When another radio frequency field is applied, it will flip the magnetization by desired angle. Once the pulse is removed, the magnetization starts to freely relax back to the original direction. This decaying magnetization will induce an rf current at the Larmor frequency.

Nuclear spin  $I$  is a unique feature of a given nucleus. Because electrons are spinning around the nucleus, they behave like small molecular magnets. For a nucleus with even number of protons and neutrons, the nuclear spin will be zero. Nuclei having sum of protons and neutrons odd will have half integer spin like  $1/2$ ,  $3/2$ ,  $5/2$  and so on. If the number of neutrons and number of protons are both odd, it will give integer spin like 1, 2, 3 and so on. The interaction of nuclear spin with external magnetic field is defined in terms of a number  $m$  called magnetic quantum number written as

$$m = 2I + 1$$

This magnetic quantum number will define different energy splitting in presence of external mag-



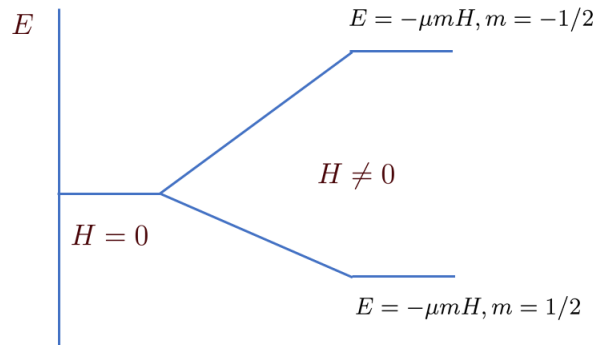


Figure 3.12: Splitting of spectral lines in presence of external magnetic field.

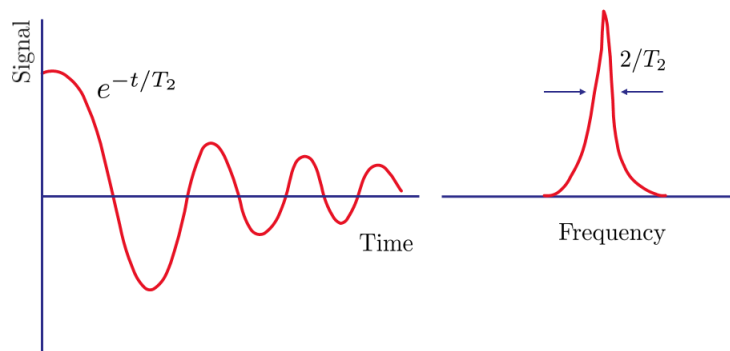


Figure 3.13: Free induction decay and corresponding signal in frequency domain.

netic field as shown in Fig. 3.12.

NMR signal has a characteristic shape and frequency as a result of free precession of magnetic moment. The decay of NMR signal is also called free induction decay (FID). This can be Fourier transformed into frequency domain signal as shown in Fig. 3.13. The effect of static field can be screened by working in a rotating frame about the static field at the nuclear Larmor frequency. The magnetic resonance frequencies for nuclear spins lie in the radio frequency region (electrons spin resonance in microwave region) and hence the process is also called radio frequency spectroscopy.

Due to the orbital motions of electrons, they produce a small magnetic field in the presence of an external magnetic field, and incur a small shift to the actual field experienced by the nucleus. This gives rise to a small shift to the resonance frequency of the nucleus. As the electron orbitals are associated with the chemical environment of the element, this shift is a signature to the chemical bonding and is called chemical shift or chemical shielding denoted by ( $\delta$ ). It is measured in parts per million (ppm) and is defined as

$$\delta = \frac{\nu - \nu_o}{\nu_o} \times 10^6, \quad (3.7)$$

where  $\nu$  is for the sample and  $\nu_o$  for the reference. A number of compounds can be used as standards e.g. tetramethylsilane (TMS) for  $^1\text{H}$  and  $^{13}\text{C}$  nuclei and so on.

Just like a dipolar moment, the external field  $\mathbf{H}$  will exert a torque on the magnetic moment  $\boldsymbol{\mu}$  of the nucleus given by

$$\frac{d\mathbf{J}}{dt} = \boldsymbol{\mu} \times \mathbf{H}. \quad (3.8)$$

Magnetic moment and angular momentum vectors are related as

$$\boldsymbol{\mu} = \gamma \mathbf{J}, \quad (3.9)$$

where  $\gamma = (ge/2mc)$  is the gyromagnetic ratio of the given nucleus and depends on mass of the nucleus,  $g$  is the  $g$ -factor and is approximately 2. Some important values are given in the Table 3.4.

Table 3.4: Parameters of Some Important Spin 1/2 Nuclei

Nucleus	Resonance (MHz) at 14.1 T	Natural abundance	Gyromagnetic ratio (MHz T <sup>-1</sup> )
<sup>1</sup> H	599.834	99.998 %	42.578
<sup>13</sup> C	150.845	1.121 %	10.709
<sup>15</sup> N	60.834	0.453 %	-4.312
<sup>31</sup> P	242.938	100 %	17.24

From Eqs. 3.8 and 3.9, we have

$$\frac{d\boldsymbol{\mu}}{dt} = \boldsymbol{\mu} \times (\gamma \mathbf{H}) = \boldsymbol{\mu} \times \boldsymbol{\omega}. \quad (3.10)$$

The equation 3.10 tells that the magnetic moment vector precesses around magnetic field direction at an angle  $\theta$  generating a cone. This precession frequency which is needed for magnetic resonance absorption is called Larmor's frequency  $\omega_o$  given by the Eq. 3.11. This equation tells that it

requires higher magnetic field to get stronger resonance for a given isotope.

$$\omega_o = \gamma \mathbf{H}_o. \quad (3.11)$$

After the pulse is removed, the magnetization decays as the system comes back to equilibrium. The magnetization will start dephasing in  $x-y$  plane because of the field inhomogeneity and spin–spin relaxation while it returns gradually to thermo–equilibrium distribution along  $z$  direction following spin–lattice relaxation. Bloch equations can be used to describe the recovery phenomena:

$$\frac{dM_z}{dt} = \frac{M_o - M_z}{T_1} + \gamma(M \times H)_z \quad (3.12)$$

$$\frac{dM_x}{dt} = \gamma(M \times H)_x - \frac{M_x}{T_2} \quad (3.13)$$

$$\frac{dM_y}{dt} = \gamma(M \times H)_y - \frac{M_y}{T_2}, \quad (3.14)$$

The decay rate is  $\sim e^{-t/T_2}$  and the recovery is given by

$$M_z = M_o [1 - e^{-\frac{t}{T_1}}]. \quad (3.15)$$

For the ssNMR experiment, two different sample preparation methods were used, aqueous phase mixing and organic phase mixing [107]. In the first procedure with peptides  $A\beta_{1-42}$  and  $pEA\beta_{3-42}$  that are  $^{13}\text{C}$ ,  $^{15}\text{N}$ –segmentally labeled at  $^{16}\text{K}^{17}\text{L}^{18}\text{V}$  and  $^{36}\text{V}^{37}\text{G}^{38}\text{G}^{39}\text{V}$ , each labeled peptide sam-

ples were reconstituted in lipid membrane with 60 % POPC, 30 % POPG and 10 % cholesterol in the peptide to lipid molar ratio of  $P : L = 1 : 25$ . Stock solutions of peptides each ( $\sim 6$  mg) were prepared in 250  $\mu\text{L}$  of HFIP. All the lipid stocks (POPC, POPG and cholesterol) at 44.3 mM concentration were prepared in chloroform. Desired volumes of POPC, POPG and cholesterol were mixed in a glass vial and then transferred to the stock peptide. The mixture was then vortexed for 5 s to 10 s to ensure homogenous mixing. The solvent was then dried using nitrogen stream and then desiccated for 30 min to remove any residual solvent. Final suspension was prepared in 2 mL phosphate buffer (10 mM Na,K-phosphate, pD 7.2) by vortexing the sample vigorously for 5 to 10 min. This resulted in peptide reconstituted multilamellar vesicles (MLVs). These MLVs were extruded using 200 nm polycarbonate filter as described earlier [101]. The extruded sample was then ultra-centrifuged at 200 000 g for 3 h at 24 °C using Beckman Coulter Optima TLX benchtop Ultracentrifuge. The supernatant was carefully removed and the pellet was transferred to 3.2 mm, 36  $\mu\text{L}$  (MAS) rotor for NMR measurements. The peptide concentration in supernatant and the pellet was measured using NanoDrop spectrophotometer before packing into the MAS rotor.

In the second set of sample preparation, method of organic phase mixing was used. The purpose was to enhance the signal noise and spectral quality without changing the final conditions of peptide-incorporated lipid vesicles [107]. In this method, desired concentration of peptide (especially used for pEA $\beta_{3-42}$  that is  $^{13}\text{C}$ ,  $^{15}\text{N}$ -segmentally labeled at  $^{36}\text{V}^{37}\text{G}^{38}\text{G}^{39}\text{V}$  and  $^{13}\text{C}$ ,  $^{15}\text{N}$ -uniformly labeled A $\beta_{1-42}$ ) in HFIP and lipids in chloroform were mixed gently in a glass vial so that the final peptide to lipid molar ratio became  $P : L = 1 : 25$ . The mixture was then dried using nitrogen stream. Then, the sample was placed in a desiccator overnight to make sure all organic solvents were evaporated. Finally, the whole sample was again dissolved in cyclohexane. After it was completely dissolved in cyclohexane, we lyophilised the sample for 12 h. The final lyophilized sample was then packed into 3.2 mm, 36  $\mu\text{L}$  (MAS) rotor followed by hydration using 27  $\mu\text{L}$  of buffer for NMR measurements.

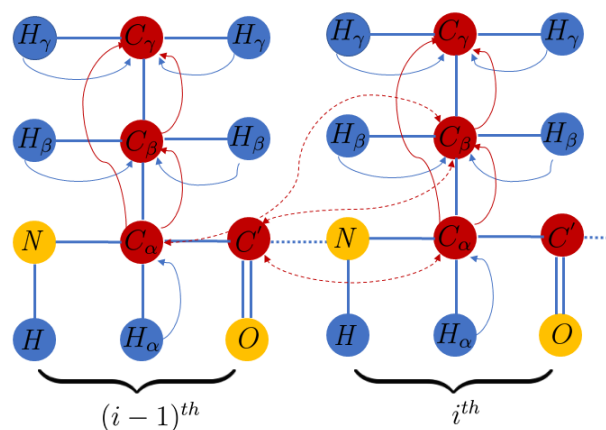


Figure 3.14: Schematic diagram of DARR mixing. This resonance can connect either intra-residues or inter-residues depending on mixing time.

NMR spectra were acquired on a 600 MHz (14.1 T) Agilent spectrometer with a triple resonance 3.2 mm magic angle spinning (MAS) probe at 13.5 kHz MAS. Two-pulse-phase-modulated (TPPM) [108, 109] decoupling of 95 kHz was applied on proton. The rf fields during cross polarization (CP) [110] were 50 kHz and 36.5 kHz on carbon and proton respectively. In two-dimensional carbon-carbon correlation spectra acquisition, 50 ms dipolar-assisted rotational resonance (DARR) [109] was used with indirect dimension spectral width of 33 kHz and complex points 128. All the measurements were done at 4 °C to minimize the effect of internal heating to the sample due to radio frequency fields, especially coming from the long decoupling in salty hydrated sample. Depending on assignments, sample was also sent to National High Magnetic Field Laboratory, (NHMFL), Tallahassee, FL where measurements were carried out on a Bruker, 800 MHz mag-

net. The spectra were processed using NMRpipe and plotted with NMRFAM–SPARKY [111] and UCSF–SPARKY3 (University of California, San Francisco). The chemical shift values were referenced based on tetramethylsilane (TMS).

Solid state NMR is different than liquid state NMR because the anisotropy will not average out from the molecular tumbling unlike in the liquid phase. And because of this anisotropy, the resonance line is broadened and resolution will be diminished. We can effectively suppress those anisotropies by spinning the sample at a fixed angle called magic angle  $54.7^\circ$  and decoupling the protons from carbons. Because most of the naturally occurring isotopes like  $^{12}\text{C}$  have no magnetic moment, they have to be isotopically replaced by active nuclei like  $^{13}\text{C}$  and  $^{15}\text{N}$  which can be achieved either by recombinant protein synthesis or by expression and purification in bacterial medium. To enhance sensitivity, techniques such as cross polarization (CP) are commonly used. This technique has another advantage over direct excitation: it detects only rigid segments while the direct excitation detects all possible signals rigid and flexible.

The initial sample and spectral quality can be checked using 1D CP MAS and 2D–CC dipolar assisted rotational resonance (DARR) with different mixing times like 25 ms and 50 ms. Sequential assignment can be used to analyze secondary structures and dynamics. To check the signal resolution, 2D–NCOCX and 2D–NCACX spectra can be acquired. If there are ambiguities in the assignment, then 3D–NCACX and 3D–NCOCX can be performed which will most likely resolve the congestion to identify the residues if the line width is near or less than 1 ppm. The longer mixing times 2D and 3D experiments can be used to probe tertiary and quaternary constraints. The qualitative distance constraints can be achieved by using PITHIRDS [112] and REDOR [113] sequences.

### 3.3 Theoretical Prospective of Membrane Binding and Pore Formation

Gouy–Chapman–Stern theory is used to analyze membrane binding parameters based on  $\zeta$ –potential measurement described elsewhere [114]. In what follows, a briefly summary of the theory is presented with symbols having their usual meanings. The total surface charge density in vesicle membrane is written as

$$\sigma = \sigma_o + \sigma_b, \quad (3.16)$$

where  $\sigma_o$  is the intrinsic charge density of lipid and  $\sigma_b$  is from peptide binding to membrane.

The Gouy–Chapman equation can be used to find total surface charge density  $\sigma$  (for 1 : 1 electrolyte) as

$$\sigma = \sqrt{8\epsilon\epsilon_o RT C} \operatorname{sh}\left(\frac{F\psi_o}{2RT}\right), \quad (3.17)$$

The  $\zeta$ –potential can be expressed as

$$\zeta = \psi_o e^{-\delta/\lambda}, \quad (3.18)$$

$$\lambda = \sqrt{\frac{\epsilon\epsilon_o RT}{F^2 \sum z_i^2 C_i}}, \quad (3.19)$$



The bound surface charge density due to peptide  $\sigma_b$  is expressed as

$$\sigma_b = \frac{ze[P_b]}{\gamma[L]A_{lipid}}, \quad (3.20)$$

Membrane-binding is a bi-molecular process [117]. Following the theory described earlier [101], the membrane binding isotherm can be written as

$$\sigma_o + \frac{ze}{\gamma[L]A_{lipid}}(a - \sqrt{a^2 - b}) = \sqrt{8\epsilon\epsilon_o RT C} sh\left(\frac{F\psi_o}{2RT}\right) \quad (3.21)$$

Using Eq. 3.21, with experimentally determined values of  $\zeta$ -potential, we constructed theoretical binding isotherms for various aggregations numbers like  $z = 1$ ,  $z = 4$ , and  $z = 8$ . Finally, the membrane binding and pore formation mechanism was analyzed based on theoretical framework previously described [100].

### 3.4 FTIR Data Analysis

#### 3.4.1 Secondary Structures Determination

FTIR and ATR-FTIR techniques can be used for the analysis of the secondary structures of peptide incorporated in lipid vesicles or in supported lipid bilayers. The detail procedure for structural characterization is described elsewhere [102]. Briefly, to analyze the structure and orientation of membrane-bound peptide, ATR-FTIR spectra were recorded at two different polarization, parallel ( $\parallel$ ) and then perpendicular ( $\perp$ ). The spectra were then converted into polarization independent

spectrum using the relation

$$A = A_{\parallel} + GA_{\perp}, \quad (3.22)$$

where  $G$  is the scaling factor given by

$$G = \frac{2E_z^2 - E_x^2}{E_y^2}. \quad (3.23)$$

The polarization independent amide I area was determined by using the relation

$$a_i = \frac{a_{i,\parallel} + Ga_{i,\perp}}{a_{total,\parallel} + Ga_{total,\perp}}, \quad (3.24)$$

where  $a_{total,\parallel}$  and  $a_{total,\perp}$  are total amide I areas at  $\parallel$  and  $\perp$  polarization respectively corrected by subtraction of side-chain component.

The GRAMS software was used to do curve-fitting and to calculate fraction of secondary structure by using the relation

$$f_i = \frac{a_i}{\epsilon_i \left( \frac{a_{\alpha}}{\epsilon_{\alpha}} + \frac{a_{\beta}}{\epsilon_{\beta}} + \frac{a_t}{\epsilon_t} + \frac{a_{\rho}}{\epsilon_{\rho}} \right)}. \quad (3.25)$$

### 3.4.2 Orientation of Peptides

ATR–FTIR spectroscopy can be used to analyze the orientation of membrane–bound peptides. For a given structure with a molecular axis, the orientation order parameter is defined as

$$S = \frac{2B}{(3\langle \cos^2 \alpha \rangle - 1)(B - 3E_z^2)}, \quad (3.26)$$

where,  $\alpha = 38$  to  $40^\circ$  for  $\alpha$ –helix.

For lipid acyl chain in all–trans conformation, the angle between  $\text{CH}_2$  stretching vibrations and the chain axis is  $90^\circ$  [102, 118, 119], hence from Eq. 3.26, we can write

$$S = \frac{2B}{(3E_z^2 - B)}. \quad (3.27)$$

The angle  $S$  between the membrane normal and the molecular axis is given by

$$S = \frac{1}{2}(3\langle \cos^2 \theta \rangle - 1). \quad (3.28)$$

The  $\beta$ –strand orientation is more difficult to calculate unless strands are arranged in central symmetry about the rotational axis. Then, the orientation of the  $\beta$ –strands is given by [119]

$$\frac{1}{2}(3\langle \sin^2 \beta \rangle - 1) = \frac{2B}{(3\langle \cos^2 \gamma \rangle - 1)(B - 3E_z^2)}. \quad (3.29)$$

Knowing the angle  $\gamma$  between pore axis and membrane normal and the dichroic ratio  $R_i$ , we can calculate the angle  $\beta$ , the angle between strand axis and the central axis of the pore.

## CHAPTER 4: RESULTS

### 4.1 Salt Dependent Membrane Binding and Pore Formation by $A\beta_{25-35}$

In this section, the detailed analysis of  $A\beta_{25-35}$  binding to membrane and resulting pore formation under various salt conditions and different lipid compositions is described. Several parameters were calculated which enabled us to find the detail structure of the pore.

#### 4.1.1 $A\beta_{25-35}$ Peptide in Aqueous Buffer

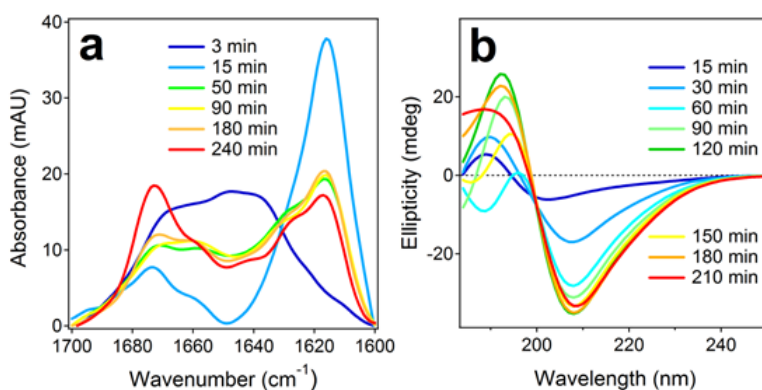


Figure 4.1: FTIR (a) and CD (b) structures of  $A\beta_{25-35}$  in aqueous buffer. FTIR measurements were done in buffer of 50 mM Na,K-phosphate, 50 mM NaCl, pD 7.2 and CD measurements were carried out in Tris buffer (145 mM NaCl, 50 mM Tris, pH 7.2).

We used CD and FTIR to analyze the structural change of peptide in aqueous buffer (145 mM NaCl and 50 mM Tris-HCl, pH 7.2). The CD data showed a gradual change of conformation from unordered structure to type-I  $\beta$ -turn as we incubated the peptide in the buffer. In about 2.5 h, the

transition saturated. FTIR data revealed that the initial structure was unordered and  $\beta$ -turns which then changed to intermolecular  $\beta$ -sheet in about 15 min after putting in aqueous buffer (50 mM NaCl and 50 mM Na,K-phosphate, pD 7.2) as shown in Fig. 4.1. These data suggest that  $A\beta_{25-35}$  assumes heterogeneous conformations, mostly of  $\beta$ -sheet and  $\beta$ -turn [101].

#### 4.1.2 Binding of $A\beta_{25-35}$ Peptide to Lipid Membrane

In order to understand the membrane binding mechanism, we used microelectrophoresis to measure  $\zeta$ -potential of lipid vesicles before and after addition of peptide. The peptide was incubated for 2.5 h in aqueous buffer and added to anionic vesicles with composition 60 mol % POPC, 30 mol % POPG and 10 mol % cholesterol. This lipid composition makes the overall charge of the membrane negative while peptide has a positive charge of Lys<sup>28</sup>. When we increased the peptide concentration, the negative  $\zeta$ -potential of vesicles was reduced. This confirmed membrane binding as shown in Fig. 4.2. As we increased the concentrations of NaCl in the buffer, the peptide binding and surface potential of vesicles were both decreased. This suggested an important role of electrostatics in membrane-peptide interactions.

Using the data at different ionic concentrations, we found that vesicles had a layer of bound water molecules which is consistent with a shear layer thickness of 3 Å [101]. Moreover, the saturation of  $\zeta$ -potential at higher concentration of peptide as shown in Fig. 4.2 (a – c) suggested that peptide binding site has limited surface area available. Using cross sectional area 59 Å<sup>2</sup> for POPC and POPG and 23 Å<sup>2</sup> for cholesterol [120, 121], we found that  $A_{lipid} = 55.4 \text{ Å}^2$ . The detail calculation procedure is described in [101]. The binding curves for  $z > 8$  went out of experimental range as shown in Fig. 4.2 (a – c). This suggested that either there were no larger particles or they didn't bind to the membrane.

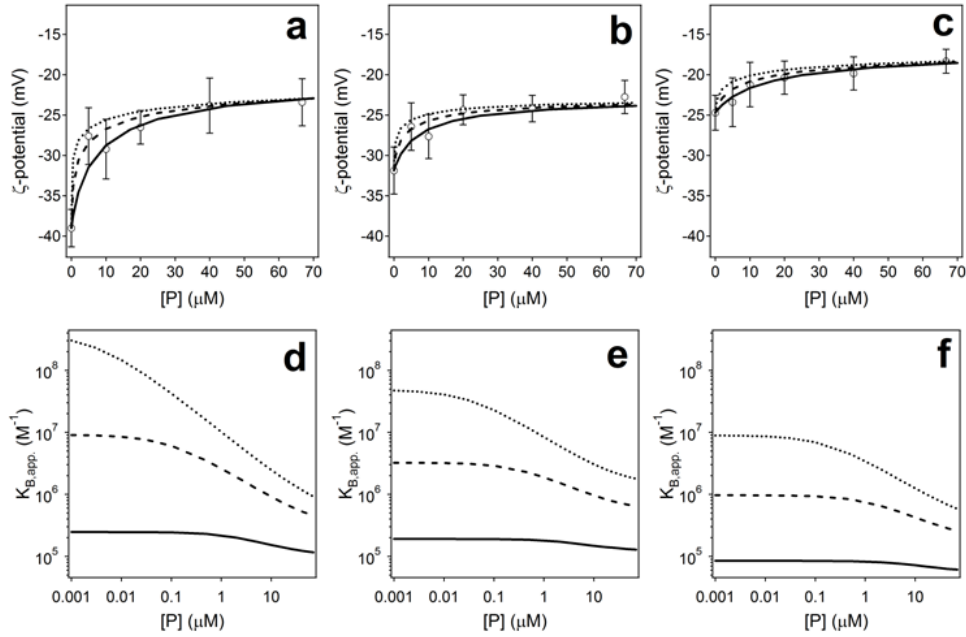


Figure 4.2:  $\zeta$ -potential of lipid vesicles as a function of added peptide at different salt (NaCl) concentrations: 10 mM (a), 30 mM (b), and 75 mM (c) in Tris-HCl buffer (20 mM, pH 7.2). Solid, dashed and dotted lines represent theoretical plots for aggregation numbers of  $z = 1$ ,  $z = 4$ , and  $z = 8$  respectively. The corresponding variation of binding constants (apparent) are shown in panels (d – f). The working lipid concentration is 0.2 mM with membrane molar composition of 60 % PC, 30 % PG and 10 % cholesterol.

This peptide  $A\beta_{25-35}$  has been shown to form soluble oligomers at shorter times [122]. The peptide assemblies contained monomers to octamers during incubation in buffer. The number of lipids per unit binding site  $N_L$  and intrinsic dissociation constants  $K_D$  were calculated using the surface charge and area of lipid. We were able to calculate that 25 to 40 lipid molecules are required for a monomer-binding site. This number was found to be directly proportional to the aggregation number. Similarly, the dissociation constants for different species *i.e.* monomers, tetramers and

octamers were calculated to be  $2.5 \times 10^{-5}$  M to  $4.4 \times 10^{-5}$  M,  $1.6 \times 10^{-4}$  M to  $2.0 \times 10^{-4}$  M and  $4.2 \times 10^{-3}$  M to  $5.6 \times 10^{-3}$  M respectively. The detail parameters are given in Table 4.1, 4.2, and 4.3 respectively.

The apparent binding constants corresponding to zeta potential measurements ( $a - c$ ) were plotted as shown in Fig. 4.2( $d - f$ ). These constants were evaluated by using measured zeta potentials and dissociation constants given in Table 4.1, 4.2, and 4.3. The binding constants are seen decreasing with increasing salt concentrations. These apparent binding constants are higher for higher peptide assemblies as shown in Fig. 4.2( $d - f$ ). They are in range of data reported earlier [80].

Table 4.1: Binding Parameters Describing the Binding of  $A\beta_{25-35}$  to Lipid Vesicles for Aggregation Number  $z = 1$

NaCl (mM)	$\sigma_o$ (mC m <sup>-2</sup> )	$K_D$ (M)	$N_L$
10	-21.19	$2.5 \times 10^{-5}$	26.3
30	-22.70	$2.5 \times 10^{-5}$	40.5
75	-25.61	$4.4 \times 10^{-5}$	33.5

Table 4.2: Binding Parameters Describing the Binding of  $A\beta_{25-35}$  to Lipid Vesicles for Aggregation Number  $z = 4$

NaCl (mM)	$\sigma_o$ (mC m <sup>-2</sup> )	$K_D$ (M)	$N_L$
10	-21.19	$1.6 \times 10^{-4}$	105.1
30	-22.70	$1.6 \times 10^{-4}$	161.8
75	-25.61	$2.0 \times 10^{-4}$	134.0

Table 4.3: Binding Parameters Describing the Binding of  $A\beta_{25-35}$  to Lipid Vesicles for Aggregation Number  $z = 8$

NaCl (mM)	$\sigma_o$ (mC m <sup>-2</sup> )	$K_D$ (M)	$N_L$
10	-21.19	$5.6 \times 10^{-3}$	210.2
30	-22.70	$5.6 \times 10^{-3}$	323.6
75	-25.61	$5.6 \times 10^{-3}$	268.0

#### 4.1.3 Membrane Permeabilization Effect of Peptide

In this assay, we tested the effect of peptide on membrane permeabilization using anionic and zwitterionic lipids. The peptide was first incubated in the same buffer for 2.5 h before adding to the lipid vesicles. We first tested the controls, calcium ionophore as positive and buffer as negative. Addition of ionophore resulted in a strong Quin-2 fluorescence while buffer alone didn't cause any fluorescence as shown in Fig. 4.3. This confirmed that our lipid vesicles system is intact and fully functional. The effect of peptide at low ionic strength was over 50 % that of positive control. The time constant was calculated to be 0.33 min to 1.67 min. The effect was greatly reduced as we increased the salt concentration in the buffer. The rate constant reached over 30 min with high salt concentration  $\geq 180$  mM. This confirmed again that the electrostatic screening is the leading phenomena in these processes in which counterions collect in between the positively charged peptide and negatively charged membrane and reduce the effective charge of attraction. These data agree with earlier reported studies [80].



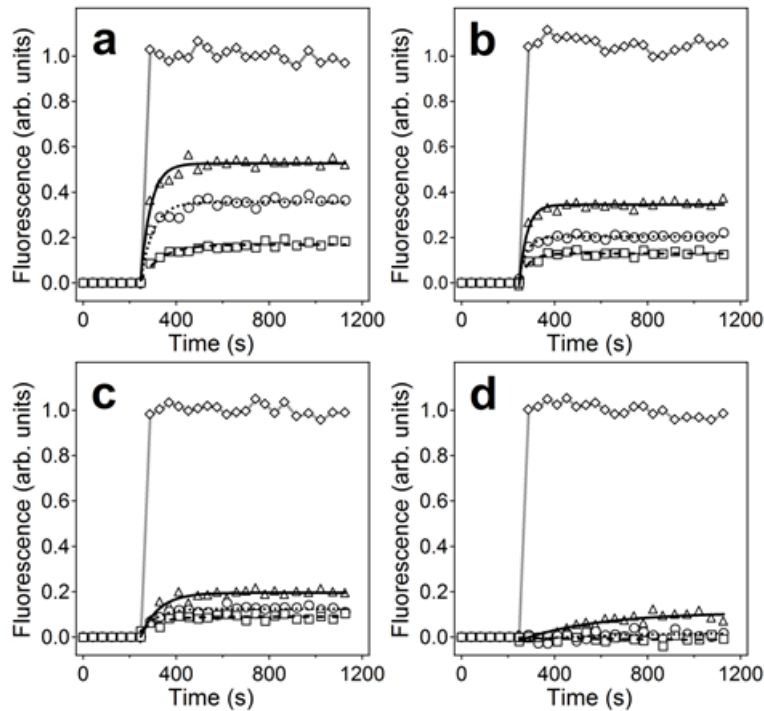


Figure 4.3: Quin-2 fluorescence as a function of time due to influx of  $\text{Ca}^{2+}$  at different salt concentrations: 30 mM (a), 75 mM (b), 150 mM (c) and 180 mM (d). Squares, circles and triangles represent  $P : L = 1 : 10$ ,  $1 : 5$  and  $1 : 3$  and rhombs represent effect of ionophore as positive control. The working lipid concentration is 0.2 mM with membrane molar composition of 60 % PC, 30 % PG and 10 % cholesterol. All data are normalized to unity based on the maximum effect of ionophore.

Based on the Quin-2 fluorescence assay experiment shown in Fig. 4.4, we can say that membrane permeation effect of  $A\beta_{25-35}$  depends bi-phasically on ionic strength of the buffer. The rate constant increased with increasing ionic concentrations of buffer up to 100 mM to 150 mM and then decreased. This dual effect is the result of electrostatic screening from counterion accumulation. At high ionic concentration, peptide-peptide interactions is dominant and peptide-membrane in-

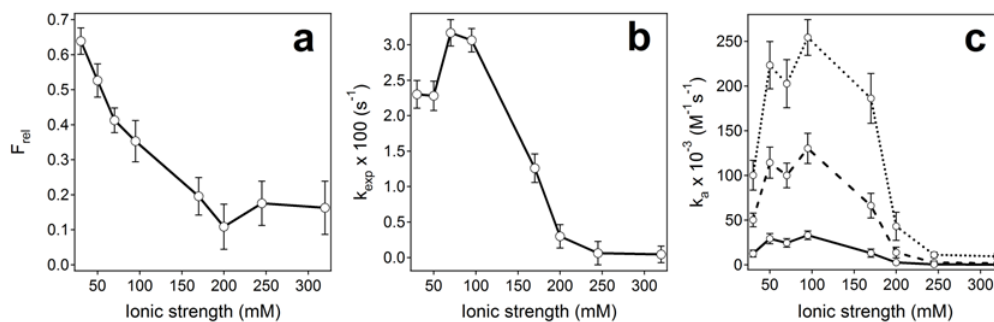


Figure 4.4: Relative Quin–2 fluorescence intensity as a function of salt in buffer (a), single exponential rate constant as a function of salt in buffer (b), and second order rate constant of pore formation as a function of salt in buffer (c). Solid ( $z = 1$ ), dashed ( $z = 4$ ) and dotted ( $z = 8$ ) lines represent theoretical isotherms respectively. The working lipid concentration is 0.2 mM with membrane molar composition of 60 % PC, 30 % PG and 10 % cholesterol. Peptide concentration is 66.7  $\mu\text{M}$ .

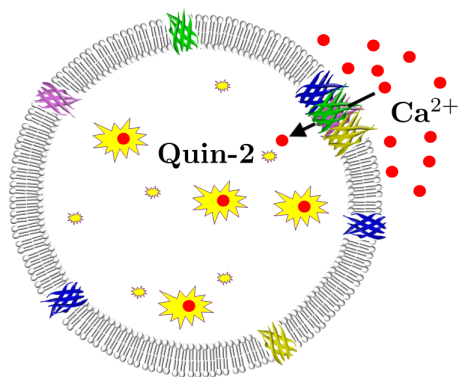


Figure 4.5: Model of lipid vesicles with Quin–2 entrapped inside and illustration of membrane permeation, pore formation, calcium influx and Quin–2 fluorescence enhancement.

teractions is decreased. We identified two different pore populations. At low salt  $\leq 50$  mM, the population consisted of 3 to 5 peptide units while at high salt concentrations  $\geq 75$  mM, 7 to 9 peptide units were found. The functional pores were oligomers of oligomers *i.e.* hexamers of hexamers or octamers of octamers.

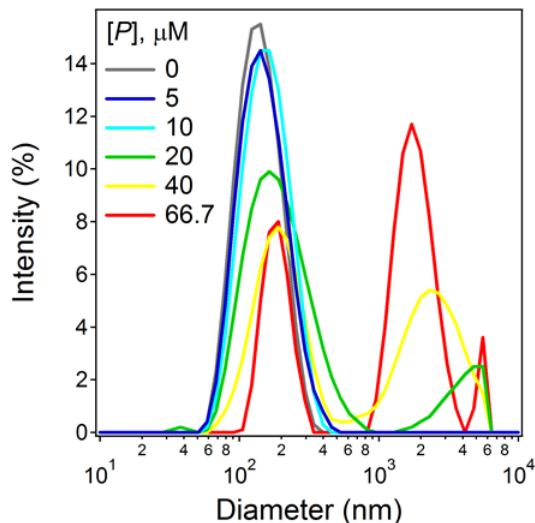


Figure 4.6: Size distribution of lipid vesicles as a function of peptide concentration shown using dynamic light scattering. The working lipid vesicle concentration is 0.2 mM with membrane molar composition of 60 % PC, 30 % PG and 10 % cholesterol.

Moreover, this assay also shows that the Quin–2 fluorescence  $F_{rel}$  never reached the effect of  $Ca^{2+}$  ionophore as shown in Fig. 4.3. To validate this phenomena, we used dynamic light scattering to find size distribution of vesicles in presence of peptide as shown in Fig. 4.6. The result is highly poly–dispersed especially at higher peptide concentrations. The peak at about 130 nm is the average vesicles size in absence of peptide consistent with earlier data [123, 124]. As we increased the peptide concentration, the peak upshifted and other higher size peaks appeared due to vesicles aggregation. In order to calculate the number of lipids per vesicles, we used lipid

concentration 0.2 mM, vesicles diameter 140 nm, and area per lipid  $0.554 \text{ nm}^2$  and found that  $\approx 2.137 \times 10^5$  lipid molecules are required to build a vesicle. This corresponds about 0.936 nM under our experimental conditions. If we consider the highest salt concentration of 300 mM NaCl in buffer, the number of peptide assemblies per lipid vesicle would be 2540, 360 and 63 at lowest concentration of peptide 2.38  $\mu\text{M}$ , 0.337  $\mu\text{M}$  and 0.059  $\mu\text{M}$  for monomers, tetramers and octamers respectively. At lowest concentration of NaCl, these number would be up to 7-fold greater. If 36 to 64 monomers are needed to form a fully functional pore, then we would not have all pores functional [125]. Another reason might be because of incomplete targeting of lipid vesicles as demonstrated for antimicrobial peptides earlier [61, 126, 127].

After analyzing these electrostatic effects coming from salt concentration in the buffer, we performed another different membrane binding assay in neutral membrane without negative lipid and containing 90 mol % POPC and 10 mol % cholesterol only. We observed the  $\zeta$ -potential of  $-6 \text{ mV}$  corresponding to a surface charge density of  $\sigma_o = -5.926 \text{ mC m}^{-2}$ . Although one would expect at least some non-negative value of this potential in this case (with neutral membrane and positive peptide), our small negative value might be attributed to  $\text{Cl}^-$  binding [114, 115, 116]. Moreover, the  $\zeta$ -potential almost didn't depend on peptide concentration and potential went positive at  $\geq 40 \mu\text{M}$  of peptide as shown in Fig. 4.7. This would suggest weak peptide binding to zwitterionic membrane and peptide aggregation at high concentration. The Quin-2 fluorescence and rate constants were found to be very low compared to similar system with 30 mol % POPG. The reason behind this may be that there is very little lateral mobility of peptide because of ionic and/or hydrogen-binding in presence of POPG and hence less peptide-peptide interactions. In neutral membrane, interaction of peptide with membrane is very insignificant. Similar effects have been studied earlier [125, 128] for  $\text{A}\beta_{1-40}$  and  $\text{A}\beta_{1-42}$ . This again confirms that membrane binding of  $\text{A}\beta_{25-35}$  is largely driven by electrostatics.

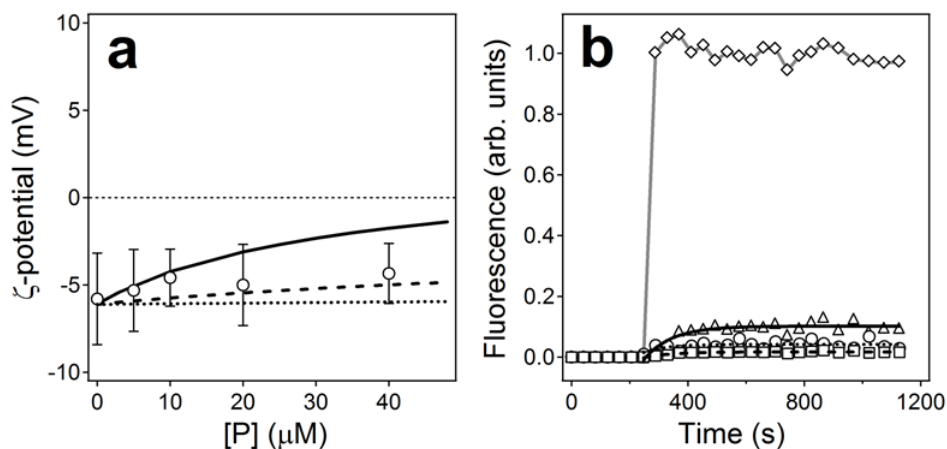


Figure 4.7:  $\zeta$ -potential of lipid vesicles as a function of added peptide concentrations with NaCl salt of 75 mM in the buffer. Solid, dashed and dotted lines represent theoretical plots for aggregation numbers of  $z = 1$ ,  $z = 4$ , and  $z = 8$  respectively (a). Quin-2 fluorescence as a function of time (b). Squares, circles and triangles represent  $P : L = 1 : 10$ ,  $1 : 5$  and  $1 : 3$  and rhombs represent effect of ionophore as positive control. The working lipid concentration is 0.2 mM with membrane molar composition of 90 % PC and 10 % cholesterol that will behave as a neutral membrane.

#### 4.1.4 Structure of Peptide in Lipid Vesicles

The CD spectroscopy has been used to assess the structure of peptide in the lipid membrane. The spectra shows that at relatively low salt concentration, the peptide assumes  $\beta$ -sheet structure (ionic strength up to 150 mM of NaCl in buffer). As the salt concentration in the buffer was increased beyond that range, the peptide didn't bind to the membrane and the structure remained the same as in aqueous buffer as shown in Fig. 4.8. This effect can be explained in terms of the increasing role of electrostatic screening with increasing salt concentration. Higher salt prevented the binding

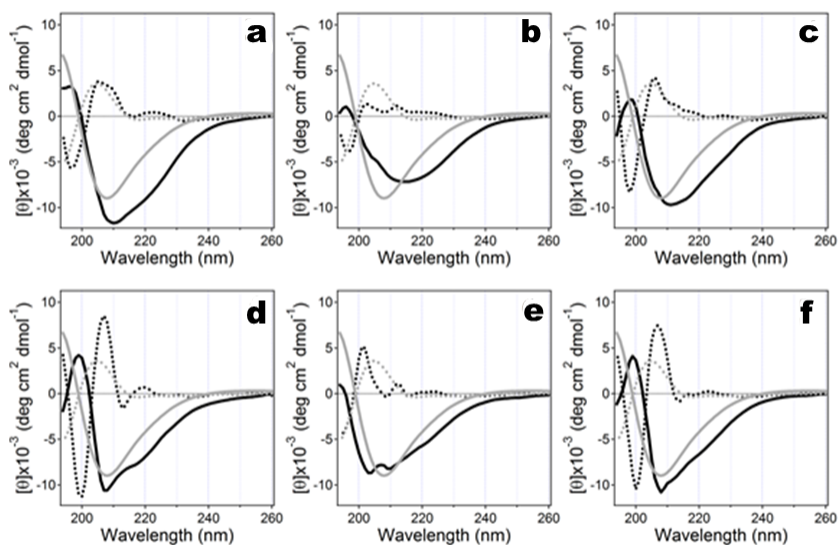


Figure 4.8: CD spectra of  $A\beta_{25-35}$  with (black solid) and without (gray solid) lipid vesicles at different ionic strength: (a) 30 mM, (b) 50 mM, (c) 75 mM, (d) 180 mM, (e) 225 mM, and (f) 300 mM of NaCl. The second derivatives are shown with respective dotted lines with (black) and without (gray) lipid vesicles. The working lipid concentration is 0.2 mM with membrane molar composition of 60 % PC, 30 % PG and 10 % cholesterol.

of peptide to the lipid vesicles. At intermediate salt 50 mM to 150 mM, rate constant of pore formation and transport of  $Ca^{2+}$  into the vesicles was the highest. This indicates that  $\beta$ -sheet conformation of peptide forms the most efficient pore.

## 4.2 Role of Cholesterol on Membrane Binding and Pore Formation by $A\beta_{25-35}$

Cholesterol is a very important part of neuronal membranes and its concentration varies with different types of cellular membranes. It plays a very distinct role in membrane–peptide interactions at different concentrations. To elucidate more on this complex behavior, we varied the concentra-

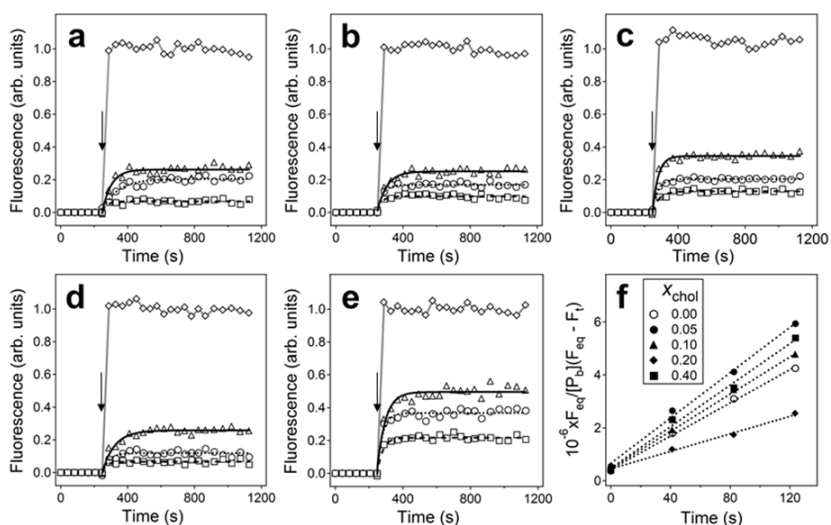


Figure 4.9: Quin–2 fluorescence as a function of time (due to influx of  $Ca^{2+}$ ) at different cholesterol concentrations: 0 % (a), 5 % (b), 10 % (c), 20 % (d), and 40 % (e). The lipid composition is  $(0.7 - x_{chol})$ , 0.3, and  $x_{chol}$  mol % of POPC, POPG and cholesterol with  $x_{chol}$  varying from 0.00, 0.05, 0.10, 0.20, and 0.40 respectively. Squares, circles and triangles represent  $P : L = 1 : 10$ , 1 : 5 and 1 : 3 and rhombs represent effect of ionophore as positive control. The working lipid concentration is 0.2 mM with buffer ionic strength of 75 mM. Graph (f) represents increase in Quin–2 fluorescence 2 min after the addition of peptide.

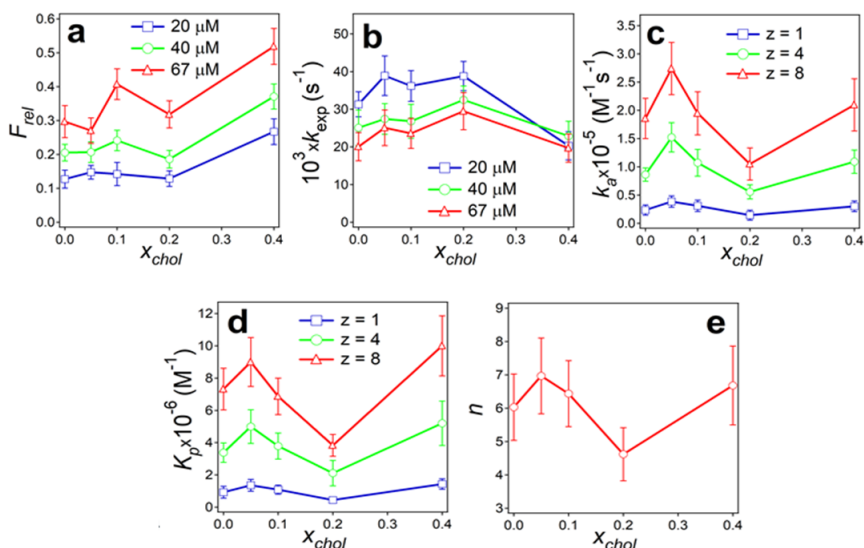


Figure 4.10: Relative Quin-2 fluorescence (a), single exponential rate constant (b), second-order rate constant of pore formation (c), affinity constant of peptide oligomers within the membrane (d), and the number of oligomers in the pore structure (e) as a function of cholesterol. The lipid composition is  $(0.7 - x_{chol})$ , 0.3, and  $x_{chol}$  mol% of POPC, POPG and cholesterol with  $x_{chol}$  varying from 0.00, 0.05, 0.10, 0.20, and 0.40 respectively. The working lipid concentration is 0.2 mM and ionic strength of buffer is 75 mM NaCl.

tion of cholesterol in the vesicles within a nearly physiological range. Quin-2 loaded vesicles with  $(0.7 - x_{chol})$  mol% of POPC, 0.3 mol% POPG and  $x_{chol}$  mol% of cholesterol with  $x_{chol}$  varying from 0, 0.05, 0.10, 0.20 and 0.40 were assayed with three different concentrations of peptide as shown in Fig. 4.9. The relative fluorescence  $F_{rel}$  was found to be directly proportional to the peptide concentration as shown in Fig. 4.10 (a) indicating polymorphic nature of  $A\beta$  which results in heterogeneous membrane bound structures [129, 130, 131]. It has been shown that the incubation of  $A\beta_{25-35}$  in buffer for about 2.5 h resulted oligomers with up to 8 monomers [101].



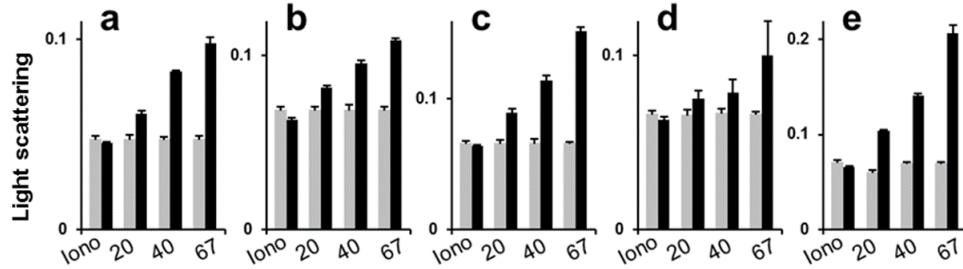


Figure 4.11: Light scattering of lipid vesicles before (gray) and after (black) addition of ionophore or peptide in  $\mu\text{M}$  as shown in the legend at various cholesterol concentrations: 0 % (a), 5 % (b), 10 % (c), 20 % (d), and 40 % (e). The lipid composition is  $(0.7 - x_{chol})$ , 0.3, and  $x_{chol}$  mol % of POPC, POPG and cholesterol with  $x_{chol}$  varying from 0.00, 0.05, 0.10, 0.20, and 0.40 respectively. The working lipid concentration is 0.2 mM and ionic strength of buffer is 75 mM NaCl.

These are the most active species in terms of membrane pore formation. When these peptide oligomers are added to the vesicles, they first bind to the membrane and then come together to form a functional pore with different number of peptide units  $n$ . The detail parameters are listed in Table B.4.

The role of cholesterol appeared to be complex as shown in Fig. 4.10. The values of  $k_a$  and  $K_p$  initially increased up to  $x_{chol} = 0.05$ , dropped around  $x_{chol} = 0.2$  and again went up at  $x_{chol} = 0.4$  as shown in Fig. 4.10 (c, d). The number of oligomers in the pore,  $n$  was found to be

in between 6 to 8 at cholesterol levels of  $x_{chol} = 0.0 - 0.1$  and  $x_{chol} = 0.4$ . The value decreased to about 5 at  $x_{chol} = 0.2$  as shown in Fig. 4.10 (e). This result indicates that pore formation is most effective by larger assemblies of peptide. This phenomena will be discussed later comparing with the membrane fluidity experimental data. Fig. 4.11 shows an increase of light scattering with addition of peptide which is directly proportional to concentration of peptide. This indicates that vesicles are intact in presence of peptide. The increase in light scattering is due to vesicles aggregation.

#### 4.2.1 Structure of Peptide by Circular Dichroism

CD spectra showed that the peptide assumed  $\beta$ -turn (type-I) structure with minimum fraction of  $\beta$ -sheet and  $\alpha$ -helix at peptide to lipid ratio of 1 : 3, for cholesterol mol % from 0.00 to 0.20 as shown in Fig. 4.12 (a, d). At  $x_{chol} = 0.4$ , the  $\alpha$ -helix component increased as shown in Fig. 4.12 (e). At lower peptide to lipid ratios of 1 : 5 and 1 : 10,  $\alpha$ -helical fraction at 220 nm decreased indicating  $\beta$ -sheet and  $\beta$ -turn structure.

The peptide structures shown by these spectra contain contribution from both membrane-bound peptide and free peptide in aqueous buffer. The structural features of CD spectra is greatly affected by the polarity of the environment. Because of poor resolution of these spectra and that the sample contained both membrane bound and free peptide, we plotted the CD spectra of only membrane bound peptide by subtracting the free peptide contribution from the total spectra as shown in Fig. 4.13. These data suggest that the membrane-bound peptide has  $\beta$ -sheet conformation that was red-shifted because of polarity of the environment [132, 133].

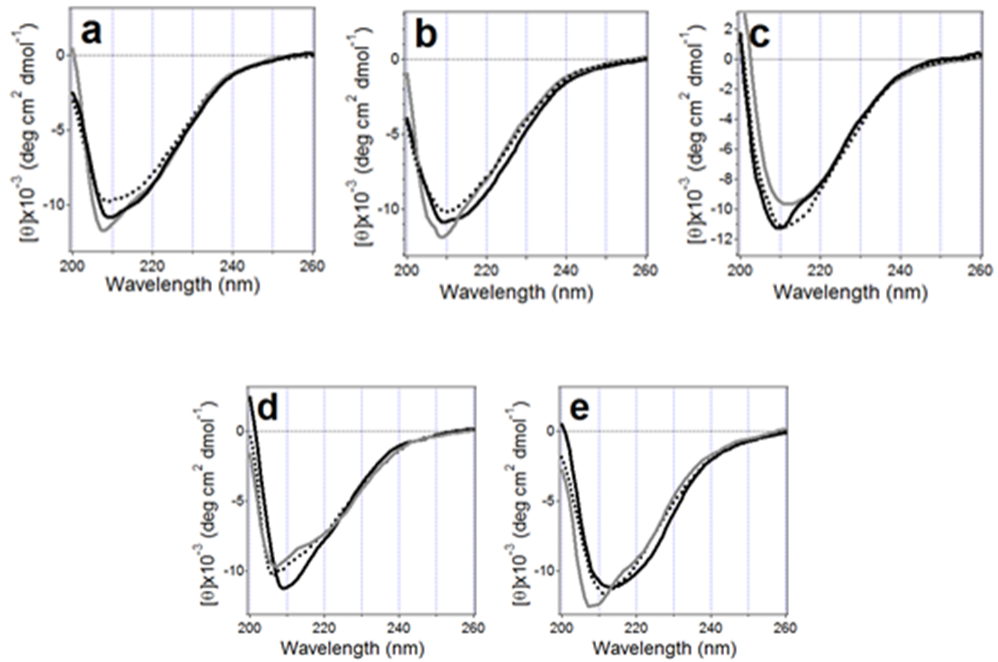


Figure 4.12: CD spectra of  $A\beta_{25-35}$  peptide at different cholesterol concentrations: 0 % (a), 5 % (b), 10 % (c), 20 % (d), and 40 % (e) in lipid vesicles with ionic strength of buffer 75 mM NaCl. The lipid composition is  $(0.7 - x_{chol})$ , 0.3, and  $x_{chol}$  mol % of POPC, POPG and cholesterol with  $x_{chol}$  varying from 0.00, 0.05, 0.10, 0.20, and 0.40 respectively. The working lipid concentration is 0.2 mM. Legend:  $P : L = 1 : 10$  (gray),  $1 : 5$  (black dotted), and  $1 : 3$  (black solid).

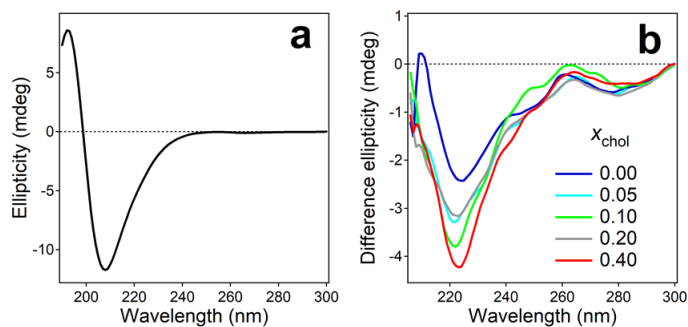


Figure 4.13: Original CD spectrum of  $A\beta_{25-35}$  peptide (a) with no lipid vesicles and (b) membrane-bound peptide at various cholesterol percentages as shown in the graph. The ionic strength of buffer is 75 mM NaCl and the working lipid concentration is 0.2 mM.

#### 4.2.2 Effect of Cholesterol on Membrane Fluidity

Generalized polarization (GP) of Laurdan was used to monitor the fluidity of lipid membrane. Without the cholesterol, Laurdan showed two emission peaks located at 435 nm and 500 nm. When the cholesterol was added to the membrane, increasing up to 0.4 mol %, the 500 nm peak gradually disappeared while the 435 nm component increased as shown in Fig. 4.14. This effect suggests that membrane becomes more and more solid [134] in presence of cholesterol. Lipid membrane was reported to transition from liquid-disordered phase ( $L_d$ ) to liquid-ordered phase ( $L_o$ ) with increasing cholesterol [135] which should inhibit the membrane insertion effect of the peptide with increasing concentration of cholesterol. Our data, however indicates more complex effect *i.e.* inter-

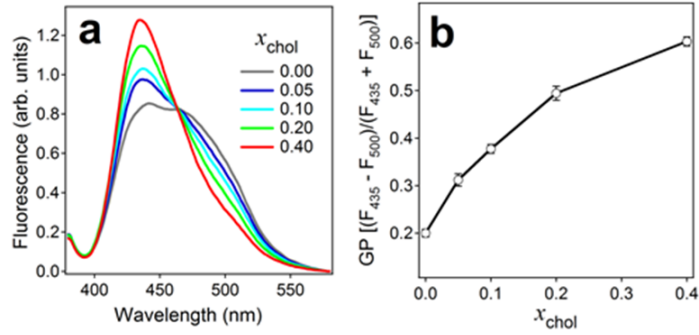


Figure 4.14: Membrane fluidity as measured by Laurdan fluorescence (a) and generalized polarization (GP) of Laurdan (b) at different cholesterol concentrations shown. The lipid composition is  $(0.7 - x_{chol})$ , 0.3, and  $x_{chol}$  mol % of POPC, POPG and cholesterol with  $x_{chol}$  varying from 0.00, 0.05, 0.10, 0.20, and 0.40 respectively.

action of cholesterol with the peptide and then modulation of membrane by the cholesterol. Cholesterol interacts with the peptide directly at low concentration *i.e.* ( $x_{chol} = 0.05$ ) [34, 36, 91, 92]. This effect enhanced the membrane pore formation as indicated by increasing values of  $k_a$  and  $K_p$ . In this case, pore structure contained 8 oligomers, as shown in Fig. 4.10 (c – e). When the cholesterol level was increased up to  $x_{chol} = 0.2$ , it caused a decrease in all three parameters. This may be explained by the fact that squeezing out of peptide assemblies occurred during membrane transition to ( $L_o$ ) phase. After this point, once the cholesterol reached ( $x_{chol} = 0.4$ ), the membrane condensing effect of cholesterol saturated which resulted in disordered boundaries between

phospholipid-rich and cholesterol-rich domains. This eventually promoted the peptide insertion and hence pore formation as indicated by an increase in  $k_a$  and  $K_p$  values as shown in Fig. 4.10 (c, d).

#### 4.2.3 Determination of Peptide Structure Using ATR-FTIR Spectroscopy

In order to examine the secondary structure components, ATR-FTIR spectra of dry lipid sample with embedded peptide were monitored. Data showed that most of the component as  $\beta$ -sheet at  $1630\text{ cm}^{-1}$  to  $1628\text{ cm}^{-1}$  with other lower intensity components at  $1660\text{ cm}^{-1}$  to  $1654\text{ cm}^{-1}$  as  $\alpha$ -helix,  $1644\text{ cm}^{-1}$  to  $1642\text{ cm}^{-1}$  as irregular (unordered),  $1700\text{ cm}^{-1}$  to  $1670\text{ cm}^{-1}$ , as  $\beta$ -turns or  $\gamma$ -turns and  $1620\text{ cm}^{-1}$  to  $1600\text{ cm}^{-1}$  are from the side chains [136]. The measurements were also repeated using  $\text{D}_2\text{O}$  vapor and  $\text{D}_2\text{O}$  buffer as shown in Fig. 4.15. Although there was a significant change in the structure between these three different conditions,  $\beta$ -sheet still remained the dominant structures. In dry state, there was about 30 % of  $\beta$ -sheet component, 30 % to 40 % of  $\beta$ -turns, 20 % of  $\alpha$ -helix, and  $\sim 10$  % of irregular structure. Increase in  $\beta$ -turns can be seen with higher cholesterol content.

As shown in Fig. 4.15 (b), after  $\text{D}_2\text{O}$  hydration, the  $\beta$ -sheet components increase and  $\beta$ -turns decrease with increasing cholesterol [136]. In  $\text{D}_2\text{O}$  buffer at 5 % and 40 % cholesterol, component of  $\beta$ -sheet jumped to 40 %, and  $\beta$ -turns decreased down to about 20 % as shown in Fig. 4.15 (c). Interestingly enough, the membrane pore formation activity is maximal at  $x_{chol} = 0.05$  and  $0.40$ . This result indicates that  $\text{A}\beta_{25-35}$  should be in  $\beta$ -sheet conformation in order to form a functional pore.

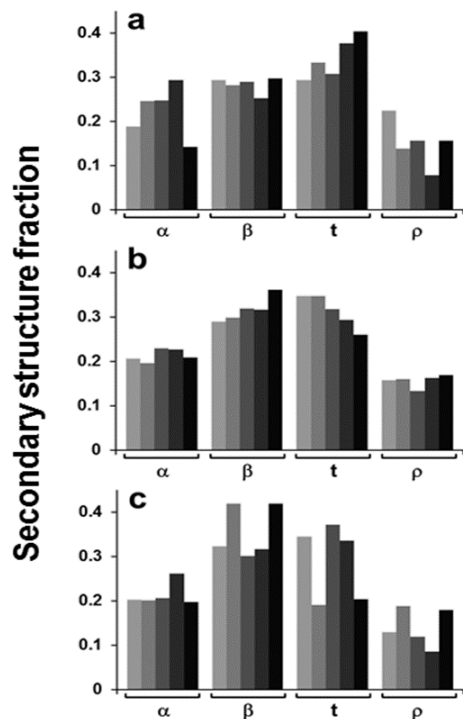


Figure 4.15: Figure shows fractions of secondary structures of  $A\beta_{25-35}$  in lipid multilayers in dry state (a),  $D_2O$  vapor (b) and  $D_2O$  buffer (c). The lipid composition is  $(0.7 - x_{chol})$ , 0.3, and  $x_{chol}$  mol % of POPC, POPG and cholesterol with  $x_{chol}$  varying from 0.00, 0.05, 0.10, 0.20, and 0.40 respectively. The symbols used are  $\alpha$  for  $\alpha$ -helix,  $\beta$  for  $\beta$ -sheet,  $t$  for turn and  $\rho$  for irregular structures.

#### 4.2.4 Peptide Orientation and Lipid Order from ATR-FTIR Spectroscopy

The ATR-FTIR method was employed to monitor the order and orientation of peptide and lipid. Data showed that most of the peptide in membrane was in  $\beta$ -sheet conformations. This tells us

that we can model the pore as  $\beta$ -barrel-like structure. The angle between the  $\beta$ -strands and the barrel axis was evaluated using the Eq. 3.29 with angle  $\gamma$  varying within some conceivable range,  $0^\circ$  to  $20^\circ$ . The possible values are shown in Table 4.4. The ATR dichroic ratio was calculated as  $R_\beta = (a_{\beta,\parallel}/a_{\beta,\perp})$ . The angle  $\beta$  varied between  $20^\circ$  to  $27^\circ$  for  $\gamma = 0^\circ$  while angle  $\beta$  got smaller with  $\gamma = 20^\circ$ . Average value of angle  $\beta$  was found to be  $\approx 22^\circ \pm 4^\circ$  [136].

Table 4.4: Orientation of  $\beta$ -Strand in Lipid Membrane in Terms of  $\beta$ -Angle Under Various Buffer Conditions

$x_{chol}$	Dry			$x_{chol}$	D <sub>2</sub> O Vapor			D <sub>2</sub> O Buffer		
	$R_\beta$	$\beta$ ( $^\circ$ )			$R_\beta$	$\beta$ ( $^\circ$ )		$R_\beta$	$\beta$ ( $^\circ$ )	
		$\gamma = 0^\circ$	$\gamma = 20^\circ$			$\gamma = 0^\circ$	$\gamma = 20^\circ$		$\gamma = 0^\circ$	$\gamma = 20^\circ$
0.00	1.464	27.2	25.3	0.00	1.120	21.2	17.2	1.233	22.1	18.5
0.05	1.165	20.1	15.6	0.05	1.010	14.6	4.6	1.066	16.9	10.3
0.10	1.328	24.5	21.8	0.10	1.163	20.2	15.7	1.160	20.1	15.6
0.20	1.303	23.9	20.9	0.20	1.577	29.3	28.0	1.243	22.4	18.9
0.40	1.247	22.5	19.1	0.40	1.194	21.1	17.0	0.890	7.1	*

The quality of lipid multilayers was tested based on the order parameter ( $S$ ) of the acyl chain. Moreover, CH<sub>2</sub> vibrational frequencies in the methylene stretching region were also analyzed. Zero value of order parameter would mean no preferential direction. Similarly, if the vibrational wave number gets shifted by  $(4 - 5) \text{ cm}^{-1}$ , this would also indicate some lipid phase transition. When there was no cholesterol, the membrane was ordered as indicated by the order parameter value of 0.5 to 0.7. Tatulian et al. reported an order parameter  $S_L$  value of 0.3 to 0.6 for PC/PG multilayers [137]. Similarly, the order parameter for extruded lipid vesicles composed of PC was reported to vary from 0.24 to 0.80 [138]. Based on these lipid order parameter data, we found that



lipid vesicles in buffer are very similar in property to that formed in supported multilayer followed by hydration using D<sub>2</sub>O buffer. The calculated ordered parameter value and CH<sub>2</sub> vibrational shift indicates a complex non-monotonous role of cholesterol *i.e.* ordered membrane at low cholesterol value and disordered membrane at high cholesterol value [136].

#### 4.2.5 Structure of the Pore

Using all above experimental constraints and standard geometry of  $\beta$ -barrels, the structure of the pore was identified. A typical sketch of a  $\beta$ -stranded barrel is shown in Fig. 4.16. The alignment of side chains of consecutive amino acids in the given  $\beta$ -strand must be in and out of the barrel alternatively. The H-bonding should be perpendicular to the side chains and strand axes [139, 140, 141, 142]. We considered the following cases:

1. Structure I: S<sup>26</sup>, K<sup>28</sup>, A<sup>30</sup>, I<sup>32</sup>, L<sup>34</sup> are inside the barrel and G<sup>25</sup>, N<sup>27</sup>, G<sup>29</sup>, I<sup>31</sup>, G<sup>33</sup>, M<sup>35</sup> are outside.
2. Structure II: S<sup>26</sup>, K<sup>28</sup>, A<sup>30</sup>, I<sup>32</sup>, L<sup>34</sup> are outside the barrel and G<sup>25</sup>, N<sup>27</sup>, G<sup>29</sup>, I<sup>31</sup>, G<sup>33</sup>, M<sup>35</sup> are inside.

Using the van der Waals volumes of amino acids [144] determined earlier, for structures I and II, the volumes required was calculated to be 3138 Å<sup>3</sup> and 2928 Å<sup>3</sup> respectively for these two topologies to accommodate the inward oriented side chains of six strands. Similarly, for an 8-stranded barrel, the required volumes were calculated to be 4184 Å<sup>3</sup> and 3904 Å<sup>3</sup> for respective configurations. The radius of barrel is written as [139]

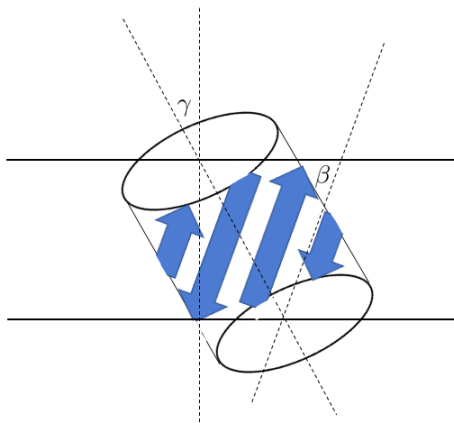


Figure 4.16: Sketch of a  $\beta$ -stranded barrel. The strands are oriented at an angle  $\beta$  with respect to the central axis of barrel and barrel axis is at angle  $\gamma$  with membrane normal.

$$R = \frac{d}{2\sin(\pi/z)\cos\beta}, \quad (4.1)$$

where  $z$  is the number of strands in the barrel, and  $\beta$  is the strand angle relative to the cylindrical axis and  $d$  is the interstrand distance as shown in Fig. 4.17 (b).

We can use the following formula to find the internal volume of  $\beta$ -barrel:

$$V = \pi R^2 h_b, \quad (4.2)$$

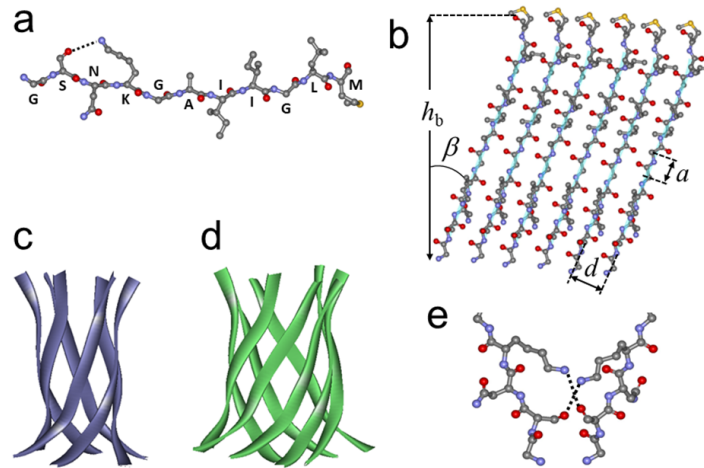


Figure 4.17: (a) Cartoon structure of  $A\beta_{25-35}$  with hydrogen bonding between  $S^{26}$  and  $K^{28}$  as shown by the dotted line. Color code is as follow: carbon in gray, nitrogen in blue, oxygen in red, and sulfur in yellow. Hydrogen atoms are not shown for clarity. (b) Model of 6-stranded  $\beta$ -barrel of the peptide in unwrapped form (inside barrel view). (c) Cartoon for a 6-stranded  $\beta$ -barrel (d) Cartoon for a 8-stranded  $\beta$ -barrel of  $A\beta_{25-35}$  (ribbon format), using residues (90 – 100) of  $\alpha B$  crystallin (reference: PDB code 3sgn). This forms “cylindrin” structure consisting of 6-stranded  $\beta$ -barrel [143]. (e) Proposed pore stabilizing H-bonding between  $S^{26}$  and  $K^{28}$  of one strand with  $K^{28}$  and  $S^{26}$  of adjacent strand in  $\beta$ -barrel.

where  $h_b$  is the barrel height given by

$$h_b = m \cos \beta, \quad (4.3)$$

and  $m$  being number of amino acids in the strand.

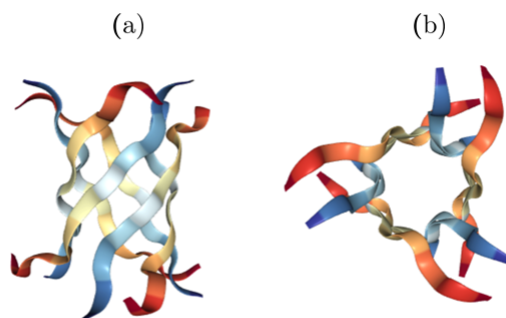


Figure 4.18: Side view (a) and top view (along the pore axis) (b) of  $\alpha$ B crystallin residues (90 – 100) (reference: PDB code 3sgn).

For standard barrels,  $d = 4.7 \text{ \AA}$ , and inter residue distance is  $a = 3.48 \text{ \AA}$ . For  $A\beta_{25-35}$ ,  $m = 11$  and  $\beta = 22^\circ$ , for 6- and 8-stranded barrels, we obtained  $R_6 = 5.09 \text{ \AA}$ ,  $V_6 = 2890 \text{ \AA}^3$ ,  $R_8 = 6.65 \text{ \AA}$ , and  $V_8 = 4930 \text{ \AA}^3$ . Both structures are possible as shown in Fig. 4.17 (c, d). Moreover, 6-stranded  $\beta$ -barrel are tightly packed and 8-stranded structures with internal cavity of  $750 \text{ \AA}^3$  to  $1000 \text{ \AA}^3$  will have a radius of  $2.6 \text{ \AA}$  to  $3.0 \text{ \AA}$ . The free volume might be randomly distributed without a fixed passageway. Hence, the  $\text{Ca}^{2+}$  transporting pores/channels are the supra-molecular structures composed of five to eight 6-stranded barrels. On the other hand, single barrel-like 8-stranded pores are possible, but they may not be able to conduct ions effectively. Here are the other possibilities:

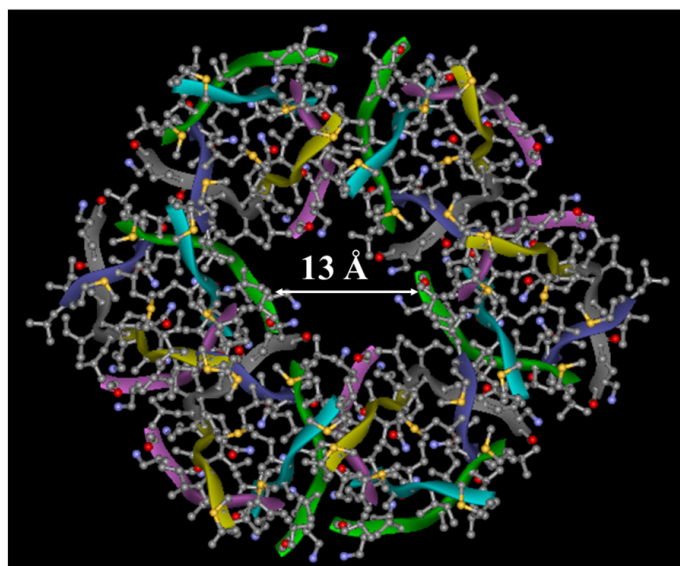


Figure 4.19: Top view (along the pore axis) of the final membrane pore (radius of central cavity about 6.5 Å) formed by  $A\beta_{25-35}$  as hexamer of 6-stranded barrel constructed from  $\alpha$ B crystallin (90 – 100) (reference: PDB code 3sgn), replacing the side chains by  $A\beta_{25-35}$  side chains. Each barrel is turned about its cylindrical axes by  $60^\circ$  relative to its neighbors.

Using  $R_6 = 5.09 \text{ \AA}$ ,  $a = 2.0 \text{ \AA}$ , (thickness of side chains), a hexamer of 6-stranded barrel would provide a pore of radius 6 Å to 7 Å, as shown in Fig. 4.19. The structure was sketched using  $\alpha$ B crystallin (90 – 100) (reference: PDB code 3sgn), replacing the side chains by  $A\beta_{25-35}$  side chains. It forms 6-stranded  $\beta$ -barrel structure as shown in Fig. 4.18. The first configuration may involve hydrogen bonding interaction between N–N and some hydrophobic interactions between I–I. Similarly, the second topology will be accompanied by K–S hydrogen bonding between two inter-strands and I–L hydrophobic interactions. The interplay of these interactions will stabilize the supramolecular pore. Because of interstrand staggering, the terminal carbonyl oxygens are not

involved in hydrogen bonding that helps the pores acquire cation selectivity. The ions are most likely in hydrated forms during the transport as the energy required for  $\text{Ca}^{2+}$  dehydration is greater than  $41.84 \text{ kJ M}^{-1}$ .

### 4.3 Detection of Early Stage Aggregation of $\text{A}\beta_{1-42}$ Using FRET

Although there have been a lot of research work in the field of protein fluorescence, not much work has been done in the field of phenylalanine to tyrosine resonance energy transfer even 30 year after the phenomena was observed in a histonelike protein from *Thermoplasma acidophilum* [145]. The problem was likely in detecting the very small intensity of phenylalanine emission. The aim of this work is to monitor the entire process of aggregation including oligomer formation and fibrillogenesis including identification of the segments of  $\text{A}\beta$  that initiate such processes using intrinsic FRET. Amyloid fibril formation by proteins is usually studied by fluorescence techniques, using exogenous fluorophores such as thioflavin T (ThT). The presence of such agents in the protein sample has two potential pitfalls: (a) the probe may affect fiber formation by intercalating in the fibrillary structure, and (b) such probes detect only the later stages of aggregation, *i.e.*, fibrillogenesis, and are insensitive to formation of soluble oligomers, the most cytotoxic species. Along with FRET experiments, ThT fluorescence was measured in parallel, which indicated temporal dissection of oligomerization, the onset and progression of fibrillogenesis. Thus, the entire process of peptide aggregation, including oligomer and fibril formation, could be monitored. CD measurements were conducted on same samples, elucidating structural changes in the peptides during aggregation. Thus, F-to-Y FRET, combined with ThT fluorescence and structural techniques, illuminates the full range of molecular events during oligomerization and fibrillization of amyloid peptides and provides valuable insight in the mechanism of their cytotoxic effects.

### 4.3.1 FRET For Soluble Oligomer Detection

In this section, I will describe the results obtained from Forster Resonance Energy Transfer (FRET) using different segments of  $A\beta_{1-42}$ . We purchased different segments of  $A\beta_{1-42}$  depending on the position of phenylalanine (F) and tyrosine (Y) and also based on types of residues present as shown in Table 4.20. The fluorescent amino acid F is colored blue and tyrosine Y is colored red. The purpose of this work is to detect oligomers of  $A\beta_{1-42}$  or figure out the early stage aggregation pattern and its origin how it starts out without using any external probe. For this, we first optimized the excitation wavelengths for both phenylalanine and tyrosine to make sure excitation of phenylalanine doesn't excite tyrosine. The phenylalanine can be excited at two excitation wavelengths  $\approx 220$  nm and 265 nm. The optimized wavelength were 220 nm for phenylalanine and 278 nm for tyrosine. Any residual intrinsic tyrosine emission was subtracted during data processing.

The peptides were dissolved in hexafluoroisopropanol (HFIP), dried by desiccation, and suspended in aqueous buffer of 25 mM NaCl, 20  $\mu$ M thioflavin-T (ThT), and 25 mM Na,K-phosphate buffer (pH 7.2). We have used several possible combinations of different sections of peptide for this study. As the phenylalanine (F) and tyrosine (Y) are in peptide segments  $A\beta_{1-10}$ ,  $A\beta_{6-15}$ ,  $A\beta_{11-20}$ ,  $A\beta_{16-25}$ ,  $A\beta_{11-28}$  and  $A\beta_{28-41}$ , we focused our work mainly in that direction. The FRET can occur when fluorescent residues called donor and acceptors are within a certain distance called Forster distance. If the residues are that close, then excitation of phenylalanine (F) gives an emission spectra which overlaps with the absorption spectra of tyrosine (Y). The emission energy then transfers to tyrosine and excites tyrosine. In this event, there will be decrease in donor fluorescence and increase in acceptor emission. This will require proper orientation of F and Y and within a given distance. The several possible combinations are as shown in Fig. 4.21. The blue stretch denotes phenylalanine segment and red denotes tyrosine segment.

Symbols Used	A $\beta$ Segments	Sequence
Pep 1	A $\beta_{1-10}$	DAE <b>F</b> RHDSG <b>Y</b>
Pep 2	A $\beta_{6-15}$	HDSG <b>Y</b> EVHHQ
Pep 3	A $\beta_{11-20}$	EVHHQKL <b>VFF</b>
Pep 4	A $\beta_{16-25}$	KL <b>VFF</b> AEDVG
Pep 5	A $\beta_{21-30}$	AEDVGSNKGA
Pep 6	A $\beta_{26-36}$	SNKGAIIGLMV
Pep 7	A $\beta_{31-42}$	IIGLMVGGVVIA
Pep 8	A $\beta_{11-28}$	EVHHQKL <b>VFF</b> AEDVGSNK
Pep 9	A $\beta_{28-11}$	KNSGVDEA <b>FF</b> VLKQHHVE

Figure 4.20: Different segments of peptide A $\beta_{1-42}$  fragments that have been studied. Phenylalanine (F) and tyrosine (Y) residues are highlighted yellow and red, respectively.

Oligomer formation was monitored by measuring fluorescence resonance energy transfer (FRET) between phenylalanine (F) and tyrosine (Y). As shown in Table 4.20, peptide 1 has both F and Y, so its aggregation in a certain alignment could produce FRET. Formation of A $\beta_{1-10}$ /A $\beta_{11-20}$  or A $\beta_{6-15}$ /A $\beta_{16-25}$  hetero-oligomers in a parallel, in-register alignment would produce FRET as well. Phenylalanine was excited at a wavelength where tyrosine is not excited, and consecutive fluorescence spectra were recorded to monitor time-dependent changes in F and Y emissions around 280 nm and 310 nm, respectively. The optimal excitation wavelength was found to be 220 nm. The spectra of peptides 1 and 3 (100  $\mu$ M) measured individually were subtracted from the the spectrum of the the mixture of these two peptides (50  $\mu$ M each) at same time point, multiplied by 2 (to make correction for concentration). These difference fluorescence spectra were obtained for A $\beta_{1-10}$ /A $\beta_{11-20}$  and A $\beta_{6-15}$ /A $\beta_{16-25}$  peptide systems over 200 h, and F to Y FRET during



hetero-oligomer formation was manifested by a reduction of F emission intensity around 280 nm paralleled with enhancement of Y intensity around 310 nm. The plots of difference F and Y fluorescence intensities against time reflected the kinetics of aggregation.

Homo-oligomers of  $A\beta_{1-10}$  under certain alignment and  $A\beta_{1-10}/A\beta_{11-20}$  or  $A\beta_{6-15}/A\beta_{16-25}$  hetero-oligomers in a parallel, in register alignment can produce FRET. In case of the  $A\beta_{1-10}/A\beta_{11-20}$  system, strong FRET effect developed between 0 h to 10 h of incubation of the two peptides, which sustained for around 40 h and diminished by 50 h of incubation. In case of the  $A\beta_{6-15}/A\beta_{16-25}$  system, FRET appeared upon mixing the two peptides, albeit at a lower intensity, and sustained for the entire period of incubation. These data imply that peptides 1 and 3 gradually form parallel, in-register aggregates, which disperse by 50 h time point, where the peptide start forming fibrils, which evidently have a different structure. Conversely, peptides 2 and 4 form parallel or antiparallel aggregates; these structures cannot be distinguished based on the present data. Also, it is not clear if the transition from oligomers to fibrils involves structural changes for the latter system. ThT data show dissection of ThT-oligomers into monomers but no early stage fibers formation. Using FTIR and FRET for other sections of peptide, we plan to bring early-stage oligomerization pathways at molecular level.

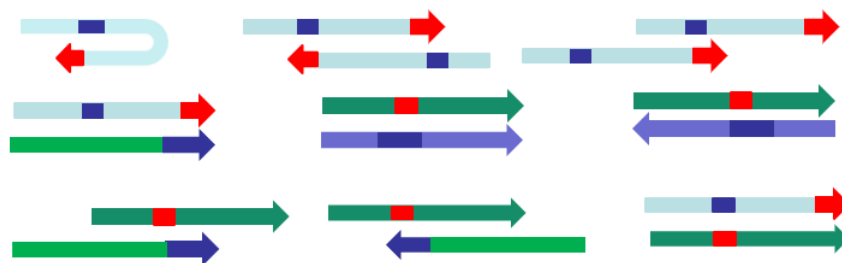


Figure 4.21: Several possible arrangements of different segments of peptide  $A\beta_{1-42}$ .

Because F has very weak emission intensity, and Y has much bigger intensity, it may not be easy to see FRET transfer just by looking into peaks. Hence, to effectively monitor FRET, we used a spectral subtraction method called “Difference Spectrum” defined as

$$DS = 2F_{xy}^{220} - (F_x^{220} + F_y^{220})$$

As we see from the Table 4.20, the most expected FRET pair would be a mixture of peptide 1 and peptide 3 and also another mixture of peptide 2 and peptide 4. Hence we started with these

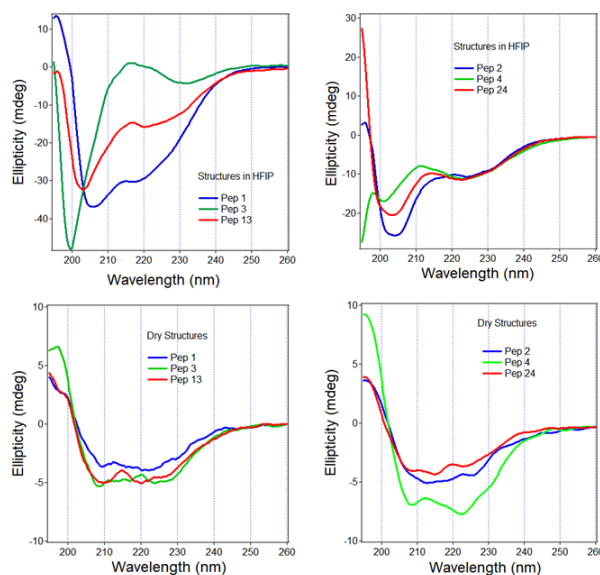


Figure 4.22: Structures of peptides  $A\beta_{1-10}$ ,  $A\beta_{11-20}$  and their equimolar mixture in HFIP and dry states (left panels). Right panels show similar structures of peptides  $A\beta_{6-15}$ ,  $A\beta_{16-25}$  and their equimolar mixture in HFIP and dry states respectively using CD.

mixtures. The structures of these peptides, individually and in equimolar mixture in dry states and in HFIP are shown in Fig. 4.22. The structures are in helical conformation except for peptide 2, 4 and their mixture where turn structure is dominant. Now, we measured the FRET occurring between peptides 1 and 3 in their equimolar mixture and that of the mixture of 2 and 4 are as shown in Fig. 4.23. Similarly, for the structural information of these peptide segments and their combination, CD measurements were also done at the same time as shown in Fig. 4.24.

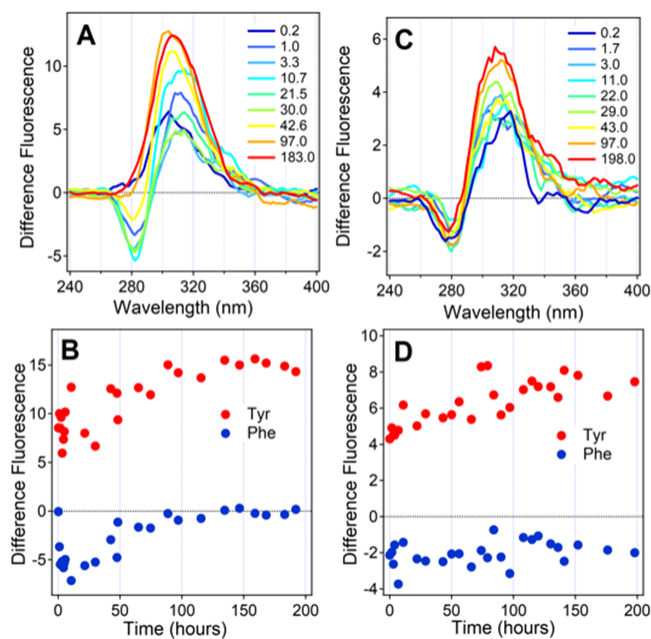


Figure 4.23: FRET difference spectra and time dependence of difference F and Y fluorescence intensities for  $A\beta_{1-10}/A\beta_{11-20}$  (A,B) and  $A\beta_{6-15}/A\beta_{16-25}$  (C,D). In panels A and C, the insets show the hours of incubation in buffer (25 mM NaCl, 20  $\mu$ M ThT, 25 mM Na,K-phosphate, pH 7.2) at 25  $^{\circ}$ C.

### 4.3.2 Secondary Structure Change During Oligomerization Using CD

The peptides' secondary structural changes during aggregation were studied by circular dichroism (CD) spectroscopy. CD spectra of peptide 1 show a prominent minimum around 200 nm to 205 nm, indicating mostly unordered structure. The spectra of peptide 3 adopt a different shape, dominated by a minimum around 225 nm and a maximum around 200 nm, possibly indicating  $\beta$ -turn structure. The mixture of peptide 1 and 3 produces CD spectra that include the features of the spectra of individual peptides. The structural features of peptides 2 and 4, and their mixture are different.

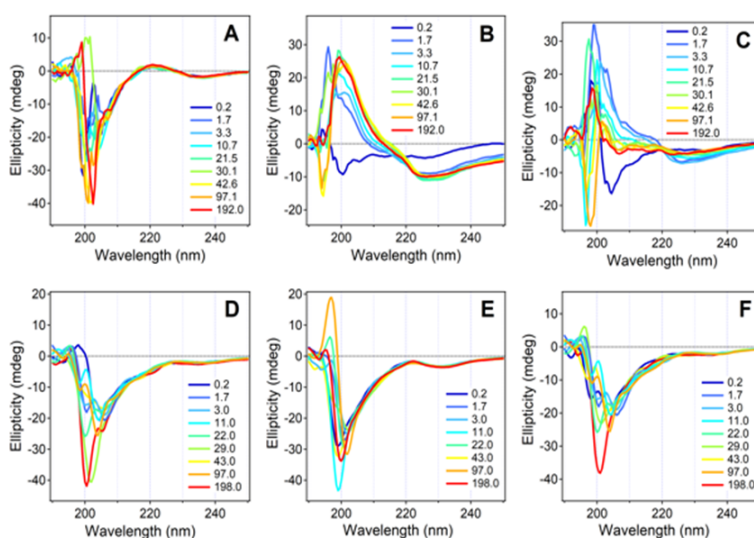


Figure 4.24: CD spectra of  $A\beta_{1-10}$  (A),  $A\beta_{11-20}$  (B), equimolar mixture of  $A\beta_{1-10}$  and  $A\beta_{11-20}$  (C),  $A\beta_{6-15}$  (D),  $A\beta_{16-25}$  (E), and the equimolar mixture of  $A\beta_{6-15}$  and  $A\beta_{16-25}$  (F) at various time periods of incubation in aqueous buffer containing 25 mM NaCl, 20  $\mu$ M ThT, 25 mM Na,K-phosphate, pH 7.2 at temperature 25  $^{\circ}$ C.

These peptides tend to stay in unordered conformation during the entire 200 h time period of incubation in aqueous buffer.

#### 4.4 FTIR and ssNMR Analysis of Neurotoxic Peptides $A\beta_{1-42}$ and $pEA\beta_{3-42}$ in Membrane

In order to monitor the structure of these neurotoxic peptides in lipid membrane, we analyzed FTIR and ssNMR data in unlabeled and corresponding labeled peptides. We used different peptides  $A\beta_{1-42}$  and  $pEA\beta_{3-42}$  with  $^{13}\text{C}$ ,  $^{15}\text{N}$ —segmentally labeled at  $^{16}\text{K}^{17}\text{L}^{18}\text{V}$  and  $^{36}\text{V}^{37}\text{G}^{38}\text{G}^{39}\text{V}$  as indicated by red color. Similarly,  $^{13}\text{C}$ ,  $^{15}\text{N}$ —uniformly labeled  $A\beta_{1-42}$  was also used as shown below.

$A\beta_{1-42}$ :

$^1\text{DAEFRHDSGYEVHHQ}^{16}\text{K}^{17}\text{L}^{18}\text{VFFAEDVGSNKGAIIGLMVGGVVI}^{42}\text{A}$

$^1\text{DAEFRHDSGYEVHHQKLVFFAEDVGSNKGAIIGLM}^{36}\text{V}^{37}\text{G}^{38}\text{G}^{39}\text{VVI}^{42}\text{A}$

$pEA\beta_{3-42}$ :

$p^3\text{EFRHDSGYEVHHQ}^{16}\text{K}^{17}\text{L}^{18}\text{VFFAEDVGSNKGAIIGLMVGGVVI}^{42}\text{A}$

$p^3\text{EFRHDSGYEVHHQKLVFFAEDVGSNKGAIIGLM}^{36}\text{V}^{37}\text{G}^{38}\text{G}^{39}\text{VVI}^{42}\text{A}$

$A\beta_{1-42}$ :

$^1\text{DAEFRHDSGYEVHHQKLVFFAEDVGSNKGAIIGLMVGGVVI}^{42}\text{A}$

##### 4.4.1 FTIR Shows Different Aggregation Pathways of $A\beta_{1-42}$ and $pEA\beta_{3-42}$

The sample preparation steps for membrane—peptide reconstitution were as described in materials and methods section. The peptide was reconstituted in lipid membrane in 10 mM Na,K—phosphate

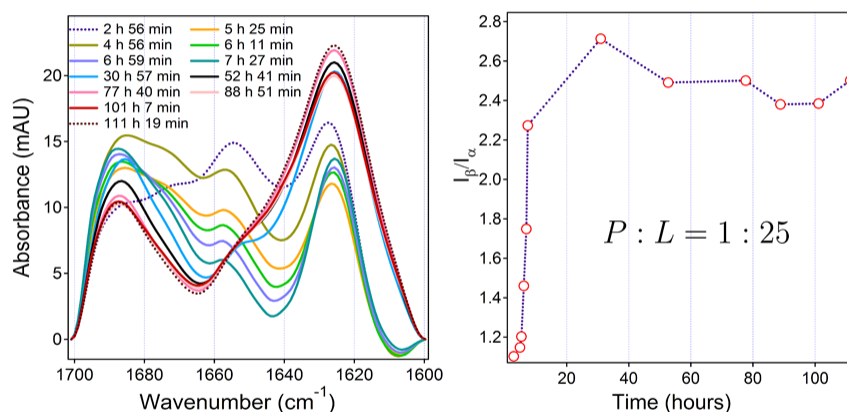


Figure 4.25: FTIR spectra of A $\beta_{1-42}$  in lipid membrane and corresponding time dependence of the values of  $I_{\beta}/I_{\alpha}$  in 10 mM Na,K-phosphate with pD 7.2, in peptide to lipid ratio of  $P : L = 1 : 50$ . Lipid composition is 60 % POPC, 30 % POPG and 10 % cholesterol.

buffer with pD 7.2, in peptide to lipid ratio of 1 : 50. Lipid composition was 60 % POPC, 30 % POPG and 10 % cholesterol. FTIR analysis revealed that A $\beta_{1-42}$  and pEA $\beta_{3-42}$  in membrane stabilized in  $\beta$ -sheet conformation through different aggregation pathways. The A $\beta_{1-42}$  and pEA $\beta_{3-42}$  peptides in lipid membrane followed distinct conformational pathways. A $\beta_{1-42}$  initially assumed partial  $\alpha$ -helix (1655 cm $^{-1}$ ) and  $\beta$ -sheet (1625 cm $^{-1}$ ) structures in lipid environment. The helix component gradually decreased while the beta sheet components increased over time. After about 7 h, the structure stabilized in mostly two components: intermolecular  $\beta$ -sheets at about

1625  $\text{cm}^{-1}$  and  $\gamma$ -turns or unordered structure at about 1687  $\text{cm}^{-1}$  as shown in Fig. 4.25. This agrees well with the NMR data which showed unordered structures in the region  $^{16}\text{K}^{17}\text{L}^{18}\text{V}$  and intermolecular  $\beta$ -sheets in the region  $^{36}\text{V}^{37}\text{G}^{38}\text{G}^{39}\text{V}$ . The ratio of  $\beta$ -sheet to  $\alpha$ -helix increased gradually up to 7 h to 8 h and then saturated afterwards. The values of  $I_{\beta}/I_{\alpha}$  are summarized in Appendix Table C.1.

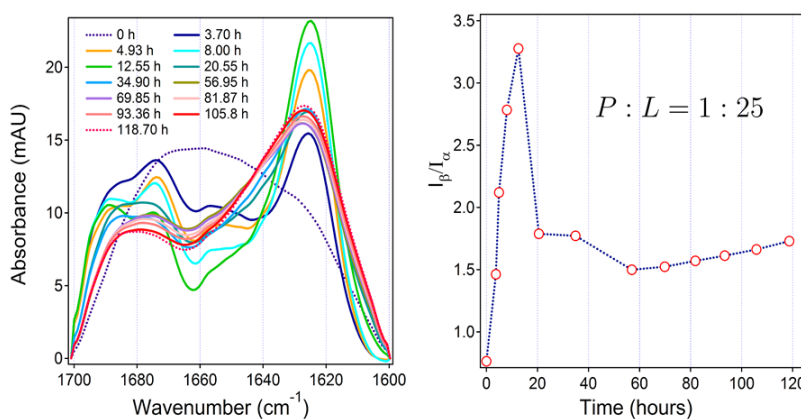


Figure 4.26: FTIR spectra of pEA $_{\beta 3-42}$  in lipid membrane and corresponding time dependence of the values of  $I_{\beta}/I_{\alpha}$  in 10 mM Na,K-phosphate with pD 7.2, in peptide to lipid ratio of  $P : L = 1 : 50$ . Lipid composition is 60 % POPC, 30 % POPG and 10 % cholesterol.

The pEA $_{\beta 3-42}$  peptide on the other hand shows unordered structure for the first few hours and then it acquires two major components; intermolecular  $\beta$ -sheets (1625  $\text{cm}^{-1}$ ) and  $\beta/\gamma$ -turns or unordered structures (1675  $\text{cm}^{-1}$ ) with small  $\alpha$ -helix component (1656  $\text{cm}^{-1}$ ) as shown in Fig. 4.26. The ratio  $I_{\beta}/I_{\alpha}$  gradually increased for about 15 h and then dropped to reach a plateau. The

structure then assumed a stable conformation with turn structures ( $1684\text{ cm}^{-1}$ ) and intermolecular  $\beta$ -sheets ( $1625\text{ cm}^{-1}$ ). The values of  $I_{\beta}/I_{\alpha}$  are summarized in Table C.2 in Appendix.

#### 4.4.2 Solid State NMR Data Shows Coexisting Ordered ( $\beta$ -Sheet) and Disordered (Turns and Loops) Regions in Both Peptides $A\beta_{1-42}$ and $pEA\beta_{3-42}$ in Lipid Membrane.

For the ssNMR characterization of peptides  $A\beta_{1-42}$  and  $pEA\beta_{3-42}$  in lipid membrane, previously described peptide reconstitution methods (Materials and Methods) were used. The peptide reconstitution was done in peptide to lipid ratio of  $P : L = 1 : 25$  in 10 mM Na,K-phosphate buffer

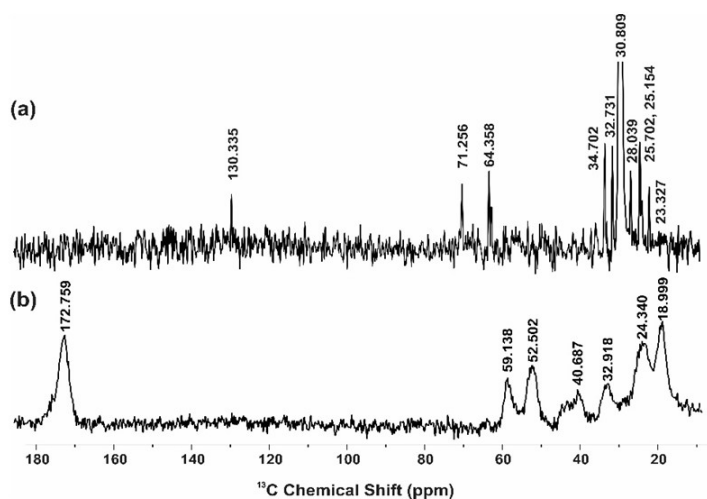


Figure 4.27: 1D CP  $^{13}\text{C}$ -NMR spectra of (a) pure lipid sample with 60 % POPC, 30 % POPG and 10 % cholesterol (b) pure peptide  $A\beta_{1-42}$  with  $^{13}\text{C}$ ,  $^{15}\text{N}$ -segmentally labeled at  $^{16}\text{K}^{17}\text{L}^{18}\text{V}$ .

with pD 7.2. Lipid membrane composition was 60 % POPC, 30 % POPG and 10 % cholesterol.



As a baseline characterization, we first acquired cross polarization (CP) spectra of pure lipid and pure peptide samples by themselves as shown in Fig. 4.27. Typical sharp and strong resonances were observed with pure lipid sample in the CP spectrum, indicating a high uniformity in our lipid preparation. In contrast, both pure  $A\beta_{1-42}$  and  $pEA\beta_{3-42}$  with  $^{13}\text{C}$ ,  $^{15}\text{N}$ –segmentally labeled at  $^{16}\text{K}^{17}\text{L}^{18}\text{V}$  exhibited broad NMR linewidth (3 ppm to 4 ppm) as shown in Fig. 4.27 indicating highly inhomogeneous and polymorphic conformation. Similar broad resonances were observed with  $A\beta_{1-42}$  and  $pEA\beta_{3-42}$  peptides  $^{13}\text{C}$ ,  $^{15}\text{N}$ –segmentally labeled at  $^{36}\text{V}^{37}\text{G}^{38}\text{G}^{39}\text{V}$ . This highly heterogeneous conformation of  $A\beta$  agrees with Wei Qiang et al. [146].

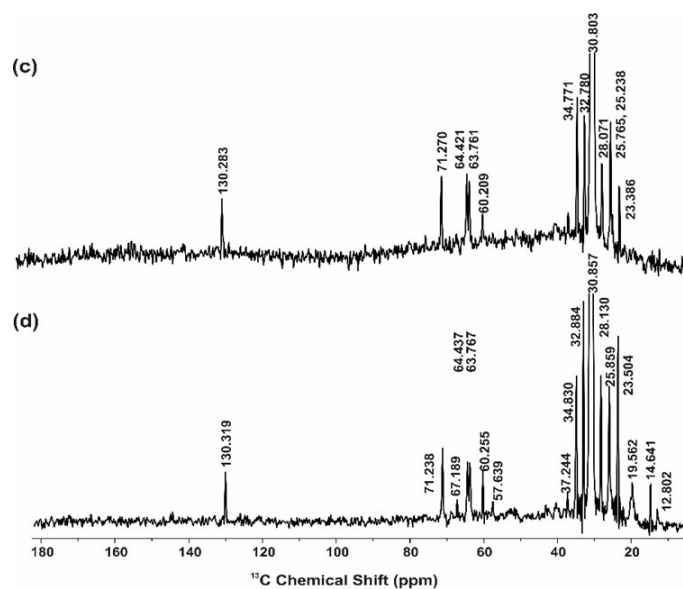


Figure 4.28: 1D CP  $^{13}\text{C}$ –NMR spectra of peptide (c)  $A\beta_{1-42}$  and (d)  $pEA\beta_{3-42}$  reconstituted in lipid membrane. Peptides are  $^{13}\text{C}$ ,  $^{15}\text{N}$ –segmentally labeled at  $^{16}\text{K}^{17}\text{L}^{18}\text{V}$ .

In contrast, when reconstituted in lipid membrane, little peptide signals were observed in 1D CP  $^{13}\text{C}$ –NMR spectra for both  $A\beta_{1-42}$  and  $pEA\beta_{3-42}$ –segmentally labeled at residues  $^{16}\text{K}^{17}\text{L}^{18}\text{V}$  as

shown in Fig. 4.28. It suggests that  $^{16}\text{K}^{17}\text{L}^{18}\text{V}$  region in both peptide samples reconstituted in lipids is disordered, likely in looped region. This agrees with the existing models by Y. Ishii and R. Tycko [48, 147].

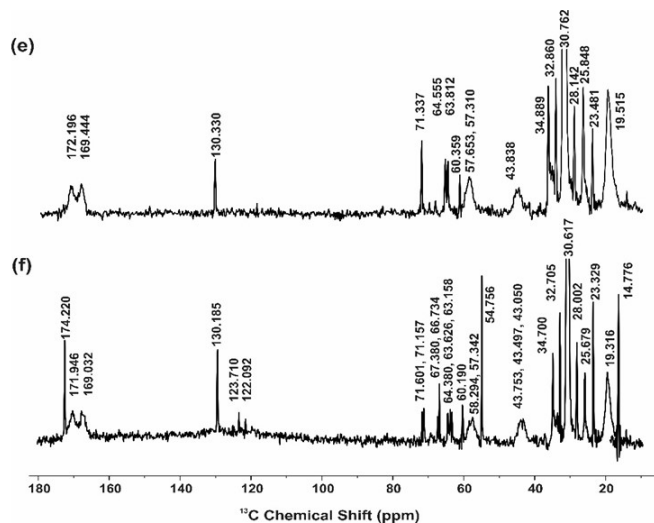


Figure 4.29: 1D  $^{13}\text{C}$ -NMR spectra of the peptide  $\text{A}\beta_{1-42}$  with  $^{13}\text{C}$ ,  $^{15}\text{N}$ -segmentally labeled at  $^{36}\text{V}^{37}\text{G}^{38}\text{G}^{39}\text{V}$  (e) CP and (f) direct  $\pi/2$  pulse (*Onepul*) in lipid membrane.

Meanwhile, we observed the downshift of  $\text{C}_\alpha$  and  $\text{C}_\beta$  peaks for both peptides  $^{13}\text{C}$ ,  $^{15}\text{N}$ -segmentally labeled at  $^{36}\text{V}^{37}\text{G}^{38}\text{G}^{39}\text{V}$  in their 1D CP  $^{13}\text{C}$ -NMR spectra (which selectively observes rigid signals) and direct  $\pi/2$  pulse (which can show both rigid and dynamic segments) acquisition spectra as shown in Fig. 4.29 and Fig. 4.30 respectively. This represents  $\beta$ -sheet conformation in that region. In addition, the linewidth reduced to 1 ppm or less. It suggests that this region assumes uniform conformation after reconstitution in lipid membrane. We also observed the membrane conformational uniformity preserved before and after peptide reconstitution as shown by the simi-

lar line width of lipid components before and after lipid–peptide reconstitution.

Figures 4.29 and 4.30 represent how CP excites selectively only rigid segments and the direct  $\pi/2$  pulse excites all rigid and dynamic segments. The missing lipid components in 1D CP  $^{13}\text{C}$ –NMR spectra compared to that in direct  $\pi/2$  pulse (*Onepul*) acquisition spectra shows that some lipid segments, specifically glycerol region (around 60 ppm to 67 ppm) becomes flexible after peptide reconstitution. This may suggest some preferential interaction of peptide in that region. The chemical shift values and line widths are summarized in Tables C.3 and C.4 in the Appendix.

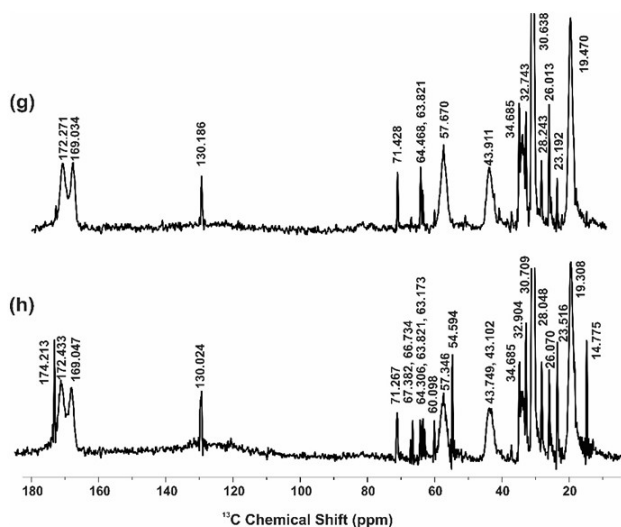


Figure 4.30: 1D  $^{13}\text{C}$ –NMR spectra of the peptide  $\text{pEA}\beta_{3-42}$  with  $^{13}\text{C}$ ,  $^{15}\text{N}$ –segmentally labeled at  $^{36}\text{V}^{37}\text{G}^{38}\text{G}^{39}\text{V}$  (*g*) CP and (*h*) direct  $\pi/2$  pulse (*Onepul*) in lipid membrane.

After these initial characterization, we performed 2D  $^{13}\text{C}$ – $^{13}\text{C}$  DARR spectrum of the peptide  $\text{pEA}\beta_{3-42}$   $^{13}\text{C}$ ,  $^{15}\text{N}$ –segmentally labeled at  $^{36}\text{V}^{37}\text{G}^{38}\text{G}^{39}\text{V}$  recorded at 600 MHz resonance with

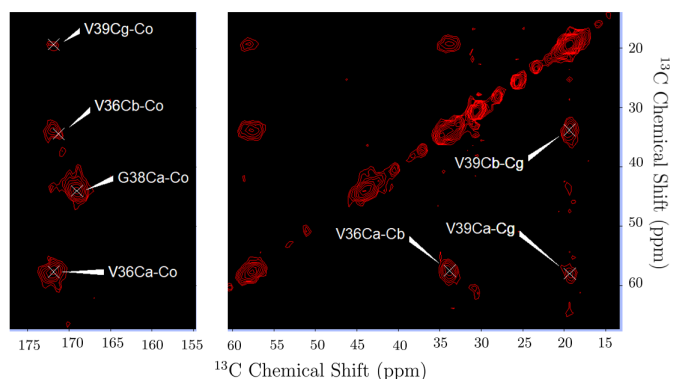


Figure 4.31: 2D  $^{13}\text{C}$ – $^{13}\text{C}$  DARR spectrum of the peptide pEA $\beta_{3-42}$   $^{13}\text{C}$ ,  $^{15}\text{N}$ –segmentally labeled at  $^{36}\text{V}^{37}\text{G}^{38}\text{G}^{39}\text{V}$  recorded at 600 MHz resonance with 100 ms mixing time in lipid membrane.

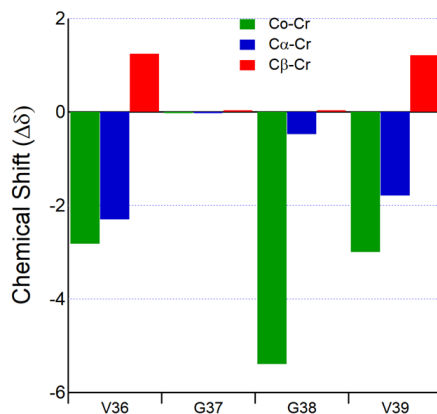


Figure 4.32: Chemical shift of  $\text{C}_o$ ,  $\text{C}_\alpha$ , and  $\text{C}_\beta$  of different residues with respect to random coil  $\text{C}_r$  in 2D  $^{13}\text{C}$ – $^{13}\text{C}$  DARR spectrum of the peptide pEA $\beta_{3-42}$   $^{13}\text{C}$ ,  $^{15}\text{N}$ –segmentally labeled at  $^{36}\text{V}^{37}\text{G}^{38}\text{G}^{39}\text{V}$  recorded at 600 MHz resonance with mixing time 100 ms in lipid membrane.

100 ms mixing time in lipid membrane as shown in Fig. 4.31. Based on the chemical shift values of  $C_o$ ,  $C_\alpha$ , and  $C_\beta$  with respect to the random coil  $C_r$ , we again confirmed the down-shift of  $C_o$  and  $C_\alpha$  and up-shift of  $C_\beta$  as shown in Fig. 4.32. This indicates  $^{36}\text{V}^{37}\text{G}^{38}\text{G}^{39}\text{V}$  region of  $\text{pEA}_{\beta_{3-42}}$  assumes  $\beta$ -sheet conformation. The shift were calculated based on the random coil  $^{13}\text{C}$  chemical shift values summarized in Table C.6 in the Appendix.

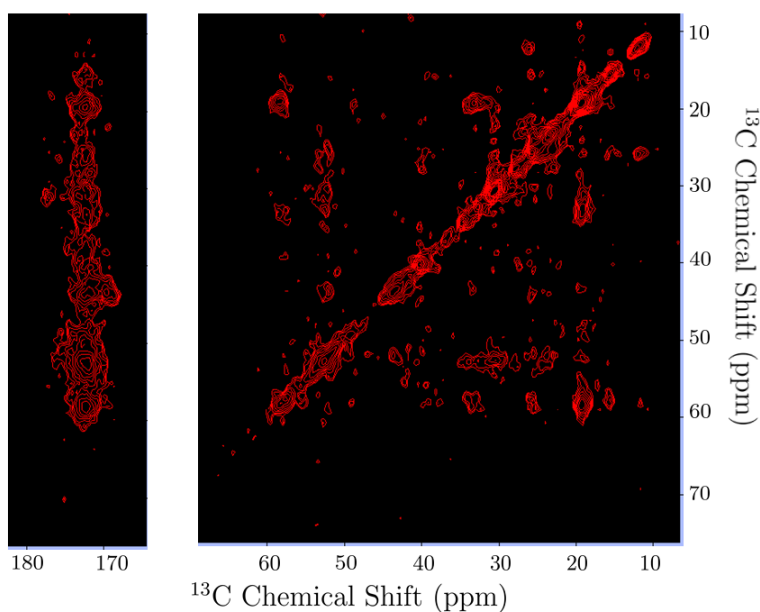


Figure 4.33: 2D  $^{13}\text{C}$ – $^{13}\text{C}$  DARR spectrum of  $^{13}\text{C}$ ,  $^{15}\text{N}$ –uniformly labeled peptide  $\text{A}\beta_{1-42}$  reconstituted in lipid membrane recorded at 600 MHz resonance with 100 ms mixing time.

After these NMR measurements, we aimed at determining the structure of the entire segments of  $\text{A}\beta_{1-42}$  and  $\text{pEA}\beta_{3-42}$  in lipid environment. The synthesis of  $\text{pEA}\beta_{3-42}$  was little bit challenging and time consuming so we decided to start with full length  $\text{A}\beta_{1-42}$ . For this purpose, we purchased  $^{13}\text{C}$ ,  $^{15}\text{N}$ –uniformly labeled recombinant peptide  $\text{A}\beta_{1-42}$ . In order to yield better spectra and sample quality, we used organic phase mixing reconstitution method by lyophilisation in cyclohexane.

This method provided optimal sample packing with almost identical final sample condition.

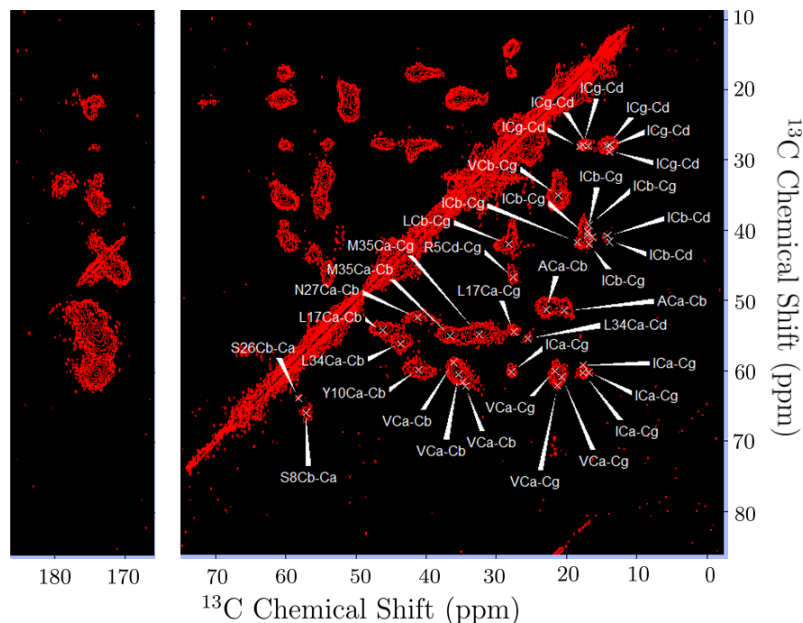


Figure 4.34: 2D  $^{13}\text{C}$ – $^{13}\text{C}$  DARR spectrum of  $^{13}\text{C}$ ,  $^{15}\text{N}$ –uniformly labeled peptide  $\text{A}\beta_{1-42}$  reconstituted in lipid membrane recorded at 800 MHz resonance with 25 ms mixing time.

The 2D  $^{13}\text{C}$ – $^{13}\text{C}$  DARR spectrum of  $^{13}\text{C}$ ,  $^{15}\text{N}$ –uniformly labeled  $\text{A}\beta_{1-42}$  was recorded at 600 MHz resonance with mixing time 100 ms in lipid membrane in the peptide to lipid molar ratio of 1 : 25 as shown in Fig. 4.33. The sample quality and spectral resolution was found very good with linewidth of 1 ppm or less. DARR spectra were also recorded at 800 MHz resonance with 25 ms and 50 ms mixing to probe intra–residue contacts as shown in Figures 4.34 and 4.35 respectively. The higher mixing time of 50 ms did not produce any additional features other than some longer side chain contacts like  $\text{LC}_\beta\text{--C}_\delta$ ,  $\text{IC}_\alpha\text{--C}_\delta$ ,  $\text{IC}_\beta\text{--C}_\delta$ ,  $\text{IC}_\gamma\text{--C}_\delta$  as shown in Fig. 4.35.

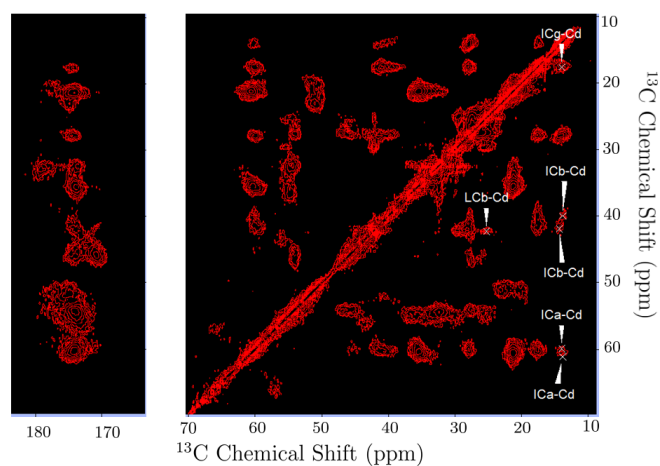


Figure 4.35: 2D  $^{13}\text{C}$ – $^{13}\text{C}$  DARR spectrum of  $^{13}\text{C}$ ,  $^{15}\text{N}$ –uniformly labeled  $\text{A}\beta_{1-42}$  reconstituted in lipid membrane recorded at 800 MHz resonance with 50 ms mixing time.

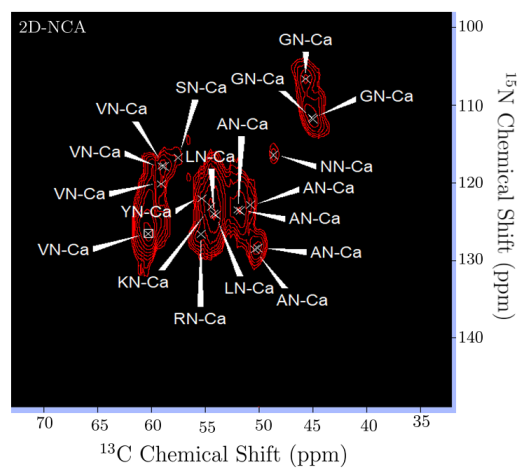


Figure 4.36: 2D NCA spectra of  $^{13}\text{C}$ ,  $^{15}\text{N}$ –uniformly labeled  $\text{A}\beta_{1-42}$  recorded at 600 MHz resonance in lipid membrane.

Using 1D and 2D  $^{13}\text{C}$ – $^{13}\text{C}$  DARR spectrum of segmentally labeled and fully labeled peptide, we were able to make residue type assignments of some of the residues. We also used 2D–NCA and 2D–NCO to identify some additional residues as shown in Fig. 4.36 and Fig. 4.37.

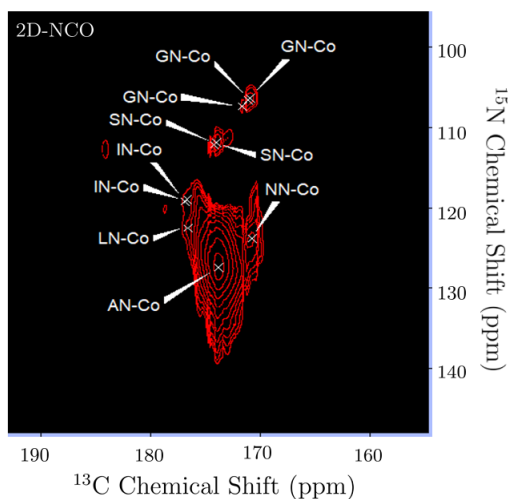


Figure 4.37: 2D NCO spectra of  $^{13}\text{C}$ ,  $^{15}\text{N}$ –uniformly labeled  $\text{A}\beta_{1-42}$  recorded at 600 MHz resonance in lipid membrane.

However, to find tertiary structure and dynamics, sequential assignments will be needed. For this, we need 3D NCACX and 3D NCOCX. Some of the chemical shift values of identified residues are shown in Table C.5 in Appendix. The complete sequential assignment of these residues is in progress. These chemical shift information is used to find the secondary and tertiary structure of the peptide in lipid membrane. TALOS–N [148] can be used to predict the backbone and side–chain torsion angle restraints. Using these data together with sequential assignments, the detail structural of these neurotoxic peptides in lipid membrane will be revealed.



## CHAPTER 5: CONCLUSION

In this chapter, I will summarize the important findings documented in this dissertation and future outlook. First, the elusive nature of membrane binding mechanism of  $A\beta_{25-35}$  was qualitatively established using experimental procedures. The role of electrostatics in these binding processes were illustrated using microelectrophoresis experiments. Moreover, the membrane-active structures of these toxic species were documented precisely. The molecular assembly mechanism, oligomeric state of these species in active state, *i.e.* membrane disrupting and pore forming conformation were also analyzed.

We also shed light on the complex role of cholesterol in  $A\beta_{25-35}$  binding to membrane. To be precise, key parameters governing the effect of cholesterol such as experimental rate constant, rate constant of pore formation, peptide–peptide affinity constant, and the number of oligomeric units in the pore complex were also established along with complete qualitative pathway of structural transitions in these processes. We also monitored experimentally underlying changes in the lipid structure and phase during interaction with the peptide with various cholesterol composition. Our data proved that cholesterol has a dual role during these binding events. It preferentially interacts with peptide at low concentration, makes lipid more condensed at intermediate concentration and at very high concentration it makes membrane disordered. Moreover, using experimental data, we established the structure of the pore as hexamers of hexamers of diameter 13 Å in  $\beta$ -barrel conformation. These findings will help clear very divergent existing membrane-pore models which is a key step towards therapeutic anti–Alzheimer’s drug design.

The second part of this work helped to understand the early stage aggregation pathways of  $A\beta_{1-42}$ . The use of exogenous fluorophores can affect the fiber formation and they are insensitive to formation of soluble oligomers which are the most cytotoxic species. Hence, we used intrinsic FRET

to qualitatively indicate the temporal dissection of oligomerization, the onset and progression of fibrillogenesis. This allowed us to monitor the entire process of aggregation. This is another important work because exact knowledge of temporal points on the initiation of oligomer formation and fibrillogenesis is a key to drug development that can hinder the oligomerization pathway.

Finally, in order to extrapolate and compare the cytotoxic effects of  $A\beta_{25-35}$  to full length peptides  $A\beta_{1-42}$  and pEA $\beta_{3-42}$ , we performed solid state NMR characterization to find the structure of these peptides in membrane-active conformation. Because most of the components in  $A\beta$  deposits are full length peptides, it is important to also understand the membranotropic role of these peptides as well. Our data again points in the direction of formation of fibrillary  $\beta$ -sheets even with these full length peptides. This work is aimed at providing detail structure of these full length peptides so that it will contribute to a more precise and targeted therapeutic drug design.

## **APPENDIX A: LIST OF ABBREVIATIONS**

The following abbreviations have been used in this dissertation:

AD: Alzheimer's Disease

APP: Amyloid Precursor Protein

ACH: Amyloid Cascade Hypothesis

A $\beta$ : Amyloid Beta

pEA $\beta$ : Pyroglutamylated Amyloid Beta

POPC/PC: 1-Palmitoyl-2-Oleoyl-Phosphatidylcholine

POPG/PG: 1-Palmitoyl-2-Oleoyl-Phosphatidylglycerol

HFIP: Hexafluoroisopropanol

Quin-2: 2 - [(2-Amino-5-methylphenoxy)methyl]-6-methoxy-8-aminoquinoline-N,N,  
N',N'-tetraacetic acid tetrapotassium salt

ThT: Thioflavin T

Phe (F): Phenylalanine

Tyr (Y): Tyrosine

Trp (W): Tryptophan

Cryo-EM: Cryo Electron Microscopy

CD: Circular Dichroism

CPL: Circularly Polarized Light

PEM: Photoelastic Modulator

UV: Ultraviolet

PTM: Photomultiplier Tube

IRE: Internal Reflection Element

DS: Difference Spectrum

FS: Fluorescence Spectroscopy

FTIR: Fourier Transform Infrared Spectroscopy

ATR-FTIR: Attenuated Total Reflection Fourier Transform Infrared Spectroscopy

SSNMR: Solid State Nuclear Magnetic Resonance

FID: Free Induction Decay

TMS: Tetramethylsilane

FRET: Forster Resonance Energy Transfer

RET: Resonance Energy Transfer

DLS: Dynamic Light Scattering

GP: Generalized Polarization

MAS: Magic Angle Spinning

FWHM: Full Width Half Maximum

DARR: Dipolar Assisted Rotational Resonance

TPPM: Two-Pulse-Phase Modulation

REDOR: Rotational Echo-Double Resonance

CP: Cross Polarization

CaN: Calcineurons

LTP: Long Term Potentiation

LTD: Long Term Depression

MLV: Multilamellar Vesicles

LUV: Large Unilamellar Vesicles

**APPENDIX B: SUPPLEMENTARY DATA OF MEMBRANE PORE  
FORMATION**

Table B.1: Concentrations of Membrane Bound Peptide  $[P_b]$  ( $\mu\text{M}$ ) at Various Aggregation Numbers:  $z = 1$ ,  $z = 4$  and  $z = 8$

NaCl (mM)	$[P]$ ( $\mu\text{M}$ )	$F_{rel}$	$k_{exp}$ ( $\text{s}^{-1}$ )	$[P_b]$ ( $z = 1$ )	$[P_b]$ ( $z = 4$ )	$[P_b]$ ( $z = 8$ )
10	20	0.1662	$5.18 \times 10^{-2}$	2.86	0.766	0.400
10	40	0.5094	$2.69 \times 10^{-2}$	3.27	0.834	0.423
10	66.7	0.6388	$2.30 \times 10^{-2}$	3.50	0.875	0.439
30	20	0.1691	$1.44 \times 10^{-2}$	1.88	0.515	0.276
30	40	0.3564	$1.85 \times 10^{-2}$	2.16	0.563	0.292
30	66.7	0.5263	$2.28 \times 10^{-2}$	2.30	0.589	0.301
50	20	0.1249	$4.33 \times 10^{-2}$	2.01	0.523	0.269
50	40	0.2779	$2.50 \times 10^{-2}$	2.41	0.600	0.299
50	66.7	0.4128	$3.17 \times 10^{-2}$	2.64	0.648	0.319
75	20	0.1123	$2.04 \times 10^{-2}$	1.76	0.493	0.271
75	40	0.2137	$3.66 \times 10^{-2}$	2.21	0.577	0.303
75	66.7	0.3530	$3.06 \times 10^{-2}$	2.49	0.630	0.323
150	20	0.0898	$1.19 \times 10^{-2}$	1.75	0.315	0.107
150	40	0.1244	$1.63 \times 10^{-2}$	2.22	0.416	0.145
150	66.7	0.1955	$1.26 \times 10^{-2}$	2.50	0.489	0.174
180	66.7	0.1089	$3.00 \times 10^{-2}$	2.47	0.459	0.147
225	66.7	0.1758	$6.18 \times 10^{-2}$	2.41	0.381	0.088
300	66.7	0.163	$4.41 \times 10^{-2}$	2.38	0.337	0.059

Table B.2: Second Order Rate Constant of Pore Formation  $k_a$  ( $M^{-1} s^{-1}$ ) at Various Aggregation

Numbers:  $z = 1$ ,  $z = 4$  and  $z = 8$

NaCl (mM)	[ $P$ ] ( $\mu$ M)	$F_{rel}$	$k_{exp}$ ( $s^{-1}$ )	$k_a$ ( $z = 1$ )	$k_a$ ( $z = 4$ )	$k_a$ ( $z = 8$ )
10	20	0.1662	$5.18 \times 10^{-2}$	$5.907 \times 10^3$	$2.206 \times 10^4$	$4.224 \times 10^4$
10	40	0.5094	$2.69 \times 10^{-2}$	$5.925 \times 10^3$	$2.323 \times 10^4$	$4.581 \times 10^4$
10	66.7	0.6388	$2.30 \times 10^{-2}$	$1.255 \times 10^4$	$5.020 \times 10^4$	$1.001 \times 10^5$
30	20	0.1691	$1.44 \times 10^{-2}$	$1.693 \times 10^4$	$6.178 \times 10^4$	$1.153 \times 10^5$
30	40	0.3564	$1.85 \times 10^{-2}$	$2.942 \times 10^4$	$1.129 \times 10^5$	$2.176 \times 10^5$
30	66.7	0.5263	$2.28 \times 10^{-2}$	$2.923 \times 10^4$	$1.142 \times 10^5$	$2.234 \times 10^5$
50	20	0.1249	$4.33 \times 10^{-2}$	$6.527 \times 10^4$	$2.508 \times 10^4$	$4.877 \times 10^4$
50	40	0.2779	$2.50 \times 10^{-2}$	$1.393 \times 10^4$	$5.596 \times 10^4$	$1.123 \times 10^5$
50	66.7	0.4128	$3.17 \times 10^{-2}$	$2.452 \times 10^4$	$9.990 \times 10^4$	$2.026 \times 10^5$
75	20	0.1123	$2.04 \times 10^{-2}$	$2.631 \times 10^4$	$9.391 \times 10^4$	$1.708 \times 10^5$
75	40	0.2137	$3.66 \times 10^{-2}$	$4.563 \times 10^4$	$1.748 \times 10^5$	$3.328 \times 10^5$
75	66.7	0.3530	$3.06 \times 10^{-2}$	$3.297 \times 10^4$	$1.303 \times 10^5$	$2.542 \times 10^5$
150	20	0.0898	$1.19 \times 10^{-2}$	$1.776 \times 10^4$	$9.871 \times 10^4$	$2.906 \times 10^5$
150	40	0.1244	$1.63 \times 10^{-2}$	$1.313 \times 10^4$	$7.010 \times 10^4$	$2.011 \times 10^5$
150	66.7	0.1955	$1.26 \times 10^{-2}$	$1.296 \times 10^4$	$6.626 \times 10^4$	$1.862 \times 10^5$
180	66.7	0.1089	$3.00 \times 10^{-2}$	$2.561 \times 10^3$	$1.381 \times 10^4$	$4.304 \times 10^4$
225	66.7	0.1758	$6.18 \times 10^{-2}$	$4.103 \times 10^2$	$2.595 \times 10^3$	$1.121 \times 10^4$
300	66.7	0.163	$4.41 \times 10^{-2}$	$2.385 \times 10^2$	$1.684 \times 10^3$	$9.538 \times 10^3$



Table B.3: Peptide–Peptide Affinity Constant  $K_P$  ( $M^{-1}$ ) at Various Aggregation Numbers:  $z = 1$ ,  $z = 4$  and  $z = 8$

NaCl (mM)	$[P]$ ( $\mu M$ )	$F_{rel}$	$k_{exp}$ ( $s^{-1}$ )	$K_P$ ( $z = 1$ )	$K_P$ ( $z = 4$ )	$K_P$ ( $z = 8$ )
10	20	0.1662	$5.18 \times 10^{-2}$	$1.141 \times 10^5$	$4.258 \times 10^5$	$8.155 \times 10^5$
10	40	0.5094	$2.69 \times 10^{-2}$	$2.199 \times 10^5$	$8.623 \times 10^5$	$1.700 \times 10^6$
10	66.7	0.6388	$2.30 \times 10^{-2}$	$5.458 \times 10^5$	$2.183 \times 10^6$	$4.351 \times 10^6$
30	20	0.1691	$1.44 \times 10^{-2}$	$1.489 \times 10^6$	$5.437 \times 10^6$	$1.014 \times 10^7$
30	40	0.3564	$1.85 \times 10^{-2}$	$1.593 \times 10^6$	$6.114 \times 10^6$	$1.179 \times 10^7$
30	66.7	0.5263	$2.28 \times 10^{-2}$	$1.282 \times 10^6$	$5.004 \times 10^6$	$9.792 \times 10^6$
50	20	0.1249	$4.33 \times 10^{-2}$	$1.508 \times 10^5$	$5.797 \times 10^5$	$1.127 \times 10^6$
50	40	0.2779	$2.50 \times 10^{-2}$	$5.577 \times 10^5$	$2.240 \times 10^6$	$4.495 \times 10^6$
50	66.7	0.4128	$3.17 \times 10^{-2}$	$7.739 \times 10^5$	$3.153 \times 10^6$	$6.406 \times 10^6$
75	20	0.1123	$2.04 \times 10^{-2}$	$1.287 \times 10^6$	$4.595 \times 10^6$	$8.359 \times 10^6$
75	40	0.2137	$3.66 \times 10^{-2}$	$1.247 \times 10^6$	$4.777 \times 10^6$	$9.096 \times 10^6$
75	66.7	0.3530	$3.06 \times 10^{-2}$	$1.070 \times 10^6$	$4.255 \times 10^6$	$8.300 \times 10^6$
150	20	0.0898	$1.19 \times 10^{-2}$	$1.491 \times 10^6$	$8.285 \times 10^6$	$2.439 \times 10^7$
150	40	0.1244	$1.63 \times 10^{-2}$	$8.041 \times 10^5$	$4.291 \times 10^6$	$1.231 \times 10^7$
150	66.7	0.1955	$1.26 \times 10^{-2}$	$1.028 \times 10^6$	$5.256 \times 10^6$	$1.477 \times 10^7$
180	66.7	0.1089	$3.00 \times 10^{-2}$	$8.533 \times 10^5$	$4.603 \times 10^6$	$1.434 \times 10^7$
225	66.7	0.1758	$6.18 \times 10^{-2}$	$6.642 \times 10^5$	$4.201 \times 10^6$	$1.185 \times 10^7$
300	66.7	0.163	$4.41 \times 10^{-2}$	$5.407 \times 10^5$	$3.819 \times 10^6$	$2.163 \times 10^7$

Table B.4: Oligomeric State (Number of Peptide Oligomers) of the Pore  $n$

NaCl (mM)	[ $P$ ] ( $\mu$ M)	$F_{rel}$	$k_{exp}$ ( $s^{-1}$ )	$n$ (No. of Oligomers)
10	20	0.1662	$5.18 \times 10^{-2}$	3.4
10	40	0.5094	$2.69 \times 10^{-2}$	2.6
10	66.7	0.6388	$2.30 \times 10^{-2}$	3.1
30	20	0.1691	$1.44 \times 10^{-2}$	8.2
30	40	0.3564	$1.85 \times 10^{-2}$	6.3
30	66.7	0.5263	$2.28 \times 10^{-2}$	4.4
50	20	0.1249	$4.33 \times 10^{-2}$	3.6
50	40	0.2779	$2.50 \times 10^{-2}$	4.8
50	66.7	0.4128	$3.17 \times 10^{-2}$	4.6
75	20	0.1123	$2.04 \times 10^{-2}$	8.6
75	40	0.2137	$3.66 \times 10^{-2}$	7.4
75	66.7	0.3530	$3.06 \times 10^{-2}$	5.7
150	20	0.0898	$1.19 \times 10^{-2}$	9.8
150	40	0.1244	$1.63 \times 10^{-2}$	7.4
150	66.7	0.1955	$1.26 \times 10^{-2}$	7.5
180	66.7	0.1089	$3.00 \times 10^{-2}$	8.4
225	66.7	0.1758	$6.18 \times 10^{-2}$	6.3
300	66.7	0.163	$4.41 \times 10^{-2}$	5.9

Table B.5: Concentrations of Membrane Bound Peptide  $[P_b]$  ( $\mu\text{M}$ ) at Various Aggregation Numbers:  $z = 1$ ,  $z = 4$  and  $z = 8$  for Zwitterionic Lipid Vesicles Composed of 90 % POPG and 10 % Cholesterol in Buffer Containing 75 mM NaCl, 30 mM Myo-Inositol, 6 mM  $\text{CaCl}_2$ , and 20 mM Tris-HCl (pH 7.2)

$[P]$ ( $\mu\text{M}$ )	$F_{rel}$	$k_{exp}$ ( $\text{s}^{-1}$ )	$[P_b]$ ( $z = 1$ )	$[P_b]$ ( $z = 4$ )	$[P_b]$ ( $z = 8$ )
20	0.01697	$1.058 \times 10^{-2}$	1.05	0.0573	0.00301
40	0.04197	$1.314 \times 10^{-2}$	1.52	0.0980	0.00582
66.7	0.1018	$1.051 \times 10^{-2}$	1.88	0.139	0.00929

Table B.6: Second Order Rate Constant of Pore Formation  $k_a$  ( $\text{M}^{-1} \text{s}^{-1}$ ) at Various Aggregation Numbers:  $z = 1$ ,  $z = 4$  and  $z = 8$  for Zwitterionic Lipid Vesicles Composed of 90 % POPG and 10 % Cholesterol in Buffer Containing 75 mM NaCl, 30 mM Myo-Inositol, 6 mM  $\text{CaCl}_2$ , and 20 mM Tris-HCl (pH 7.2)

$[P]$ ( $\mu\text{M}$ )	$F_{rel}$	$k_{exp}$ ( $\text{s}^{-1}$ )	$k_a$ ( $z = 1$ )	$k_a$ ( $z = 4$ )	$k_a$ ( $z = 8$ )
20	0.01697	$1.058 \times 10^{-2}$	$7.575 \times 10^3$	$1.388 \times 10^5$	$2.642 \times 10^6$
40	0.04197	$1.314 \times 10^{-2}$	$7.684 \times 10^3$	$1.192 \times 10^5$	$2.007 \times 10^6$
66.7	0.1018	$1.051 \times 10^{-2}$	$7.082 \times 10^3$	$9.580 \times 10^4$	$1.434 \times 10^6$

Table B.7: Peptide–Peptide Affinity Constant  $K_p$  ( $M^{-1}$ ) at Various Aggregation Numbers:  $z = 1$ ,  $z = 4$  and  $z = 8$  for Zwitterionic Lipid Vesicles Composed of 90 % POPG and 10 % Cholesterol in Buffer (75 mM NaCl, 30 mM Myo–Inositol, 6 mM  $CaCl_2$ , and 20 mM Tris–HCl, pH 7.2)

$[P]$ ( $\mu M$ )	$F_{rel}$	$k_{exp}$ ( $s^{-1}$ )	$K_p$ ( $z = 1$ )	$K_p$ ( $z = 4$ )	$K_p$ ( $z = 8$ )
20	0.01697	$1.058 \times 10^{-2}$	$7.159 \times 10^5$	$1.312 \times 10^7$	$2.497 \times 10^8$
40	0.04197	$1.314 \times 10^{-2}$	$5.863 \times 10^5$	$9.053 \times 10^6$	$1.525 \times 10^8$
66.7	0.1018	$1.051 \times 10^{-2}$	$6.737 \times 10^5$	$9.114 \times 10^6$	$1.364 \times 10^8$

Table B.8: Oligomeric State of the Pore  $n$  at Various Aggregation Numbers:  $z = 1$ ,  $z = 4$  and  $z = 8$  for Zwitterionic Lipid Vesicles Composed of 90 % POPG and 10 % Cholesterol in Buffer Containing 75 mM NaCl, 30 mM Myo–Inositol, 6 mM  $CaCl_2$ , and 20 mM Tris–HCl at pH 7.2

$[P]$ ( $\mu M$ )	$F_{rel}$	$k_{exp}$ ( $s^{-1}$ )	$n$
20	0.01697	$1.058 \times 10^{-2}$	8.1
40	0.04197	$1.314 \times 10^{-2}$	7.3
66.7	0.1018	$1.051 \times 10^{-2}$	6.8

## **APPENDIX C: SUPPLEMENTARY DATA OF FTIR AND ssNMR**

Table C.1:  $I_{\beta}/I_{\alpha}$  Values for  $A\beta_{1-42}$  Reconstituted in Lipid Membrane in Buffer Consisting of 10 mM Na,K-Phosphate with pD 7.2, in Peptide to Lipid Ratio of  $P : L = 1 : 50$ . Lipid Composition is 60 % POPC, 30 % POPG and 10 % Cholesterol

Time (h)	$I_{\beta}/I_{\alpha}$	Time (h)	$I_{\beta}/I_{\alpha}$
2.93	1.102711	40.91	2.56057
4.93	1.147687	52.68	2.490982
5.41	1.202958	65.25	2.547443
5.66	1.346677	77.66	2.500884
5.90	1.398877	88.85	2.380106
6.18	1.46033	101.11	2.384582
6.41	1.587431	111.31	2.501619
6.98	1.748604	123.25	2.426039
7.45	2.273357	135.70	2.474541
30.95	2.713397		

Table C.2:  $I_{\beta}/I_{\alpha}$  Values for pEA $\beta_{3-42}$  Reconstituted in Lipid Membrane in Buffer Consisting of 10 mM Na,K–Phosphate with pD 7.2, in Peptide to Lipid Ratio of  $P : L = 1 : 50$ . Lipid Composition is 60 % POPC, 30 % POPG and 10 % Cholesterol

Time (h)	$I_{\beta}/I_{\alpha}$	Time (h)	$I_{\beta}/I_{\alpha}$
0	0.763505	25.8667	1.77796
3.01667	1.41842	34.9	1.77212
3.31667	1.43812	40.65	1.72761
3.7	1.46271	56.95	1.49936
4.21667	2.02377	62.2667	1.50759
4.9333	2.11994	69.85	1.52298
8	2.7835	81.8667	1.57029
12.55	3.27698	93.3667	1.61269
15.5667	3.43633	105.8	1.66204
20.55	1.78781	118.7	1.72867

Table C.3:  $^{13}\text{C}$  Chemical Shift and FWHM of Pure Lipid and  $\text{A}\beta_{1-42}$  with  $^{13}\text{C}$  Uniformly Labeled Residues in the Region  $^{16}\text{K}^{17}\text{L}^{18}\text{V}$ . Lipid Composition is 60 % POPC, 30 % POPG, and 10 % Cholesterol

Sample	Region of Interest	$^{13}\text{C}$ Chemical Shift (ppm)	Line Width (ppm)
Lipid Mixture *	Aliphatic: $\alpha\text{CH}_2$	34.702	1.294
	Aliphatic: $(\omega-2)\text{CH}_2$	32.731	
	Aliphatic: $(\text{CH}_2)_n$	30.809	
	Aliphatic: $\beta\text{CH}_2$	28.038	
	Aliphatic: $(\omega-1)\text{CH}_2$	25.702	
	Aliphatic: $\omega\text{CH}_3$	23.327	
	Triacylglycerol (glyc-1,3)	64.358	0.485
	Triacylglycerol (glyc-2)	71.256	0.486
	Olefinic $\text{CH}_2$	130.335	0.324
$\text{A}\beta_{1-42}$ ( $^{16}\text{K}^{17}\text{L}^{18}\text{V}$ )	$\text{C}=\text{O}$	172.759	3.39
	$\text{C}_\alpha$	59.138, 52.502	2.42, 3.075
	$\text{C}_\beta$	40.687, 32.918	4.53, 3.076
	$\text{C}_\gamma$	24.340, 18.999	5.17, 4.53



Table C.4:  $^{13}\text{C}$  Chemical Shift and FWHM of  $\text{A}\beta_{1-42}$  and  $\text{pEA}\beta_{3-42}$  with  $^{13}\text{C}$  Uniformly Labeled Residues in the Region  $^{36}\text{V}^{37}\text{G}^{38}\text{G}^{39}\text{V}$  in Lipid Membrane. Lipid Composition is 60 % POPC, 30 % POPG, and 10 % Cholesterol

Sample	Region of Interest	$^{13}\text{C}$ Chemical Shift (ppm)	Line Width (ppm)
$\text{A}\beta_{1-42}$ ( $^{16}\text{K}^{17}\text{L}^{18}\text{V}$ ) in Lipid	C=O	172.196, 169.444	1.942, 1.943
	$\text{C}_\alpha$	57.653, 57.310, 43.838	1.832, 1.78
	$\text{C}_\beta$	—	—
	$\text{C}_\gamma$	19.515	1.459
$\text{pEA}\beta_{3-42}$ ( $^{16}\text{K}^{17}\text{L}^{18}\text{V}$ ) in Lipid	C=O	171.387, 168.635	1.943, 1.78
	$\text{C}_\alpha$	57.111, 43.352	2.49, 1.94
	$\text{C}_\beta$	33.479	1.96
	$\text{C}_\gamma$	19.073	1.295

Table C.5:  $^{13}\text{C}$  Chemical Shift and FWHM of Identified Residues of  $^{13}\text{C}$ ,  $^{15}\text{N}$  Uniformly Labeled  $\text{A}\beta_{1-42}$  in Lipid Membrane. Lipid Composition is 60 % POPC, 30 % POPG, and 10 % Cholesterol at Peptide to Lipid Ratio  $P : L = 1 : 25$

Identified Residues	Region of Interest	$^{13}\text{C}$ Chemical Shift Value (ppm)
Ile (I)	$\text{C}_\alpha$	59.187 – 60.270
	$\text{C}_\beta$	39.288 – 41.967
	$\text{C}_\gamma$	16.790 – 18.550
	$\text{C}_\delta$	13.913 – 14.224
Ala (A)	$\text{C}_\alpha$	51.421, 51.300
	$\text{C}_\beta$	20.344, 22.892
	$\text{C}_\gamma$	33.479
Leu (L)	$\text{C}_\alpha$	54.212 – 56.154
	$\text{C}_\beta$	41.957 – 46.189
	$\text{C}_\gamma$	27.503 – 28.231
	$\text{C}_\delta$	25.562
Val (V)	$\text{C}_\alpha$	58.823 – 62.220
	$\text{C}_\beta$	34.419 – 36.188
	$\text{C}_\gamma$	19.073
Met (M)	$\text{C}_\alpha$	54.819, 55.062
	$\text{C}_\beta$	36.603
	$\text{C}_\gamma$	32.478

Identified Residues	Region of Interest	<sup>13</sup> C Chemical Shift Value (ppm)
Arg (R)	C <sub>γ</sub>	27.624
	C <sub>δ</sub>	46.689
Asn (N)	C <sub>α</sub>	52.392
	C <sub>β</sub>	41.214
Tyr (Y)	C <sub>α</sub>	59.915
	C <sub>β</sub>	41.093
Ser (S)	C <sub>α</sub>	58.201
	C <sub>β</sub>	63.919

Table C.6: Random Coil  $^{13}\text{C}$  Chemical Shifts for the 20 Common Amino Acids

Residue	N	$\text{C}_o$	$\text{C}_\alpha$	$\text{C}_\beta$	Others
Ala (A)	123.8	175.9	50.5	18.1	—
Cys (reduced) C	118.8	173.0	56.4	27.1	—
Asp (D)	120.4	175	52.2	40.9	$\gamma\text{CO}$ 179.9
Glu (E)	120.2	174.9	54.2	29.2	$\gamma\text{CH}_2$ 35.0; $\delta\text{CO}$ 183
Phe (F)	120.3	174.4	55.6	39.1	1C 138.9; 2, 6CH 132.1; 3, 5CH 131.4; 4CH 129.9
Gly (G)	108.8	174.5	44.5	—	—
His (H)	118.2	172.6	53.3	29.0	2CH 136.3; 4CH 120.3; 5C 131.2
Ile (I)	119.9	175.0	58.7	38.7	$\gamma\text{CH}_2$ 26.9; $\gamma\text{CH}_3$ 17.1; $\delta\text{CH}_3$ 12.7
Lys (K)	120.4	174.8	54.2	32.6	$\gamma\text{CH}_2$ 24.6; $\delta\text{CH}_2$ 29.1; $\epsilon\text{CH}_2$ 41.9
Leu (L)	121.8	175.7	53.1	41.7	$\gamma\text{CH}$ 27.1; $\delta\text{CH}_3$ 25.1, 3.3
Met (M)	119.6	174.6	53.3	32.4	$\gamma\text{CH}_2$ 32.0; $\epsilon\text{CH}_3$ 17.0
Asn (N)	118.7	173.6	51.3	38.7	$\gamma\text{CO}$ 177.1
Pro (P)	147.3	171.4	61.5	30.9	$\gamma\text{CH}_2$ 27.2; $\delta\text{CH}_2$ 49.7
Glu (Q)	119.84	174.4	53.7	28.8	$\gamma\text{CH}_2$ 33.4; $\delta\text{CO}$ 180.5
Arg (R)	120.5	174.5	54.0	30.2	$\gamma\text{CH}_2$ 26.8; $\delta\text{CH}_2$ 43.4; $\epsilon\text{C}$ 159.6
Ser (S)	115.7	173.1	56.4	63.3	—
Thr (T)	113.6	173.2	59.8	69.8	$\gamma\text{CH}_3$ 21.4
Val (V)	119.2	174.9	59.8	32.6	$\gamma\text{CH}_3$ 20.9, 20.1
Trp (W)	121.3	174.8	55.7	28.9	2CH 127.3; 3C 111.3; 4CH 122.2; 5CH 124.8; 6CH 120.9; 7CH 114.7; 8C 138.8; 9C 129.6
Tyr (Y)	120.3	174.8	55.8	38.3	1C 130.7; 2, 6CH 133.5; 3, 5CH 118.2; 4C 157.3

## LIST OF REFERENCES

- [1] Rajasekhar, K.; Chakrabarti, M.; Govindaraju, T. Function and Toxicity of Amyloid  $\beta$  and Recent Therapeutic Interventions Targeting Amyloid  $\beta$  in Alzheimer's Disease. *ChemComm* **51**, 13434 – 13450, (2015).
- [2] Underwood, E. N. Alzheimer's Amyloid Theory Gets Modest Boost. *Science* **349**, 464, (2015).
- [3] Tycko, R. Alzheimer's Disease: Structure of Aggregates Revealed. *Nature* **537**, 492 – 493, (2016).
- [4] Pike, C. J.; Burdick, D.; Walencewicz, A. J. et al. Neurodegeneration Induced by Beta–Amyloid Peptides in Vitro—The Role of Peptide Assembly State. *Journal of Neuroscience* **13**, 1676 – 1687, (1993).
- [5] Tenzi, R. E.; Bertram, L. Twenty Years of the Alzheimer's Disease Amyloid Hypothesis: A Genetic Perspective. *Cell* **120**, 545 – 555, (2005).
- [6] Querforth, H. W.; LaFerla, F. M. Alzheimer's Disease. *The New England Journal of Medicine* **362**, 329 – 344, (2010).
- [7] Serrano–Pozo, A.; Frosch, M. P.; Masliah, E. et al. Neuropathological Alterations in Alzheimer Disease. *Cold Spring Harbor Perspective in Medicine* **1**, (2011).
- [8] Goedert, M. Alzheimer's and Parkinson's Disease. The Prion Concept in Relation to Assembled A $\beta$ , Tau and  $\alpha$ –synuclein. *Science* **349**, 6248, 1255555, (2015).
- [9] Cerasoli, E.; Ryadnov, M. G.; Austen, B. M. The Elusive Nature and Diagnostics of Misfolded A $\beta$  Oligomers. *Frontiers in Chemistry* **3**, (2015).

- [10] Quitterer, U.; AbdAlla, S. Pharmacol Res. Improvements of Symptoms of Alzheimer's Disease by Inhibition of the Angiotensin System. *Pharmacol Res*, (2019).
- [11] Hardy, J.; Allsop, D. Amyloid Deposition as the Central Event in the Etiology of Alzheimer's Disease. *Trends Pharmacol. Sci.* **2**, 383 – 388, (1991).
- [12] Hardy, J. The Amyloid Hypothesis for Alzheimer's Disease: A Critical Reappraisal. *J Neurochem*, 1129 – 1134, (2009).
- [13] Herholz, K.; Ebmeier, K. Clinical Amyloid Imaging in Alzheimer's Disease. *Lancet Neurology* **10**, 667 – 670, (2011).
- [14] Sievers, S. A.; Karanicolas, J.; Chang, H. W. et al. Structure–Based Design of Non–Natural Amino–Acid Inhibitors of Amyloid Fibril Formation. *Nature* **475**, 96 – 111, (2011).
- [15] Karran, E.; Mercken M.; De Strooper, B. The Amyloid Cascade Hypothesis for Alzheimer's Disease: An Appraisal for the Development of Therapeutics. *Nature Reviews Drug Discovery* **10**, 698 – 1600, (2011).
- [16] Gureviciene, I.; Gurevicius, K.; Mugantseva, E.; Kislin, M.; Khiroug, L.; Tanila, H. Amyloid Plaques Show Binding Capacity of Exogenous Injected Amyloid- $\beta$ . *J Alzheimers Dis.* **55**, 147 – 157, (2017).
- [17] Janus, C.; Pearson, J.; McLaurin, J. et al. A $\beta$  Peptide Immunization Reduces Behavioural Impairment And Plaques in a Model of Alzheimer's Disease. *Nature* **408**, 979 – 982, (2000).
- [18] Fessel, J. Amyloid is Essential but Insufficient for Alzheimer Causation: Addition of Subcellular Cofactors is Required for Dementia. *Int J Geriatr Psychiatry*, (2018).
- [19] Serpell, L. C. Alzheimer's Amyloid Fibrils: Structure and Assembly. *Biochem Biophys Acta* **1502**, 16 – 30, (2000).

- [20] Estrada, L. D.; Soto, C. Inhibition of Protein Misfolding and Aggregation by Small Rationally Designed Peptides. *Curr Pharm Des* **12**, 2557 – 2567, (2006).
- [21] Kirkitadze, M. D.; Bitan, G.; Teplow, D. B. Paradigm Shifts in Alzheimer's Disease and Other Neurodegenerative Disorders: The Emerging Role of Oligomeric Assemblies. *J. Neurosci. Res.* **69**, 567 – 577, (2002).
- [22] Benilova, I.; Karran, E.; De Strooper, B. The Toxic A $\beta$  Oligomer and Alzheimer's Disease: An Emperor in Need of Clothes. *Nat. Neurosci.* **15**, 349 – 357, (2012).
- [23] Lesne, S. E. et al. Brain Amyloid- $\beta$  Oligomers in Ageing and Alzheimer's Disease. *Brain* **136**, 1383 – 1398, (2013).
- [24] Selkoe, D. J.; Hardy, J. The Amyloid Hypothesis of Alzheimer's Disease at 25 years. *EMBO Mol. Med.* **8**, 595 – 608, (2016).
- [25] Kaye, R.; Lasagna-Reeves, C. A. Molecular Mechanisms of Amyloid Oligomers Toxicity. *J Alzheimers Dis.* **33**, (2013).
- [26] Chang, Z.; Luo, Y.; Zhang, Y.; Wei, G. Interactions of A $\beta_{25-35}$   $\beta$ -Barrel Like Oligomers With Anionic Lipid Bilayer and Resulting Membrane Leakage: An All Atom Molecular Dynamics Study. *The Journal of Physical Chemistry B* **115**, 1165 – 1174, (2011).
- [27] Do, T. D.; LaPointe, N. E.; Nelson, R.; Krotee, P.; Hayden, E. Y.; Ulrich, B.; Quan, S.; Feinstein, S. C.; Teplow, D. B.; Eisenberg, D.; et al. Amyloid  $\beta$ -Protein C-Terminal Fragments: Formation of Cylindrins and  $\beta$ -Barrels. *J. Am. Chem. Soc.* **138**, 549 – 557, (2016).
- [28] Di Scala, C.; Troadec, J. D.; Lelievre, C.; Garmy, N.; Fantini, J.; Chahinian, H. Mechanism of Cholesterol-Assisted Oligomeric Channel Formation by a Short Alzheimer  $\beta$ -Amyloid Peptide. *Journal of Neurochemistry* **128**, 186 – 195, (2014).

- [29] Chow, V. W.; Mattson, M. P.; Wong, P. C.; Gleichmann, M. An Overview of APP Processing Enzymes and Products. *NeuroMol. Med.* **12**, 1 – 12, (2010).
- [30] Agostinho, P.; Pliassova, A.; Oliveira, C. R.; Cunha, R. A. Localization and Trafficking of Amyloid- $\beta$  Protein Precursor and Secretases: Impact on Alzheimer's Disease. *J. Alzheimer's Dis.* **45**, 329 – 347, (2015).
- [31] Naldi, M., Fiori, J.; Pistolozzi, M.; Drake, A. F.; Bertucci, C.; Wu, R.; Mlynarczyk, K.; Filipek, S.; Simone, A. De; Andrisano, V. Amyloid  $\beta_{25-35}$  Peptide Self-Assembly and Its Inhibition: A Model Undecapeptide System to Gain Atomistic and Secondary Structure Details of the Alzheimer's Disease Process and Treatment. *ACS Chemical Neuroscience* **3**, 952 – 962, (2012).
- [32] Tsai, H. H.; Lee, J. B.; Tseng, S. S.; Pan, X. A.; Shih, Y. C. Folding and Membrane Insertion of A $\beta_{25-35}$  Peptide and its Mutants: Implications for Aggregation and Neurotoxicity. *Proteins* **78**, 1909 – 1925, (2010).
- [33] Tsai, H. H.; Lee, J. B.; Shih, Y. C.; Wan, L.; Shieh, F. K.; Chen, C. Y. Location and Conformation of A $\beta_{25-35}$  Peptide and its Sequence-Shuffled Peptides within Membranes: Implications for Aggregation and Toxicity in PC12 Cells. *ChemMedChem* **9**, 1002 – 1011, (2014).
- [34] Di Scala, C.; Troadec, J. D.; Lelievre, C.; Garmy, N.; Fantini, J.; Chahinian, H. Mechanism of Cholesterol-Assisted Oligomeric Channel Formation by a Short Alzheimer A $\beta$  Peptide. *J. Neurochem.* **128**, 186 – 195, (2014).
- [35] Di Scala, C.; Yahi, N.; Lelievre, C.; Garmy, N.; Chahinian, H.; Fantini, J. Biochemical Identification of a Linear Cholesterol-Binding Domain within Alzheimer's Amyloid  $\beta$  Peptide. *ACS Chem. Neurosci.* **4**, 509 – 517, (2013).



- [36] Di Scala, C.; Chahinian, H.; Yahy, N.; Garmy, N.; Fantini, J. Interaction of Alzheimer's Amyloid  $\beta$  Peptides with Cholesterol: Mechanistic Insights into Amyloid Pore Formation. *Biochemistry* **53**, 4489 – 4502, (2014).
- [37] Fantini, J.; Di Scala, C.; Yahy, N.; Troadec, J. D.; Sadelli, K.; Chahinian, H.; Garmy, N. Bexarotene Blocks Calcium-Permeable Ion Channels Formed by Neurotoxic Alzheimer's Amyloid  $\beta$  Peptides. *ACS Chem. Neurosci.* **5**, 216 – 224, (2014).
- [38] Dies, H.; Topozini, L.; Rheinstadter, M. C. The Interaction Between Amyloid- $\beta$  Peptides and Anionic Lipid Membranes Containing Cholesterol and Melatonin. *PLoS One* **9**, e99124, (2014).
- [39] Kohno, T.; Kobayashi, K.; Maeda, T.; Sato, K.; Takashima, A. Three-Dimensional Structures of the A $\beta_{25-35}$  in Membrane-Mimicking Environment. *Biochemistry* **35**, 16094 – 16104, (1996).
- [40] D'Ursi, A. M.; Armenante, M. R.; Guerrini, R.; Salvadori, S.; Sorrentino, G.; Picone, D. Solution Structure of A $\beta_{25-35}$  in Different Media. *J. Med. Chem.* **47**, 4231 – 4238, (2004).
- [41] Coles, M.; Bicknell, W.; Watson, A. A.; Fairlie, D. P.; Craik, D. J. Solution Structure of Amyloid  $\beta_{1-40}$  in a Water-Micelle Environment. Is the Membrane Spanning Domain Where We Think It Is? *Biochemistry* **37**, 11064 – 11077, (1998).
- [42] Jang, H.; Arce, F. T.; Ramachandran, S.; Capone, R.; Lal, R.; Nussinov, R.  $\beta$ -Barrel Topology of Alzheimer's  $\beta$ -Amyloid Ion Channels. *J. Mol. Biol.* **404**, 917 – 934, (2010).
- [43] Gillman, A. L.; Jang, H.; Lee, J.; Ramachandran, S.; Kagan, B. L.; Nussinov, R.; Arce, F. T. Activity and Architecture of Pyroglutamate-Modified pEA $\beta_{3-42}$  Pores. *J. Phys. Chem. B* **118**, 7335 – 7344, (2014).

- [44] Jang, H.; Connelly, L.; Arce, F. T.; Ramachandran, S.; Kagan, B. L.; Lal, R.; Nussinov, R. Mechanisms for the Insertion of Toxic, Fibrillike Amyloid  $\beta$  Oligomers into the Membrane. *J. Chem. Theory Comput.* **9**, 822 – 833, (2013).
- [45] Shafir, Y.; Durell, S.; Arispe, N.; Guy, H. R. Models of Membrane-Bound Alzheimer's A $\beta$  Peptide Assemblies. *Proteins* **78**, 3473 – 3487, (2010).
- [46] Lashuel, H. A.; Hartley, D.; Petre, B. M.; Walz, T.; Lansbury, P. T., Jr. Neurodegenerative Disease: Amyloid Pores from Pathogenic Mutations. *Nature* **418**, 291, (2002).
- [47] Lin, H.; Bhatia, R.; Lal, R. Amyloid  $\beta$  Protein Forms Ion Channels: Implications for Alzheimer's Disease Pathophysiology. *FASEB Journal* **15**, 2434, (2001).
- [48] Petkova, A. T.; Ishii, Y.; Balbach, J. J.; Antzutkin, O. N.; Leapman, R. D.; Delaglio, F.; Tycko, R. A Structural Model for Alzheimer's Amyloid  $\beta$  Fibrils Based on Experimental Constraints from Solid State NMR. *PNAS* **99**, 16742 – 16747, (2002).
- [49] Gremer, L.; Scholzel, D.; Schenk, C.; Reinartz, E.; Labahn, J.; Ravelli, R. B. G.; Tusche, M.; Lopez-Iglesias, C.; Hoyer, W.; Heise, H.; Willbold, D.; Schroder, G. F. Fibril Structure of Amyloid  $\beta_{1-42}$  by Cryo-Electron Microscopy. *Science* **358**, 116 – 119, (2017).
- [50] Xiong, J.; Roach, C. A.; Oshokoya, O. O.; Schroell, R. P.; Yakubu, R. A.; Eagleburger, M. K.; Cooley, J. W.; Ji, R. D. Role of Bilayer Characteristics on the Structural Fate of A $\beta_{1-40}$  and A $\beta_{25-40}$ . *Biochemistry* **53**, 3004 – 3011, (2014).
- [51] Kubo, T.; Nishimura, S.; Kumagai, Y.; Kaneko, I. In-Vivo Conversion of Racemized Beta-Amyloid ( $[D - Ser26]A\beta_{1-40}$  to Truncated and Toxic Fragments ( $[D - Ser26]A\beta_{25-35/40}$  and Fragment Presence in the Brains of Alzheimer's Patients. *J. Neurosci. Res.* **70**, 474 – 483, (2002).

- [52] Cuevas, E.; Lantz, S. M.; Tobon–Velasco, J. C.; Newport, G. D.; Wu, Q.; Virmani, A.; Ali, S. F.; Santamaria, A. On the In–Vivo Early Toxic Properties of  $A\beta_{25-35}$  Peptide in the Rat Hippocampus: Involvement of the Receptor For Advanced Glycation End Products and Changes in Gene Expression. *Neurotoxicol. Teratol.* **33**, 288 – 296, (2011).
- [53] Behensky, A. A.; Yasny, I. E.; Shuster, A. M.; Seredenin, S. B.; Petrov, A. V.; Cuevas, J. Stimulation of Sigma Receptors with Afobazole Blocks Activation of Microglia and Reduces Toxicity Caused by  $A\beta_{25-35}$ . *J. Pharmacol. Exp. Ther.* **347**, 458 – 467, (2013).
- [54] Behensky, A. A.; Yasny, I. E.; Shuster, A. M.; Seredenin, S. B.; Petrov, A. V.; Cuevas, J. Afobazole Activation of  $\sigma-1$  Receptors Modulates Neuronal Responses to  $A\beta_{25-35}$ . *J. Pharmacol. Exp. Ther.* **347**, 468 – 477, (2013).
- [55] Millucci, L.; Ghezzi, L.; Bernardini, G.; Santucci, A. Conformations and Biological Activities of Amyloid Beta Peptide  $A\beta_{25-35}$ . *Curr. Protein Pept. Sci.* **11**, 54 – 67, (2010).
- [56] Abramov, A. Y.; Ionov, M.; Pavlov, E.; Duchon, M. R. Membrane Cholesterol Content Plays a Key Role in the Neurotoxicity of  $A\beta$ : Implications for Alzheimer’s Disease. *Aging Cell* **10**, 595 – 603(2011).
- [57] Da Luz Eltchechem, C. et al. Transcranial LED Therapy on Amyloid– $\beta$  Toxin (25 – 35) in the Hippocampal Region of Rats. *Lasers Med. Sci.* **32**, 749 – 756, (2017).
- [58] Song, Y.; Li, P.; Liu, L.; Bortolini, C.; Dong, M. Nanostructural Differentiation and Toxicity of Amyloid– $\beta_{25-35}$  Aggregates Emerge from Distinct Secondary Conformation. *Sci. Rep.* **8**, 765, (2018).
- [59] Li, J.; Ji, X.; Zhang, J.; Shi, G.; Zhu, X.; Wang, K. Paeoniflorin Attenuates  $A\beta_{25-35}$  Induced Neurotoxicity in PC12 Cells by Preventing Mitochondrial Dysfunction. *Folia Neuropathol.* **52**, 285 – 290, (2014).

- [60] Cardinale, A. et al. Sublethal Doses of  $\beta$ -Amyloid Peptide Abrogate DNA-Dependent Protein Kinase Activity. *J. Biol. Chem.* **287**, 2618 – 2631, (2012).
- [61] Wang, J. et al. The Cooperative Behaviour of Antimicrobial Peptides in Model Membranes. *Biochim. Biophys. Acta* **1838**, 2870 – 2881, (2014).
- [62] Li, L.; Du, J.; Zou, L.; Xia, H.; Wu, T.; Kim, Y.; Lee, Y. The Neuroprotective Effects of Decursin Isolated from *Angelica gigas* Nakai against Amyloid  $\beta$  Protein Induced Apoptosis in PC 12 Cells via a Mitochondria Related Caspase Pathway. *Neurochem. Res.* **40**, 1555 – 1562, (2015).
- [63] Lahmy, V.; Long, R.; Morin, D.; Villard, V.; Maurice, T. Mitochondrial Protection by the Mixed Muscarinic/ $\sigma$ 1 Ligand ANAVEX2 – 73, a Tetrahydrofuran Derivative, in  $A\beta_{25-35}$  Peptide-Injected Mice, a Nontransgenic Alzheimer's Disease Model. *Front. Cell. Neurosci.* **8**, 463, (2014).
- [64] Chang, C. P.; Liu, Y. F.; Lin, H. J.; Hsu, C. C.; Cheng, B. C.; Liu, W. P.; Lin, M. T.; Hsu, S. F.; Chang, L. S.; Lin, K. C. Beneficial Effect of Astragaloside on Alzheimer's Disease Condition Using Cultured Primary Cortical Cells under  $A\beta$  Exposure. *Mol. Neurobiol.* **53**, 7329 – 7340, (2016).
- [65] Moreira, P. I.; Santos, M. S.; Moreno, A.; Oliveira, C. Amyloid Beta-Peptide Promotes Permeability Transition Pore in Brain Mitochondria. *Biosci. Rep.* **21**, 789 – 800, (2001).
- [66] Ren, R.; Zhang, Y.; Li, B.; Wu, Y.; Li, B. Effect of  $\beta$ -Amyloid (25 – 35) on Mitochondrial Function and Expression of Mitochondrial Permeability Transition Pore Proteins in Rat Hippocampal Neurons. *J. Cell. Biochem.* **112**, 1450 – 1457, (2011).

- [67] Mirzabekov, T.; Lin, M. C.; Yuan, W. L.; Marshall, P. J.; Carman, M.; Tomaselli, K.; Lieberburg, I.; Kagan, B. L. Channel Formation in Planar Lipid Bilayers by a Neurotoxic Fragment of the Beta–Amyloid Peptide. *Biochem. Biophys. Res. Commun.* **202**, 1142 – 1148, (1994).
- [68] Hertel, C.; Terzi, E.; Hauser, N.; Jakob–Rotne, R.; Seelig, J.; Kemp, J. A. Inhibition of the Electrostatic Interaction Between Beta–Amyloid Peptide and Membranes Prevents Beta–Amyloid–Induced Toxicity. *Proc. Natl. Acad. Sci.* **94**, 9412 – 9416, (1997).
- [69] Lin, M.C.; Kagan, B. L. Electrophysiologic Properties of Channels Induced by  $A\beta_{25-35}$  in Planar Lipid Bilayers. *Peptides* **23**, 1215 – 1228, (2002).
- [70] Peters, C.; Bascunan, D.; Opazo, C.; Aguayo, L. G. Differential Membrane Toxicity of Amyloid– $\beta$  Fragments by Pore Forming Mechanisms. *J. Alzheimers Dis.* **51**, 689 – 699, (2016).
- [71] Labbe, J.F.; Lefevre, T.; Guay-Begin, A.A.; Auger, M. Structure and Membrane Interactions of the  $A\beta_{25-35}$  as Viewed Using Spectroscopic Approaches. *Phys. Chem. Chem. Phys.* **15**, 7228 – 7239, (2013).
- [72] Ghobeh, M.; Ahmadian, S.; Meratan, A. A.; Ebrahim–Habibi, A.; Ghasemi, A.; Shafizadeh, M.; Nemat–Gorgani, M. Interaction of  $A\beta_{25-35}$  Fibrillation Products with Mitochondria: Effect of Small Molecule Natural Products. *Biopolymers* **102**, 473 – 486, (2014).
- [73] Accardo, A.; Shalabaeva, V.; Cotte, M.; Burghammer, M.; Krahn, R.; Riek, C.; Dante, S. Amyloid  $\beta$  Peptide Conformational Changes in the Presence of a Lipid Membrane System. *Langmuir* **30**, 3191 – 3198, (2014).
- [74] Mason, R. P.; Estermyer, J. D.; Kelly, J. F.; Mason, P. E. Alzheimer’s Disease Amyloid Beta Peptide (25 – 35) is Localized in the Membrane Hydrocarbon Core: X–ray Diffraction Analysis. *Biochem. Biophys. Res. Commun.* **222**, 78 – 82, (1996).

- [75] Dante, S.; Hauss, T.; Dencher, N. A. Insertion of Externally Administered  $A\beta_{25-35}$  and Perturbation of Lipid Bilayers. *Biochemistry* **42**, 13667 – 13672, (2003).
- [76] Dante, S.; Hauss, T.; Dencher, N. A. Cholesterol Inhibits the Insertion of the Alzheimer's Peptide  $A\beta_{25-35}$  in Lipid Bilayers. *Eur. Biophys. J.* **35**, 523 – 531, (2006).
- [77] Vitiello, G.; Di Marino, S.; D'Ursi, A. M.; D'Errico, G. Omega-3 Fatty Acids Regulate the Interaction of the Alzheimer's  $A\beta_{25-35}$  Peptide with Lipid Membranes. *Langmuir* **29**, 14239 – 14245, (2013).
- [78] Lau, T. L.; Gehman, J. D.; Wade, J. D.; Perez, K.; Masters, C. L.; Barnham, K. J.; Separovic, F. Membrane Interactions and the Effect of Metal Ions of the Amyloidogenic Fragment  $A\beta_{25-35}$  in Comparison to  $A\beta_{1-42}$ . *Biochim. Biophys. Acta* **1768**, 2400 – 2408, (2007).
- [79] Dante, S.; Hauss, T.; Dencher, N. A.  $A\beta_{25-35}$  Is Intercalated in Anionic and Zwitterionic Lipid Membranes to Different Extents. *Biophys. J.* **83**, 2610 – 2616, (2002).
- [80] Terzi, E.; Holzemann, G.; Seelig, J. Alzheimer's  $A\beta_{25-35}$ : Electrostatic Interactions with Phospholipid Membranes. *Biochemistry* **33**, 7434 – 7441, (1994).
- [81] D'Arrigo, C.; Tabaton, M.; Perico, A. N-Terminal Truncated Pyroglutamyl Amyloid Peptide pEA $\beta_{3-42}$  Shows a Faster Aggregation Kinetics Than the Full Length  $A\beta_{1-42}$ . *Biopolymers* **90**, (2009).
- [82] Schilling, S.; Zeitschel, U.; Hoffmann, T.; Heiser, U.; Francke, M.; Kehlen, A.; Holzer, M.; Hutter-Paier, B.; Prokesch, M.; Windisch, M.; Jagla, W.; Schlenzig, D.; Lindner, C.; Rudolph, T.; Reuter, G.; Cynis, H.; Montag, D.; Demuth, H. U.; Rossner, S. Glutaminyl Cyclase Inhibition Attenuates Pyroglutamate  $A\beta$  and Alzheimer's Disease Like Pathology. *Letters, Nature Medicine* **14**, (2008).

- [83] Lee, J.; Gillman, A. L.; Jang, H.; Ramachandran, S.; Kagan, B. L.; Nussinov, R.; Arce, F. T. Role of Fast Kinetics of Pyroglutamate Modified Amyloid Beta Oligomers in Membrane Binding and Membrane Permeability. *Biochemistry*, (2014).
- [84] Tong, B. C.; Wu, A. J.; Cheung K. H. Calcium Signaling in Alzheimer's Disease and Therapies. *Biochim Biophys Acta Mol Cell Res* **1865**, 1745 – 1760, (2018).
- [85] Supnet, C.; Bezprozvanny, I. The Dysregulation of Intracellular Calcium in Alzheimer Disease. *Cell Calcium* **47**, 183 – 189, (2010).
- [86] George–Hyslop, P. S. Molecular Genetics of Alzheimer's Disease. *Biol Psychiatry* **47**, 183 – 99, (2000).
- [87] Xiang, Y.; Zheng, J. Cholesterol Promotes the Interaction of Alzheimer A $\beta$  Monomer with Lipid Bilayer. *Journal of Molecular Biology* **421**, 561 – 571, (2012).
- [88] Solomon, A.; Kivipelto, M.; Wolozin, B.; Zhou, J.; Whitmer, R. A. Midlife Serum Cholesterol and Increased Risk of Alzheimer's and Vascular Dementia Three Decades Later. *Dement. Geriatr. Cogn. Disord.* **28**, 75 – 80, (2009).
- [89] Habchi, J. et al. Cholesterol Catalyses A $\beta_{1-42}$  Aggregation Through a Heterogeneous Nucleation Pathway in the Presence of Lipid Membranes. *Nat. Chem.* **10**, 673 – 683, (2018).
- [90] Barrett, P. J. et al. The Amyloid Precursor Protein Has a Flexible Transmembrane Domain and Binds Cholesterol. *Science* **336**, 1168 – 1171, (2012).
- [91] Avdulov, N. A. et al. Lipid Binding to Amyloid  $\beta$ -Peptide Aggregates: Preferential Binding of Cholesterol as Compared with Phosphatidylcholine and Fatty acids. *J. Neurochem.* **69**, 1746 – 1752, (1997).
- [92] Yu, X.; Zheng, J. Cholesterol Promotes the Interaction of Alzheimer  $\beta$ -Amyloid Monomer With Lipid Bilayer. *J. Mol. Biol.* **421**, 561 – 571, (2012).

- [93] Berthelot, K.; Cullin, C.; Lecomte, S. What Does Make an Amyloid Toxic: Morphology, Structure or Interaction With Membrane? *Biochimie* **95**, 12 – 19, (2013).
- [94] Ko, M. et al. Phosphatidylcholine Protects Neurons From Toxic Effects of Amyloid  $\beta$ – Protein in Culture. *Brain Res.* **1642**, 376 – 383, (2016).
- [95] Zhao, L. N.; Chiu, S. W.; Benoit, J.; Chew, L. Y.; Mu, Y. Amyloid  $\beta$  Peptides Aggregation in a Mixed Membrane Bilayer: A Molecular Dynamics Study. *J. Phys. Chem. B* **115**, 12247 – 12256, (2011).
- [96] Qiu, L.; Buie, C.; Reay, A.; Vaughn, M. W.; Cheng, K. H. Molecular Dynamics Simulations Reveal the Protective Role of Cholesterol in  $\beta$ –Amyloid Protein Induced Membrane Disruptions in Neuronal Membrane Mimics. *J. Phys. Chem. B* **115**, 9795 – 9812, (2011).
- [97] Vitiello, G.; Di Marino, S.; D’Ursi, A. M.; D’Errico, G. Omega–3 Fatty Acids Regulate the Interaction of the Alzheimer’s  $A\beta_{25-35}$  Peptide with Lipid Membranes. *Langmuir* **29**, 14239 – 14245, (2013).
- [98] D’Errico, G. et al. Interaction Between Alzheimer’s  $A\beta_{25-35}$  Peptide and Phospholipid Bilayers: The Role of Cholesterol. *Biochim. Biophys. Acta* **1778**, 2710 – 2716, (2008).
- [99] Tatulian, S. A.; Kandel, N. Membrane Pore Formation by Peptides Studied by Fluorescence Techniques. *Methods Mol. Biol.* **2003**, 449 – 464, (2019).
- [100] Garg, P.; Nemeč, K. N.; Khaled, A. R.; Tatulian, S. A. Transmembrane Pore Formation by the Carboxyl Terminus of Bax Protein. *Biochim. Biophys. Acta* **1828**, 732 – 742, (2013).
- [101] Kandel, N.; Zheng, T.; Huo, Q.; Tatulian, S. A. Membrane Binding and Pore Formation by A Cytotoxic Fragment of Amyloid  $\beta$  Peptide. *J. Phys. Chem. B* **121**, 10293 – 10305, (2017).
- [102] Tatulian, S. A. Structural Characterization of Membrane Proteins and Peptides by FTIR and ATR–FTIR Spectroscopy. *Methods Mol. Biol.* **974**, 177 – 218, (2013).



- [103] Goldblatt, G.; Matos, J. O.; Gornto, J.; Tatulian, S. A. Isotope–Edited FTIR Reveals Distinct Aggregation and Structural Behaviors of Unmodified and Pyroglutamylated Amyloid  $\beta$  Peptides. *Phys. Chem. Chem. Phys.* **17**, 32149 – 32160, (2015).
- [104] Foster, Th. Intermolecular Energy Migration and Fluorescence. *Ann. Phys. (Leipzig)* **2**, 55 – 75, (1948).
- [105] Stryer, L. Fluorescence Energy Transfer as Spectroscopic Ruler. *Annu. Rev. Biochem.* **47**, 819 – 846, (1978).
- [106] Lakowicz, J. R.. Principles of Fluorescence Spectroscopy. *Second Edition*, ISBN 0 – 306 – 46093 – 9, Kluwer Academic/Plenum Publishers, New York, (1999).
- [107] Cady, S. D.; Goodman, C.; Tatko, C. D.; DeGrado, W. F.; Hong, M. Determination of Orientation of Uniaxially Rotating Membrane Proteins Using Unoriented Samples. A  $^2\text{H}$ ,  $^{13}\text{C}$ ,  $^{15}\text{N}$  Solid State NMR Investigation of the Dynamics and Orientation of a Transmembrane Helical Bundle. *Journal of American Chemical Society* **129**, 5719 – 5729, (2007).
- [108] Bennett, A. E.; Rienstra, C. M.; Auger, M.; Lakshmi, K. V.; Griffin, R. G. Heteronuclear Decoupling in Rotating Solids. *Journal of Chemical Physics*, **103**, 6951 – 6958, (1995).
- [109] Takegoshi, K.; Mizokami, J.; Terao, T.  $^{13}\text{C}$ – $^1\text{H}$  Decoupling with Third Averaging in Solid NMR. *Chemical Physics Letters* **341**, 540 – 544, (2001).
- [110] Pines, A.; Gibby, M. G.; Waugh, J. S., Proton Enhanced NMR of Dilute Spins in Solids. *Journal of Chemical Physics* **59**, 569 – 590, (1973).
- [111] Delaglio, F. et al. NMRPipe: A Multidimensional Spectral Processing System Based on UNIX Pipes. *Journal of Biomolecular NMR* **6**, 277 – 293, (1995).
- [112] Tycko, R. Symmetry–Based Constant–Time Homonuclear Dipolar Recoupling in Solid State NMR. *J. Chem. Phys.* **126**, 064506, (2007).

- [113] Mihaliuk, E.; Gullion, T. A Frequency Selective REDOR Experiment for an  $SI_2$  Spin System. *Journal of Magnetic Resonance* **193**, 308 – 310, (2008).
- [114] Tatulian, S. A. Surface Electrostatics of Biological Membranes and Ion Binding. *In Surface Chemistry and Electrochemistry of Membranes*. Sorensen, T. S., Ed.; Marcel Dekker: New York, NY; 871 – 922, (1999).
- [115] Manzini, M. C.; Perez, K. R.; Riske, K. A.; Bozelli, J. C., Jr.; Santos, T. L.; da Silva, M. A.; Saraiva, G. K.; Politi, M. J.; Valente, A. P.; Almeida, F. C.; et al. Peptide:Lipid Ratio and Membrane Surface Charge Determine the Mechanism of Action of the Antimicrobial Peptide BP100. Conformational and Functional Studies. *Biochim. Biophys. Acta* **1838**, 1985–1999, (2014).
- [116] Petrache, H. I.; Zemb, T.; Belloni, L.; Parsegian, V. A. Salt Screening and Specific Ion Adsorption Determine Neutral Lipid Membrane Interactions. *Proc. Natl. Acad. Sci. U.S.A.* **103**, 7982 – 7987, (2006).
- [117] Qin, S.; Pande, A. H.; Nemecek, K. N.; Tatulian, S. A. The N-Terminal  $\alpha$ -Helix of Pancreatic Phospholipase A2 Determines Productive Mode Orientation of the Enzyme at the Membrane Surface. *J. Mol. Biol.* **344**, 71 – 89, (2004).
- [118] Marsh, D. Quantization of Secondary Structure in ATR Infrared Spectroscopy. *Biophys. J.* **77**, 2630 – 2637, (1999).
- [119] Marsh, D. Infrared Dichroism of Twisted Beta Sheet Barrels. The Structure of E. Coli Outer Membrane Proteins. *J. Mol. Biol.* **297**, 803 – 808, (2000).
- [120] Alwarawrah, M.; Dai, J.; Huang, J. A Molecular View of the Cholesterol Condensing Effect in DOPC Lipid Bilayers. *J. Phys. Chem. B* **114**, 7516 – 7523, (2010).

- [121] Leftin, A.; Molugu, T. R.; Job, C.; Beyer, K.; Brown, M. F. Area Per Lipid and Cholesterol Interactions in Membranes from Separated Local Field  $^{13}\text{C}$  NMR Spectroscopy. *Biophys. J.* **107**, 2274 – 2286, (2014).
- [122] Peters, C.; Bascunan, D.; Opazo, C.; Aguayo, L. G. Differential Membrane Toxicity of  $\text{A}\beta$  Fragments by Pore Forming Mechanisms. *J. Alzheimers Dis.* **51**, 689 – 699, (2016).
- [123] Shabbits, J. A.; Chiu, G. N. C.; Mayer, L. D. Development of an In Vitro Drug Release Assay that Accurately Predicts in Vivo Drug Retention for Liposome Based Delivery Systems. *J. Controlled Release* **84**, 161 – 170, (2002).
- [124] Lunelli, L.; Pasquardini, L.; Pederzoli, C.; Vanzetti, L.; Anderle, M. Covalently Anchored Lipid Structures on Amine–Enriched Polystyrene. *Langmuir* **21**, 8338 – 8343, (2005).
- [125] Sciacca, M. F.; Kotler, S. A.; Brender, J. R.; Chen, J.; Lee, D. K.; Ramamoorthy, A. Two–Step Mechanism of Membrane Disruption by  $\text{A}\beta$  through Membrane Fragmentation and Pore Formation. *Biophys. J.* **103**, 702 – 710, (2012).
- [126] Ashrafuzzaman, M.; Andersen, O. S.; McElhaney, R. N. The Antimicrobial Peptide Gramicidin S Permeabilizes Phospholipid Bilayer Membranes Without Forming Discrete Ion Channels. *Biochim. Biophys. Acta* **1778**, 2814 – 2822, (2008).
- [127] Enoki, T. A. et al. Antimicrobial Peptide  $\text{K}^{\circ}\text{-W}^6\text{-hya1}$  Induces Stable Structurally Modified Lipid Domains in Anionic Membranes. *Langmuir* **34**, 2014 – 2025, (2018).
- [128] Kotler, S. A.; Walsh, P.; Brender, J. R.; Ramamoorthy, A. Differences between Amyloid– $\beta$  Aggregation in Solution and on the Membrane: Insights into Elucidation of the Mechanistic Details of Alzheimer’s Disease. *Chem. Soc. Rev.* **43**, 6692 – 6700, (2014).

- [129] Wei, G.; Jewett, A. I.; Shea, J. E. Structural Diversity of Dimers of the Alzheimer A $\beta_{25-35}$  Peptide and Polymorphism of the Resulting Fibrils. *Phys. Chem. Chem. Phys.* **12**, 3622 – 3629, (2010).
- [130] Cheon, M.; Kang, M.; Chang, I. Polymorphism of Fibrillar Structures Depending on the Size of Assembled A $\beta_{17-42}$  Peptides. *Sci. Rep.* **6**, 38196, (2016).
- [131] Liu, J. et al. Amyloid Structure Exhibits Polymorphism on Multiple Length Scales in Human Brain Tissue. *Sci. Rep.* **6**, 33079, (2016).
- [132] Sreerama, N.; Woody, R. W. Circular Dichroism of Peptides and Proteins in Circular Dichroism: Principles and Applications (ed. Berova, N.; Nakanishi, K.; Woody, R. W.), 601 – 620 *John Wiley & Sons*, (2000).
- [133] Chen, Y.; Wallace, B. A. Secondary Solvent Effects on the Circular Dichroism Spectra of Polypeptides in Non-Aqueous Environments: Influence of Polarisation Effects on the Far Ultraviolet Spectra of Alamethicin. *Biophys. Chem.* **65**, 65 – 74, (1997).
- [134] Pande, A. H.; Qin, S.; Tatulian, S. A. Membrane Fluidity is a Key Modulator of Membrane Binding, Insertion, and Activity of 5-Lipoxygenase. *Biophys. J.* **88**, 4084 – 4094, (2005).
- [135] McMullen, T. P. W.; Lewis, R. N. A. H.; McElhaney, R. N. Cholesterol-Phospholipid Interactions, the Liquid-Ordered Phase and Lipid Rafts in Model and Biological Membranes. *Cur. Opin. Colloid Interface Sci.* **8**, 459 – 468, (2004).
- [136] Kandel, N.; Matos, J. O.; Tatulian, S. A. Structure of Amyloid  $\beta_{25-35}$  in Lipid Environment and Cholesterol Dependent Membrane Pore Formation. *Scientific Reports* **9**, 2689, (2019).
- [137] Tatulian, S. A.; Garg, P.; Nemeč, K. N.; Chen, B.; Khaled, A. R. Molecular Basis for Membrane Pore Formation by Bax Protein Carboxyl Terminus. *Biochemistry* **51**, 9406 – 9419, (2102).

- [138] Tatulian, S. A. Quantitative Characterization of Membrane Binding of Peripheral Proteins by Spin–Label EPR Spectroscopy. *J. Phys. Chem. B* **106**, 8870 – 8877, (2002).
- [139] McLachlan, A. D. Gene Duplication in the Evolution of the Yeast Hexokinase Active Site. *Eur. J. Biochem.* **100**, 181 – 187, (1979).
- [140] Chou, K. C.; Carlacci, L.; Maggiora, G. M. Conformational and Geometrical Properties of Idealized Beta Barrels in Proteins. *J. Mol. Biol.* **213**, 315 – 326, (1990).
- [141] Murzin, A. G.; Lesk, A. M.; Chothia, C. Principles Determining the Structure of Beta Sheet Barrels in Proteins I: A Theoretical Analysis. *J. Mol. Biol.* **236**, 1369 – 1381, (1994).
- [142] Murzin, A. G.; Lesk, A. M.; Chothia, C. Principles Determining the Structure of Beta Sheet Barrels in Proteins II. The Observed Structures. *J. Mol. Biol.* **236**, 1382 – 1400, (1994).
- [143] Laganowsky, A.; Liu, C.; Sawaya, M. R.; Whitelegge, J. P.; Park, J.; Zhao, M.; Pensalfini, A.; Soriaga, A. B.; Landau, M.; Teng, P. K.; Cascio, D.; Glabe, C.; Eisenberg, D. Atomic View of A Toxic Amyloid Small Oligomer. *Science* **335**, 1228 – 1231, (2012).
- [144] Darby, N. J.; Creighton, T. E. Dissecting the Disulphide–Coupled Folding Pathway of Bovine Pancreatic Trypsin Inhibitor. Forming the First Disulphide Bonds in Analogues of the Reduced Protein. *J. Mol. Biol.* **232**, 873 – 896, (1993).
- [145] Searcy, D. G.; Montenay–Garestier, T.; Helene, C. Phenylalanine to Tyrosine Singlet Energy Transfer in the Archaeobacterial Histone–like Protein HTa. *Biochemistry* **28**, 9058 – 9065, (1989).
- [146] Qiang, W.; Yau, W. M.; Lu, J. X.; Collinge, J.; Tycko, R., Structural Variation in Amyloid–Beta Fibrils from Alzheimer’s Disease Clinical Subtypes. *Nature* **541**, 217 – 221, (2017).

- [147] Paravastu, A. K.; Leapman, R. D.; Yau, W. M.; Tycko, R., Molecular Structural Basis for Polymorphism in Alzheimer's Beta–Amyloid Fibrils. *Proceedings of the National Academy of Sciences of the United States of America* **105**, 18349 – 54, (2008).
- [148] Shen, Y.; Bax, A. Protein Structural Information Derived from NMR Chemical Shift with the Neural Network Program TALOS–N. *Methods Mol. Biol.* **1260**, 17 – 32, (2015).